CRYSTAL GROWTH AND PHOTOCONDUCTIVITY

OF

TELLURIUM AND SELENIUM-TELLURIUM ALLOYS

þΣ

C I. Shih, B.Sc.; (Cheng Kung Univ.), M.Eng.

A thesis submitted to the Faculty of Graduate Studies and Research in partial fulfillment of the requirements for the degree of Doctor of Philosophy.

Department of Electrical Engineering,

McGill University,

Montreal, P.Q., Canada.

March, 1981.

ABSTRACT

A study of the growth of monocrystals of 'tellurium and selenium-tellurium alloys by the Czochralski method has been together with measurements of the photoconductivity in such materials. In tellurium, it was found that large temperature gradients occur within a growing ingot which cause increase in the concentration of lattice defects. This concentration can be reduced by subsequent annealing. An etch pit orientation effect was observed enabling the growth direction of an ingot to be determined, arising from a correspondence between preferential growth and etching planes. Photoconductivity in tellurium at 77 K was found to be decreased by abrasive polishing of the samples and increased by annealing. Transient photoconductivity was found to be characterized approximately by two time constants, one of the order of microseconds and the other tens of microseconds. largest D* detectivity measured on the samples was 1.3x10 11 cm $Hz^{1/2} W^{-1}$ at 3.5 μm . Crystals of SexTel-x Czochralski method for prepared by the Te-rich and Se-rich compositions with 0 < x < 0.10.95<x<1.0. and intermediate compositions 0.1 < x < 0.95For with it was not possible to obtain Czochralski-ingets due to a meniscus rupture problem arising from excess selenium at the growing interface. In this case crystallographically aligned samples were obtained by a slow cooling method. Measurements alloys showed a continuous wavelength

displacement of the photoconductivity maximum from 3.7 to about 0.8 µm in going from tellurium to selenium. This was accompanied by an increase of some 5 orders of magnitude in the photocesponse, in the photoconductive decay time constants and in the electrical resistivity. From the results the estimated energy gaps were found to change continuously from tellurium to selenium with a possible change of slope starting near 40 at.% Se.

_JRésumé

Une étude de la croissance de monocristaux de tellure et d'alliages sélénium-tellure par la méthode de Czochralski ainsi que leur photoconductivité respective de effectuée. Il a été déterminé que des gradients de température elevés sont présents lors du tirage du barreau, ce qui cause une augmentation de la concentration des défauts du reseau cristallin. Ces derniers peuvent être subséquamment éliminés par recuit. Un effet d'orientation des figures d'attaque a été observé permettant de déterminer la direction de relié à une correspondance entre les plans de croissance et de décapage préférentiels. Il a été observé photoconductivité dans le tellure à 77 K a été diminuée par un polissage abrasif des échantillons et qu'elle a été augmentée par le recuit. Il est démontré qué la photoconductivité transitoire peut être décrite de façon approximative au moyen de deux constantes de temps, l'une de l'ordre de microseconde et l'autre de l'ordre đe la dizaine microsecondes. La détectivité D* la plus importante mesurée sur les échantillons est de 1.3×10^{11} cm $Hz^{1/2}W^{-1}$ Des cristaux de Se Te 1-x ont été préparés par la méthode de Czochralski pour des compositions riches en tellure ou sélénium c'est dire pour 0 < x < 0.1à En ce qui a trait aux compositions intermédiaires, soit 0.1<x<0.95, il n'a pas été possible 'd'obtenir dû â barreaux-Czochralski un problèm

excès de sélénium à l'interface du ménisque issu d'un croissance. Dans . des échantillons ce cas, cristallographiquement alignés ont été obtenus effectués' refroidissement lent. Des mesutes sur ces échantillons ont démontré un déplacement continu du maximum de photoconductivité en fonction de la longueur d'onde, de 3.7 µm à environ. 0.8 µm en allant du tellure au sélénium. était accompagné d'une augmentation de quelques 5 ordres de grandeur de la photoconductivité, des constantes de temps, ainsi que de la résistivité. A partir des résultats, il a été constaté que le "gap" énergétique estimé variait de façon continue en allant du sélénium au tellure avec un changement de pente débutant aux voisinage de 40% d'atomes de Se.

ACKNOWLEDGEMENTS

() t

The author wishes to express his sincere gratitude to professor C.H. Champness for his encouragement and guidance throughout this study.

Special thanks are due to Drs. S. Fukuda and S. Jatar for helpful discussion and reading of the manuscript, to professor G. Nimtz of the University of Koln for assistance on the initial work of transport measurements, to Mr. C.K. Jen for use of a computer program, and to Mr. J. Ostiguy for translating the abstract into French.

Sincere appreciation is expressed to professors E. Adler, A. Gundjian and N. Rumin for using some of their equipment.

In addition, the help of Messrs. Borisov, Foldvari and Kwon is greatly appreciated.

Acknowledgements are also due to the Natural Sciences and Engineering Research Council of Canada for the financial support.

Finally, the author would like to thank his wife and his family for their patience and understanding during the study.

' TABLE OF CONTENTS

ABSTRACT -		, ' , ',
RESUME	•	iii
ACKNOWLEDGEMENTS		` v
TABLE OF CONTENT	S	vi
,		
	,	,1 *
CHAPTER 1 IN	TRODUCTION	٠
CHAPIER I	IRODUCTION	1
CHAPTER 2 HIS	STORICAL SURVEY	, 11
2.1 In	troduction	, 11
2.2 Cze	ochralski Growth of Tellurium Crystals	11
2.3 Gro 2.4 Pho	owth of SexTel-x Crystals otoconductivity in Te	15 17
2.5 Pho	otoconductivity in Se Te 1-x3 Alloys	18
		1
CHAPTER 3 OR	IENTATION OF ETCH PITS ON TELLURIUM	22
	troduction	22
	view of Experiments on Chemical Etch Pits	23
	ur-sided etch pits ree-sided etch pits	23 25
	esent Work	26
	ir-sided pits on (1010) surfaces	26
	cee-sided pits on (0001) planes	28
3.4 Dis	scussion	30
	FECT OF TEMPERATURE GRADIENTS DURING	<u>.</u>
GRO	OWTH OF TELLURIUM	42
4.1 Int	roduction	42
4.2 Ten	perature Distribution During Growth	43
4.2.1 Ten	perature measurements in a growing	4.3
	.lurium crystal .culation of temperature distribution	43 46
4.2.2 Car	stal Growth and Transport Measurements	52
	stal and sample preparation	52

		*5 * * * * * * * * * * * * * * * * * *	
المعر \ \ ا	4.3.2	Transport measurements	53
		Annealing experiments	54
. \	4.4	Discussion and Conclusions	55
\			70
`	\ , ,	· · · · · · · · · · · · · · · · · · ·	
CHAPTER	5	CRYSTALLINE GROWTH OF Se Te ALLOYS	· 69
		x 1-x	
•	5.1	Introduction	69
1	5. 2	Limiting Growth Rate Considerations	70
	5.3	Growth Procedures	72
- n	5.4	Te-rich Alloys	73
_	5.5	Se-rich Alloys	74
,	5.6	Crystallization by Slow Cooling Method	76
	5.7	Laue Patterns and Compositional Analysis	76
	5.7.1	Laue patterns	76
,		Compositional analysis	78
	5.8	Discussion and Conclusions	80
	•	*	
			- /
CHAPTER	6	MEASUREMENT APPARATUS AND METHODS	101
		· · · · · · · · · · · · · · · · · · ·	,
	6.1	Introduction	101
	6.2	Sample preparation	101
		Czochralski-grown Te and Se _x Te _{1-x} alloys	101
\	6.2.2	Czochralski-grown Se-rich and Slow-cooled	
1		alloys	102
	6.3	Apparatus	103
م.	6.3.1	Cryostat	103
		Optical system	104
		Measurement Method	108
.\		Steady state photoconductivity	108
		Transient decay	110
1		Frequency dependence and noise	
\		measurements	110
0			
•		**	
CHAPTER	7	PHOTOCONDUCTIVITY RESULTS IN UNDOPED TELLURIUM	118
		,	
	7.1	Introduction	118
		Special Sample Treatment	118
\		Low Frequency (13 Hz) Photoconductivity Results	119
		Variation with temperature	119
		Effect of sample treatment and	,
1		thickness	120
\		Transient and Frequency Response Results	121
	7.4.1	Photoconductive decay	121
,	7.4.2	Frequency response · · \	122
	7.5	Calculated Response at Now Frequency	124
,	7.6	Excess Noise and Detectivity Results	125
, T	7.7	Discussion and Conclusions	126
	*	· · · · · · · · · · · · · · · · · · ·	

v	•	*	
, CHAPTER	- 8	PHOTOCONDUCTIVITY RESULTS IN SexTel-x ALLOYS	141
	8.1 8.2 8.3	Introduction Steady State Photoconductive Spectral Response Transient Photoconductivity	141 141 143
**	8.4	Electrical Resistivity and Hall Mobility Conclusions and Speculations	144 144
* /			
CHAPTER	9	CALCULATION OF ABSORPTION COEFFICIENTS AND ENERGY GAPS	150
		AND ENERGI GAFS	158
	9.1	Introduction	158
	9.2		159
	9.2.1	Photoconductivity	159
	9.2.2	Absorption edge	161
		Calculated Absorption Coefficients	162
		Undoped tellurium	162
	9.3.2	Se _x Te _{1-x} alloys Discussion	165
t	9.4	Discussion	167
CHAPTER '	10	DISCUSSION AND CONCLUSIONS	181
	10.1	Introduction	181
	10.2	Growth of Pure Tellurium	181
	10.3	Growth of Se _X Te _{1-X} Alloy's	182
	10.4	Photoconductivity in Tellurium	183
		Photoconductivity in Se _x Te _{1-x} Alloys	186
-	10.6	Future Work	187
REFERENC	, PEC		. , 100

Marie Commence Commence of the second

CHAPTER 1 INTRODUCTION

Tellurium is a semiconductor with a number specially interesting properties, some of which arise from its trigonal crystal structure. The lattice consists (Fig. 1.1) of parallel helical chains of atoms with the first and fourth atoms in the same angular position but displaced along the three-fold axis by the distance c. The point group is D2, which is the same as that of quartz, and like this substance, it is optically active except that this is observed only beyond the absorption edge near 4 µm wavelength. Tellurium is birefringent with the very large values of refractive index of $n_1=4.8$ and $n_{\parallel}=6.0$. It dichroic, notably at the absorption edge and at 11. um, where there is an absorption band for Ellc but not for Elc. The electrical conductivity is anisotropic with a value along the c-axis twice that perpendicular to it. It shows a double reversal of the sign of the Hall coefficient and has always been found to be extrinsically p-type at liquid nitrogen temperature. The substance is strongly piezoelectric and shows appreciable nonlinear optical effects with the passage of infrared laser radiation; in particular 5.3 µm wavelength second harmonic radiation can be generated from a 10.6 laser beam. Some of the basic parameters of tellurium are listed in Table 1.1. More details of physical properties are given in ref. [1.1] .

While the bonding along the atomic chains is strong, that between them is weak, so that cleavage readily takes place along prism planes. This also means that lattice damage easily occurs and that the material is very sensitive to handling. For this reason, measured physical properties are affected by the preparation procedure of the samples and hence there is often doubt about the magnitude of some published data on tellurium. There is thus a need, not only for the measurement of the parameters of new physical phenomena, but also for a repetition of previously reported measurements using samples prepared under known conditions.

With an energy gap of 0.33 eV, tellurium shows photoconductivity when illuminated with lightwavelength less than about 4 µm. The effect is more prominent at liquid nitrogen temperature than at room temperature. Some studies have already been made to understand and characterize a the effect and other work has been done to evaluate tellurium, in a preliminary way, as an infrared detector material for use near 3.5 µm wavelength. However, in all previous work the material used would have contained imperfections due to the methods used to prepare the samples and therefore it was considered appropriate to embark on a new program to grow crystals of tellurium, to understand the conditions needed for minimizing defects and to obtain a new characterization of photoconductivity in the material. This forms part of the

work to be described in this thesis.

In this program, the work on the growth of tellurium crystals consisted of a study of the effect of temperature gradients in the ingots during Czochralski pulling on extrinsic transport properties. These were also measured after annealing to remove the defects. In the course of these investigations and in some previous studies by the author [1.2], etch pit studies were made and a curious orientation effect was found. In the present thesis, this has been further studied.

The measurements of photoconductivity on tellurium were done at liquid nitrogen temperature over the wavelength region between about 1 to 4.5 µm, where the effect is most sensitive, and in these studies the influence of factors such as sample thickness, surface treatment and temperature was investigated. Transient measurements to determine decay times were also carried out. In addition, an examination was made of factors relevant to the possible use of tellurium as an infrared detector material, namely noise, low frequency response and photoconductive spectral detectivity.

The preparation and preliminary study of crystalline selenium-tellurium alloys forms the other part of this thesis. Selenium is a semiconductor, which, in its trigonal form, has

a reported energy gap of 1.85 eV [1.3]. Like tellurium it has many interesting properties [1.3] but in addition it also has practical applications. It has been established that selenium and tellurium form a complete solution in all proportions in both the liquid and solid phases. Therefore, possibility of obtaining crystalline the semiconductors with tailored energy gaps over the wide range from about 0.3 to some 2 eV. Such alloys, if they could be made in controlled single crystal form, might be useful for applications requiring special energy gaps, such as for infrared detectors and solar cells. The alloys could also be useful scientifically in elucidating, for instance, change-over from the direct band gap of tellurium to indirect one of selenium. For these reasons a program was initiated with the objectives to grow SexTel-x crystals by the Czochralski mehtod and thence to measure the band gap changes from photoconductivity measurements. As will be seen in chapter 5 of this thesis, growth by the Czochralski method proved to be exceedingly difficult for the alloys compared to pure tellurium. This was because of an inherent problem requiring a growth rate and a temperature stability quite beyond the possibilities of the growth apparatus, even when difficulties, its limits. Despite the Czochralski-grown crystalline alloys were obtained at Te-rich Se-rich compositions. For intermediate compositions, however, another method was used to obtain samples which,

while not completely monocrystalline, were sufficiently aligned crystallographically for the optical and electrical measurements. The photoconductivity measurements, which were the first made on such alloys below room temperature, show very nicely the shift of the characteristics with change of composition from tellurium to selenium. A calculation was also made of the absorption edge of each alloy from the photoconductivity to observe the change of energy gap with composition.

 C_t

While the SexTe_{1-x} investigation forms a smaller portion of this thesis and represents only a preliminary stage in the study of such materials, this work is considered by the author to be the most significant contribution presented here. In the course of the work, for instance, selenium single crystals were prepared for the first time in this laboratory, a result which could open up a new area of study.

Since the Czochralski method was the main technique used in the crystal growth work of this thesis and since a treatment of it will not be given in other chapters, a brief description of the apparatus is now given. Greater details are available in reference [1.2]. The tellurium in a quartz beaker (Fig. 1.2) is first melted under an argon or argon-hydrogen atmosphere by radio frequency induction heating, where

currents are induced directly within the material itself. This is done from a work coil surrounding the main growth chamber, which is made of Pyrex or quartz. A background temperature is provided by resistance heating from a flat wire wound around the growth chamber. A monocrystalline seed, held in a chuck at the end of a vertical rotating pull rod, is slowly lowered into the melt and after dipping, is slowly withdrawn vertically. If suitable temperature conditions prevail, the tellurium freezes uniformly on to the seed in such a way that a boule or ingot with a diameter larger than that of the seed can be "pulled" from the melt.

 \mathbf{C}

Finally, it might be helpful as a quide to the reader to sketch out briefly the structure of the thesis chapter by chapter. While the order of the chapters is important, it is quite possible to read some of them before the preceding ones. The author's work on tellurium for the M.Eng. degree is briefly reviewed in chapters 2 and 3. Beginning with chapter 2, a brief historical survey is given of work done firstly on the Czochralski growth of tellurium, secondly on melt growth Se Te 1-x of alloys and thirdly and fourthly' photoconductivity on tellurium and the alloys. Next in chapter 3 the interesting etch pit orientation effect is reviewed and further work is presented. In chapter 4 the study is reported on the influence of temperature gradients in tellurium ingots during growth on extrinsic transport properties. Chapter 5

describes the efforts to grow crystals of the Se_xTe_{1-x} alloys. The apparatus and methods used for photoconductivity measurements are described in chapter 6, while the results of such measurements are presented in chapter 7 for pure tellurium and in chapter 8 for the alloys. In chapter 9, absorption coefficients are calculated and hence energy gap values are determined. Finally, the results of the thesis are summarized in chapter 10.

Table 1.1

Some Physical Constants of Tellurium

Atomic number 52

Atomic weight 127.6

Lattice parameters a = 4.4572 Å

C = 5.9290 Å

Normal melting point 452°C

Normal boiling point 990°C

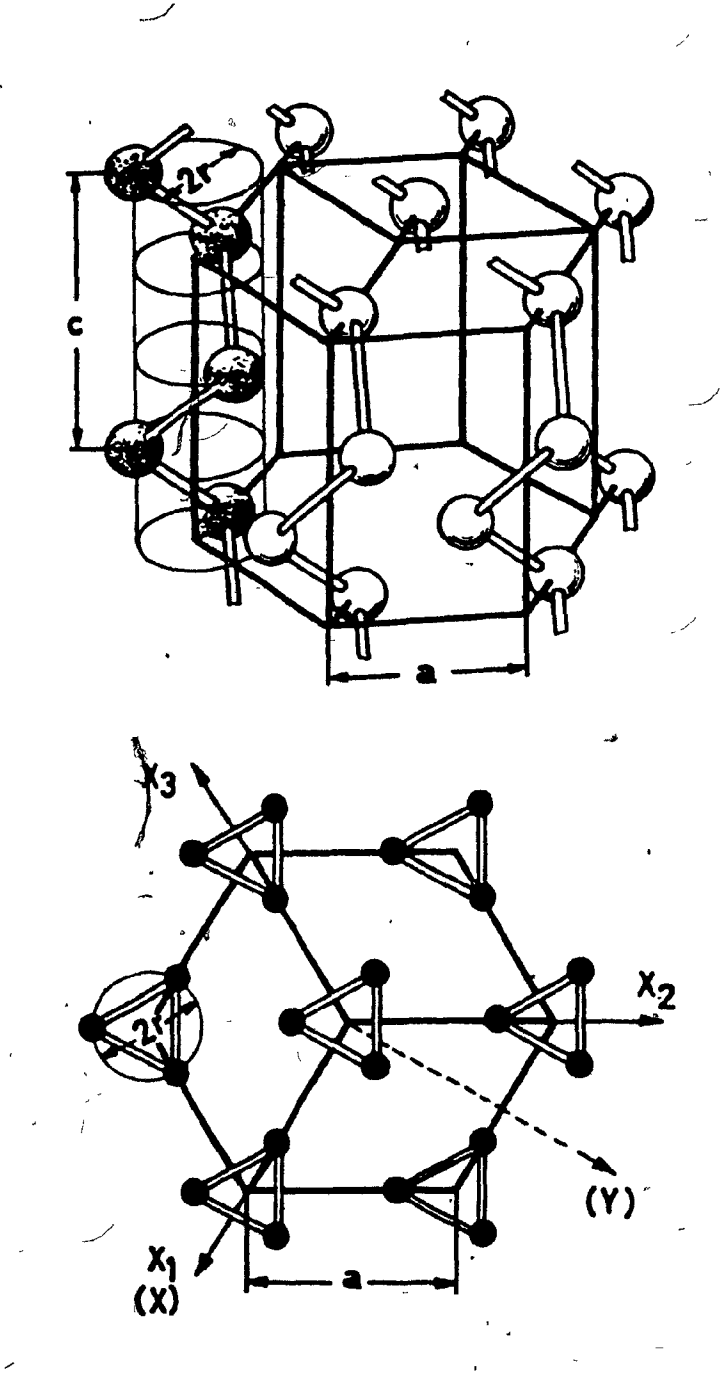


Fig. 1.1 Arrangement of the atoms in a tellurium crystal [2.7].

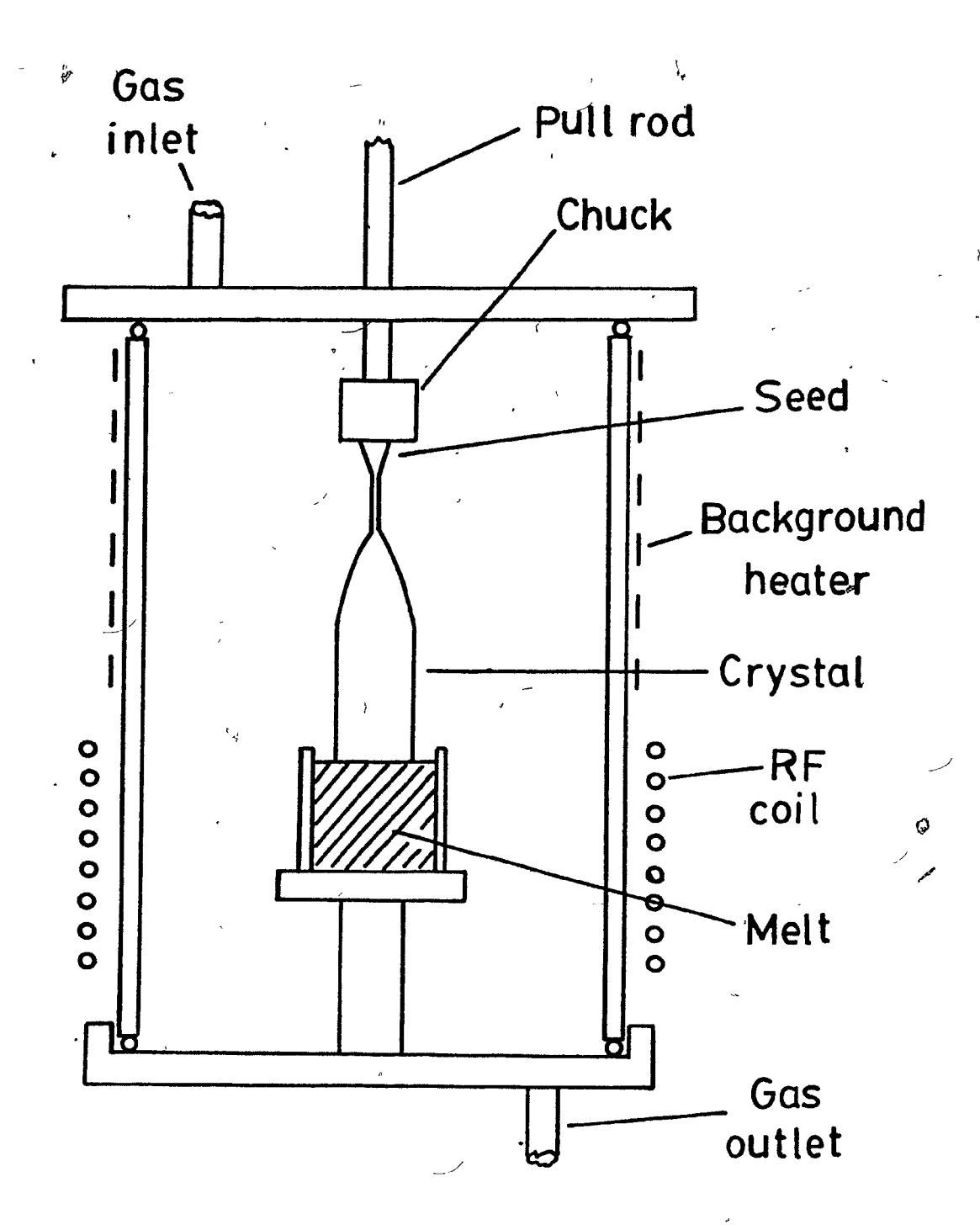


Fig. 1.2 Diagram showing the arrangement of the Czochralski growth chamber.

CHAPTER 2 HISTORICAL SURVEY

2.1 Introduction

In this chapter a review is given of the history of work done in the area of the thesis. It consists firstly of a presentation of the past work on the growth of tellurium crystals by the Czochralski method, followed by a review of the growth from the melt of $\operatorname{Se}_{x}^{\operatorname{Te}}_{1-x}$ alloys. Then, previous work on photoconductivity in Te and $\operatorname{Se}_{x}^{\operatorname{Te}}_{1-x}$ alloys is briefly reviewed.

In the review of Czochralski work on tellurium, more words have been given on the author's previous work than on that of others. This is not because of its greater importance, but because of the relevance to this thesis. In addition, it should be mentioned that the survey on work done on pure selenium does not pretend to be exhaustive, since the emphasis in the present work has been more on tellurium.

2.2 Czochralski Growth of Tellurium Crystals

Crystal growth of tellugium using the Czochralski method was first reported in 1954 by Weidel [2.1], who grew single crystals having a width of about 1 cm and a length of several cm, where the pulling direction was parallel to the

 \bigcirc

c-axis. Three years later in 1957, Davies [2.2] grew crystals from tellurium melts at pulling rates between 2 and 5 cm/hr. He reported that a necked-in seed seemed to yield the highest percentage of single crystals. In 1962, Link [2.3] reported a growth study on Czochralski tellurium crystals and, for the first time, pointed out the alternate large and small faces of ingots pulled in the c-direction. In 1963, Keezer described a very detailed crystal growth study. He found that it was important to have good alignment of the seed because a misorientation by more than 1° resulted in unstable crystal growth. He also pointed out that temperature control to better than ±0.1°C was necessary for uniform crystal growth. Tellurium crystals were also reported to have been grown in directions both parallel and perpendicular to the c-axis in the sixties by Shalyt et al [2.5] in the USSR and by Ishiguro et al [2.6] in Japan.

In 1969, Grosse [2.7] found that Czochralski growth results were better with the removal of the scum, which often occurred on the melt surface. About the same time, Kolb and Laudise [2.8] grew crystals using the Czochralski method with resistance heating and found better results at the slower growth rates. Cerclet [2.9], also in 1969, grew crystals at pull rates between 1 and 2 cm/hr. He found that the quality of the crystals was improved by annealing at 360°C. In 1973, Dufresne and Champness [2.10] reported crystal growth in

directions both parallel and perpendicular to the c-axis. They also found that the yield of crystal growth was improved with a thin neck in the initial stage of the crystal pulling. Cerclet [2.11], in 1973, grew ingots from melts containing a certain amount of impurities and confirmed an increase in monocrystallinity with decrease of impurity content and of pull rate.

In 1978, a detailed study of tellurium crystal growth by the Czochralski method was reported by Shih and Champness [2.12] arising out of the experimental work for the author's M.Eng thesis [1.2]. The study was started by adopting most of the previously reported important growth conditions, namely a narrow neck, a good alignment of the seed, a clean surface (removal of the scum), a background heating unit, a high purity raw material and a good temperature control scheme. With the above-mentioned conditions, it was found that the successful rate in producing tellurium single crystals was (more than 10 mm) only about 20%, even with a long (less than 0.5 mm) neck (see Fig. 2.1(a)). Further study was then performed by considering the importance of temperature changes in the growth chamber, especially that in the seed. The temperature study revealed that polycrystallinity of the crystal resulted if the seed was subjected to a too rapid during the temperature change seed dipping process. procedure involving a slow seed lowering rate and a relatively

high background temperature was thus established for subsequent studies. The improved procedure proved to be very successful in producing single crystals and, in the program, more than 30 ingots were grown without further necking. All of these were found to be completely single crystals, corresponding to a 100% yield. Fig. 2.1(b) shows a single crystal with a thick neck grown in this series.

 $I_{\mathcal{B}}$

Using the improved starting procedure, effects of other growth conditions on the crystal were studied by the present author [1.2]. It was found that polycrystallinity was produced with a high pulling rate (more than 3 cm/hr) and a low background temperature (less than 350°C). Good quality crystals were readily grown at a high background temperature (about 400°C). For the growth direction parallel to the c-axis, it was also observed that the ratio of the width of the three larger faces to that of the three smaller ones was increased with increase in the pulling speed. For the growth direction perpendicular to the c-axis, a similar relation was found between the ratio of the larger axis to the smaller one and the crystal pulling speed.

In a study of etch pits on tellurium [1.2], it was first confirmed that a correlation existed between mechanical damage (and hence dislocations) and etch pit density. However, some interesting features regarding the orientation

of the etch pits on the basal and the prism planes were observed. This effect will be described in more detail in chapter 3.

()

2.3 Growth of Se Te 1-x Crystals

Most of the previous work to prepare single crystal Se Te1-x alloys has been done using the Bridgman method or methods similar to it. One of the first reports was that of Loferski [2.13] in 1954, who prepared crystals up to about 16 at.% Se by this method. At the Se-rich end of the range, Keezer, Griffiths and Vernon [2.14] grew crystals by the Bridgman method from 100 to 97 at. 8 Se using 18 Tl or K in the melt to lower viscosity by shortening the length of Se chains. Sutter [2.15], in 1969 grew Bridgman crystals of composition 10 to 90 at. Se, while Shiosaki and Kawabata [2.16] (1971) used seeding in their Bridgman method to obtain monocrystals containing 70 to 100 at. Se, with growth rates of 0.2 to 1.5 mm/hr. A Bridgman and a zone-leveling method was used by Beyer, Mell and Stuke [2.17] in 1971 to obtain crystalline samples over the whole range with growth rates from 0.1 to 5 mm/hr; for the Se-rich mixtures, they added 1% T1 or K to the melt to reduce viscosity. Crystals from 10 to 90 at. Se were grown in 1975 by Bahl and Chen [2.18] with the Bridgman method at a lowering rate of 0.4 mm/hr. The Bridgman method was also used in 1978 by Bhatt and Trivedi [2.19] to obtain crystals of

10 at. 8 Se from a melt containing 1% Tl, with a lowering rate of 4.5 mm/hr.

While the Czochralski method, as mentioned above, has been very successfully used to obtain monocrystals of tellurium, it appears that only Keezer and co-workers have reported serious attempts to grow alloy crystals by this method. Using a pull rate of 1 mm/hr, Keezer, Griffiths and Vernon [2.14] were able to obtain monocrystals with 0 to 5 at.% Se in 1968. They found polycrystalline growth for Se concentrations higher than 5 at.%, which was ascribed to constitutional supercooling. In 1967, Keezer, Wood and Moody [2.20] grew monocrystals of 100 at.% Se by the Czochralski method using selenium melts doped with chlorine and bromine at pull rates of about 0.2 mm/hr and doped with Tl at rates up to 2.5 mm/hr.

Regarding the crystal structure of Se_xTe_{1-x} alloys, Grison [2.21] considered the two possibilities shown in Fig. 2.2. In one of these, the Se and Te atoms are in different but parallel helices (Fig. 2.2(a)), while in the other, each helix contains a mixture of Se and Te atoms (Fig. 2.2(b)). The experimental X-ray evidence lead Grison to favour the latter structure.

2.4 Photoconductivity in Te

Photoconductivity has been known in tellurium for more than half a century. In 1925, Bartlett [2.22] first showed that the effect in thin films was larger at liquid oxygen temperature than at room temperature. Some years later Moss found the photoconductivity maximum to lie at wavelength near 1.3 µm for cooled thin tellurium films evaporated on glass substrates. However, the first results on bulk crystal samples were reported by Loferski [2.13] in 1954. These samples were obtained by cleaving a Bridgman-grown ingot containing randomly oriented crystals, followed by abrasive grinding and polishing with final chemical etching. Edwards, Butter and McGlauchlin [2.24] published results in 1961 on samples prepared by vapour phase growth and by cleaving a Czochralski-grown crystal. On one of their vapour-grown samples they reported a detectivity at 77 K and wavelength of 3.4 µm which was essentially background limited. Vis [2.25] also studied photoconductivity on bulk samples, which were prepared by air-brasive cutting from slices cleaved tellurium Czochralski-grown crystals, followed chemical etching. In addition he studied the dependence of noise on frequency and temperature [2.26]. In 1966, Grosse and Winzer [2.27] made a detailed study of photoconductivity in

 $\mathcal{L}()$

bulk samples cut abrasively from Czochralski crystals followed by etching. They observed the decrease in response with decrease of wavelength below 3.5 µm and found this to be more rapid for the orientation with the electric vector E of the radiation perpendicular to the c-axis of the sample than for that with E parallel to it. Grosse and Winzer also showed the importance of the surface recombination velocity (s) in tellurium, which they determined from the shape of the spectral dependence of photoconductivity.

In all the previous work mentioned, abrasive action was involved in the preparation of the samples and while chemical etching was often carried out, lattice damage would not have been entirely removed. The first complete avoidance of abrasive preparation was in work in this laboratory [7.1]. Using such samples, this study showed how sample thickness changed not only the magnitude of the photoconductivity in tellurium but also caused a wavelength shift in its peak value.

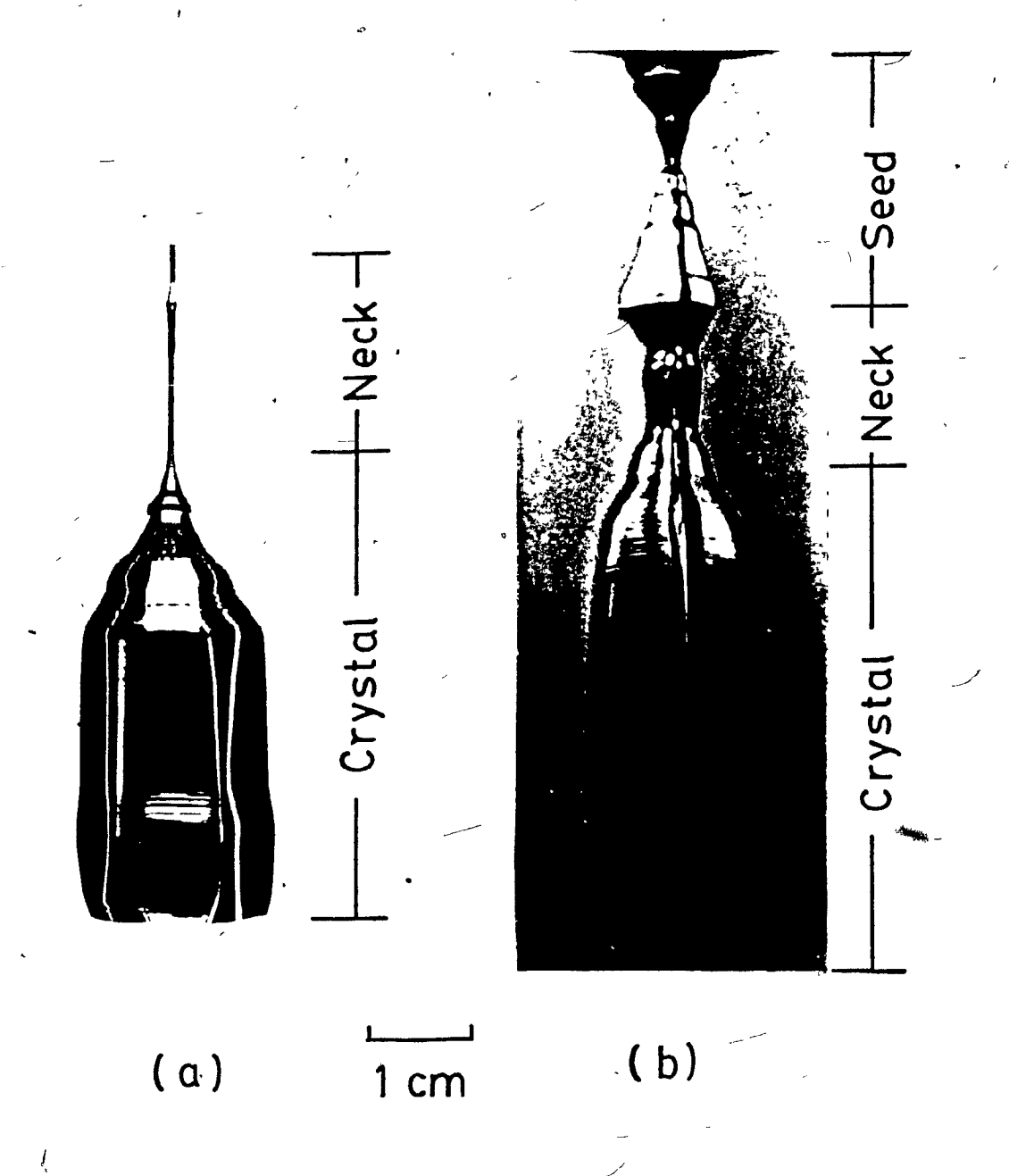
2.5 Photoconductivity in SexTe 1-x Alloys

Photoconductivity in selenium was discovered in 1873 by Smith [2.29], who observed a decrease in the resistance of a selenium bar after illumination with light. Since then there have been many photoconductive measurements made on

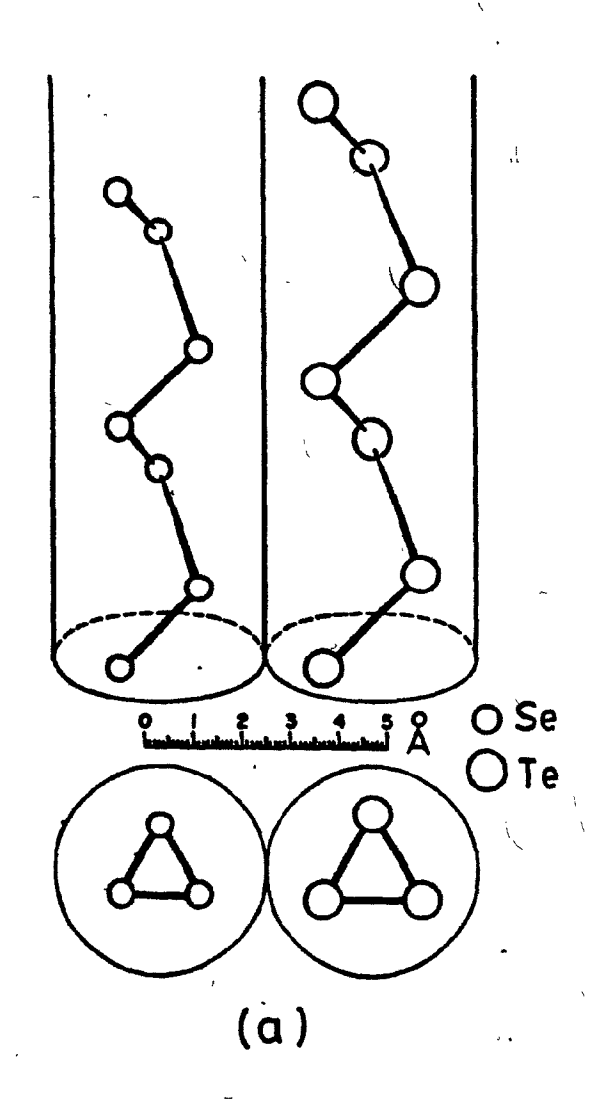
(<u>)</u>

polycrystalline selenium but data on monocrystalline trigonal material has been limited. Prosser [2.30] in 1960 found two photoconductive maxima, one near 0.6 and the other near 0.7 latter peak shifted to shorter wavelengths with A similar from 295 to 95 K. decrease of temperature temperature shift of the 0.7 µm peak was reported by Hemila peak was also measured at 93 K by and Tuomi [2.31]. This Stuke [2.32] in 1964. He observed another peak near whose magnitude was found to be very sensitive to plastic deformation of the sample. A more complete discussion of photoconductivity and allied phenomena in trigonal selenium can be found in the article "Optical and Electrical Properties of Selenium" by J. Stuke [1.3].

Compared to tellurium and selenium, very little work has been reported on photoconductivity of Se_XTe_{1-X} alloys, whether polycrystalline or monocrystalline. In fact the only paper on monocrystalline alloys appears to be that of Kessler and Sutter [2.33] in 1967. These workers measured photoconductivity at room temperature on 10 samples ranging in composition from 10 to 90% Se; they found the long wavelength maximum to shift from about 3.4 to 0.8 µm over this range.



Tellurium single crystals (a) grown under fast approach and low background temperature with a long and thin neck, and (b) grown under improved conditions with a thick neck. Fig. 2.1



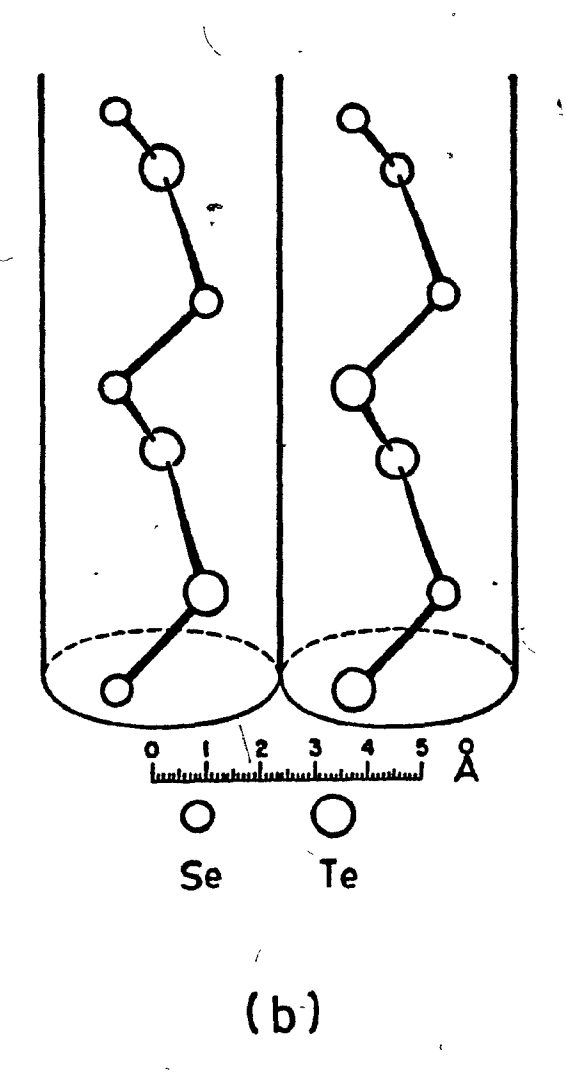


Fig. 2.2 (a) One chain of tellurium and one of selenium, and (b) chains with random sequence (taken from [2.21]).

CHAPTER 3 ORIENTATION OF ETCH PITS ON TELLURIUM

3.1 Introduction

The study of etch pits in semiconductors is interesting principally in order to determine the extent of dislocations present. The same is true in tellurium but it has been found that, in addition, the etch pits on certain planes show an interesting orientation effect. It is this aspect which is of special interest in the present chapter.

Etching in tellurium can be performed by thermal and chemical means [3.1,3.2]. Chemical polish etching is a fast etching procedure to produce a smooth flat surface, usually carried out with chromic-nitric or chromic-hydrochloric solutions. These etches were used in the preparation of surfaces of samples for the measurements in chapters 7 and 8. However, details concerning their action have been discussed elsewhere [3.1,3.2] and they will not be further discussed here. In this chapter, only chemical etch pits produced by slow etching will be treated. More specifically, the interest is in the orientation of the four-sided etch pits on the prism planes and the three-sided pits on the basal planes. These,

it will be shown, define a unique sense along the c-axis.

3.2 Review of Experiments on Chemical Etch Pits

3.2.1 Four-sided etch pits

If the prism (1010) planes of a tellurium crystal are treated with sulfuric acid at 150°C for about 5 minutes, four-sided etch pits are developed, an example of which is shown in Fig. 3.1. These particular etch pits were first reported by Blakemore, Schultz and Nomura [3.3] on cleaved tellurium surfaces. They pointed out that the pits were not symmetrical about the c-axis but that the longest edge was parallel to this direction. They suggested the four internal planes to be (1100), (1013), (0111) and (0111).

From the work of Blakemore and Nomura [3.4] and of Herrmann [3.5] it was found that there were two types of 4-sided pits, which were the mirror images of each other. However, only one type was found on one crystal. It was shown by Blakemore and Nomura [3.4] that one type occurred on a crystal with a right-handed helix of atoms and the other on a left-handed crystal. The handedness of the crystals involved in these studies was found by Nomura [3.6] by determination of the sense of rotation of the plane of polarization of light passing along the c-axis of the samples. Herrmann [3.5]

pointed out that the acute angle of the pits pointed in opposite directions on the adjacent prism faces. He also reported that the etching produced hills on one grown surface and pits on the opposite parallel surface. This latter fact has not been confirmed by subsequent work and in any case appears to be inconsistent with the symmetry of the crystal. In the studies of Koma, Takimoto and Tanaka [3.7] only pits and no hillocks were found on opposite planes and this has also been the experience of the writer. The Japanese workers clearly identified mirror image pits from right- and left-handed crystals and also attempted to explain the etch pit shapes from an atomic model involving the following assignment of internal planes (1650), (1451), (0551) and (1671). These clearly differ from the earlier assignment made by Blakemore, Schultz and Nomura [3.3].

In connection with the three equivalent (1010) and three (1010) prism planes, on which the four-sided etch pits are formed, these are the large lateral facets in Czochralski crystals pulled in the c-direction. Link [2.3] found that three of them, symmetrically arranged, were larger than the other three. The writer [2.12] showed also that the ratio of the width of the large face to that of the small face can be increased by increasing the pull rate.

Further work, in the laboratory of the writer [3.8] on

the four-sided etch pits, confirmed the following facts, (1) that the acute angle of the pits points in opposite directions on alternate prism faces, (2) that the largest edge of a pit the c-axis and (3) that the is parallel to right-handed crystals are the mirror images of those on left-handed crystals. In addition, however, a new feature was observed, namely that the acute angle of the pits always pointed towards the melt end of the ingot on the three large faces and always pointed towards the seed end on the three smaller faces. Thus, despite the fact that the crystal structure of tellurium does not distinguish a sense along the c-axis, it is possible to determine the growth direction of a crystal from the etch-pit orientation.

3.2.2 Three-sided etch pits

The basal plane, not being a cleavage surface, has to be cut and polished. The best way to do this is to use one of the fast acting polish etches. A slow acting etch will then bring out pits which are often hexagonal or triangular in shape.

Etching experiments on the (0001) plane were studied by Di Persio, Doukhan and Saada [3.9], who first reported hexagonal etch pits using a mixture of H₃PO₄, H₂SO₄ and CrO₃ at about 150 °C. The edges of the etch pits were observed to be

parallel to the planes of the crystal. A similar etch, used by Ahmed and Weintroub [3.1] was found to bring out triangular or hexagonal etch pits on (0001) surfaces. Hexagonal pits were also found by Doukhan and Farvacque [3:10] using a mixture of H₃PO₄ and CrO₃ (250 gm: 5 gm) at 150°C. The effect of the phosphoric-chromic etchant was confirmed by El Azab, McLaughlin and Champness [3.2], who also reported triangular as well as hexagonal etch pits. These results were further confirmed by Kalinski and Lehmann [3.11] who found that the hexagonal etch pits eventually became triangular after prolonged etching at 160°C for about 20 minutes.

3.3 Present Work

The further work done in this laboratory to characterize the etch pit orientation effect is now described.

3.3.1 Four-sided pits on (1010) surfaces

It was found that if a piece of tellurium, cut from a c-grown crystal, was used as the seed to grow another crystal and if the seed sense was the same as that of the original crystal, then the large faces of the new crystal grow from the large faces of the seed. This is illustrated schematically in Fig. 3.2(b), where the etch pits point downwards on the large faces of both ingot and seed. The result was also previously

demonstrated by necking and expanding the ingot diameter during growth (by adjusting the temperature), which yields a crystal, where the large faces on either side of the necked region correspond to each other.

Three growth runs were next made where the "seeds" were "inverted", that is, the sense was reversed with respect to crystals from which they were originally cut. Thus, in the seeds, the four-sided etch pits, had they been present, would point upwards on the three large faces and downwards on the small faces. The runs were also carried out at a faster pull rate than normal to obtain an eccentricity (ratio of the width of larger face to small face) of about 2 in order to ensure unambiguous results. The resulting crystals all had small faces developed from the large faces of the seed and large faces from the small faces, as indicated diagrammatically in Fig. 3.2(a). An actual photograph of an ingot and seed after such growth is shown in Fig. 3.3. Thus, irrespective of the direction of the etch pits on the seed, the etch pits on the grown crystal always point downwards on the large faces.

It was also interesting to know whether the formation of a large or small face was determined by the three metal screws in the seed chuck due to a fast heat flow through the screws. Therefore, in the above-mentioned experiments, two runs were made with the screws in contact with the three large

faces of the seed and one with the screws in contact with the three smaller ones. All the three crystals were found to have large faces developed from small faces of the seed. Therefore, the position of the screws had no effect on the development of the large and small faces and no influence on the lateral growth rate of the crystal.

In order to investigate the influence of seed rotation rate on the crystal shape, two more crystals (CZ-77-20 and CZ-77-21) were grown at pull rates of 10 and 15 mm/hr respectively. During the growth, the rotation rates were changed from 3 to 35 rpm in 6 steps. Fig. 3.4 shows a plot of the ratio of long to short side of the two crystals against the seed rotational rate. It is seen that there is essentially no change in the ratio as the rotational rate is increased from 3 to 35 rpm. It was also verified, by reversal of the sense of rotation, that this had no effect on the configuration of faces and orientation of etch pits.

3.3.2 Three-sided pits on (0001) planes

O

The uncertainty about the designation of the internal planes of the four-sided etch pits makes the understanding of their shape somewhat difficult. It was thought, however, that it might be simpler to interpret the triangular or hexagonal pits on the (0001) basal planes.

Therefore, a wafer was chemically cut perpendicular to c-axis of ingot CZ-80-4, which had a clearly defined difference between large and small prism faces. The (0001) surfaces of the slice were chemically polished with a HNO, CrO₃, H₂O solution (10:5:20 by weight). The wafer was then immersed in phosphoric chromic solution (200:5 by weight) at 140°C for 20 seconds. This brought out hexagonal etch pits on the (0001) surface, as shown in Fig. 3.5. It is noted, in indicated orientation the of cross-section, that the three larger sides of the pits (on the surface facing the melt end) were adjacent (and parallel) to the three shorter sides of the crystal prism faces. On the surface facing the seed end, however, (not shown) the opposite was true, namely that the longer sides of the hexagonal pits were adjacent to the larger sides of the crystal. Thus (as in the case of the four-sided pits) the configuration enables the growth direction to be determined; the surface facing the melt end is clearly distinguishable from that facing the seed end.

Longer etching on the basal planes produced a reversal in the pit configuration but the uniqueness of the growth sense was maintained. The small hexagonal pits were removed with the chromic nitric polish-etch (1 minute at 25 °C). Then the sample was etched for 30 minutes at 140 °C in the phosphoric-chromic solution. The longer etch produced larger triangular etch pits as shown in Fig. 3.6. This time, however,

(F)

the sides of the triangles (or the long sides of very eccentric hexagons) were adjacent (and parallel) to the large prism planes of the crystal on the surface facing the melt and adjacent to the smaller planes on the surface facing the seed. Thus, while the correspondence between pit edge and crystal prism face was opposite to that for the small hexagonal pits, the surface facing the melt end was again distinguishable from the surface facing the seed end.

In the case of these larger triangular pits, it was possible to estimate the angle of the three internal planes. This was done by measuring microscopically their depth by focusing first on the lowest point of the pit and then on the immediate surrounding surface. From the depths of 4 pits on each of the two surfaces, the average angle between the c-plane and the pyramidal planes was found to be 55°.

3.4 Discussion

It is clear that the growth direction in a grown tellurium crystal pulled in the c-direction by the Czochralski method can be determined from either the configuration of the four-sided etch pits on the prism planes or the three- or six-sided pits on the basal planes. It has been assumed that while growth was vertical in the Czochralski method, gravity played no role in providing a special sense to the pits.

the earlier stages of the experimental work During involving only the four-sided etch pits, some discussions took place with professor P. Grosse of the Technischen Hochschule in Aachen. He suggested that the orientation effect was due to preferential growth on the three pyramidal ((1011), (1101) and (0111)) planes and slower growth on the other three pyramidal planes (($\overline{1101}$), (01 $\overline{11}$) and ($\overline{1011}$)). The latter planes have a higher surface density of atoms than the former surfaces. This explanation would explain many of the observed facts. The three slower growing planes would generate the three larger prism face's of a growing crystal ((1100), (0110) and (1010)) and the three faster growing planes would lead to the three smaller prism faces ((1010), (1100) and (0110)). growth from the other end of the ingot, the same configuration would result again in the three ((1011), (1101) and (0111)) planes, producing large prism faces but now they would develop from where small faces existed before. This would be true whether the crystal was grown from the liquid or the vapor or whether growth takes place vertically or horizontally. In a vapor-grown crystal, such as that shown schematically in Fig. 3.7, the predominant growth end is that where the large pyramidal plane is adjacent to a large prism plane. Growth at the same rate at both ends would of course yield prism planes of equal width.

A photograph of an actual vapor-grown tellurium crystal

is shown in Fig. 3.8, which was obtained by a sublimation in a quartz tube over a period of about 80 hours, where the prism and pyramidal planes are clearly seen. In this case, it would appear that predominant growth was from the right-hand end. Fig. 3.9 shows a view of this same crystal, rotated so that one of the large pyramidal planes is seen side-on at both ends. Measurement of the angle between this plane and the basal c-plane gives 55° . If the c/a ratio is taken as 1.33 [3.12] then the angle should be $\tan^{-1}(\frac{2 \text{ c}}{\sqrt{3} \text{ a}})$ or 56.9° . This is also close to the value of 55° for the measured angle of the internal planes in the long-etched triangular pits.

Thus, if the larger (slower growing) pyramidal planes result in the larger prism planes during Czochralski growth, the internal planes of the long-etched triangular pits must be (1011), (1101) and (0111) planes and thus parallel to the faster growing pyramidal planes. On the other hand, the larger pyramidal planes in the short-etched hexagonal pits may well be the slower growth (1101), (0111) and (1011) planes but the angles here were not measured, due to the very small size of the pits. The correlation of etch planes on the (0001) surfaces with growth planes thus explains the orientation effect. It is suspected that a similar correlation applies to the four-sided pits but this cannot be confirmed until the internal planes have been definitely determined.



50 µm

Fig. 3.1 Four-sided etch pit on the (1010) surface of a tellurium crystal.

c-axis

()

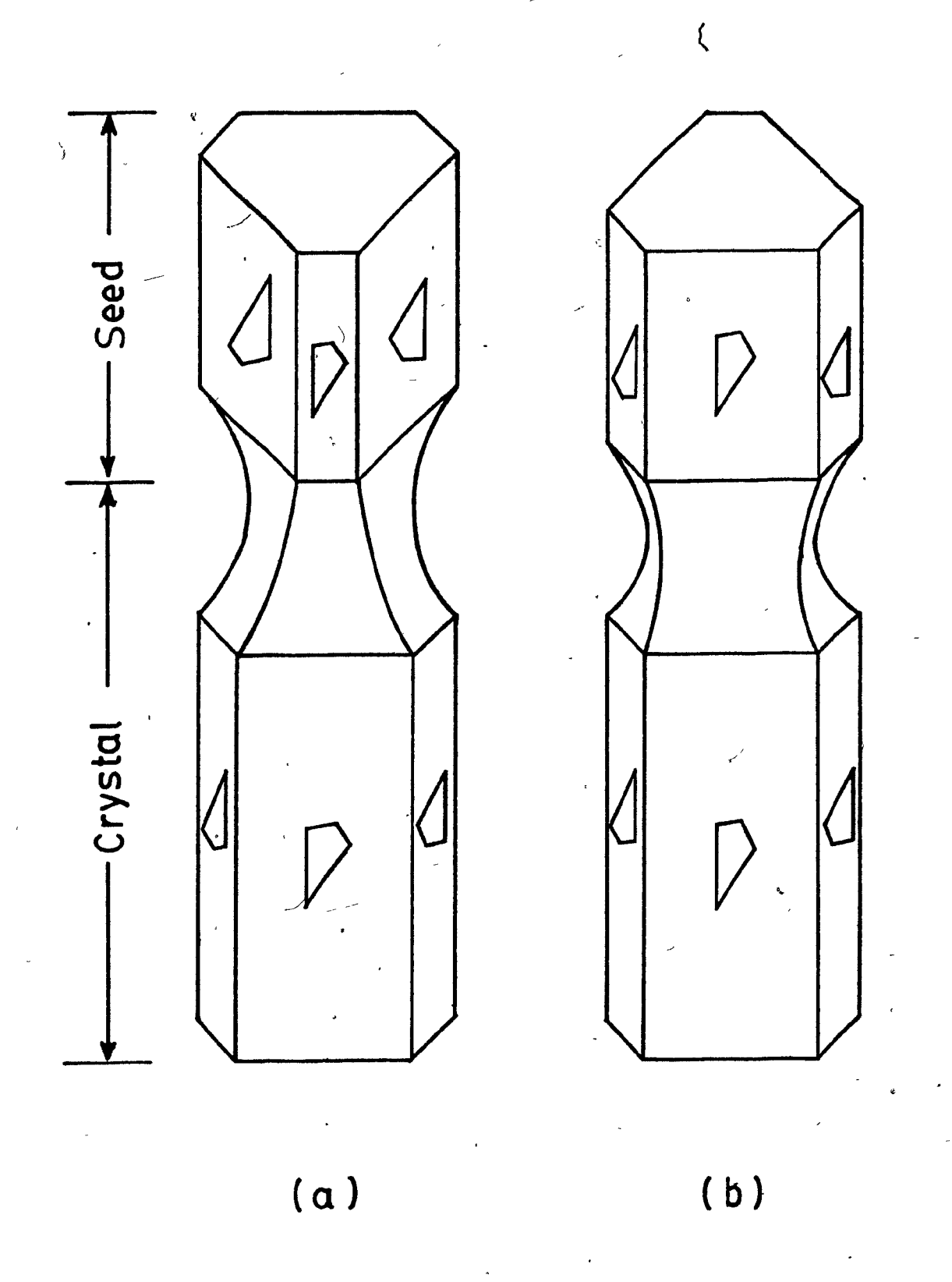


Fig. 3.2 Diagram showing the crystal faces developed from the seed for growth in the c-direction and indicating the orientation of the 4-sided etch pits; (a) growth from an "inverted" seed; (b) growth from a "normal" seed.

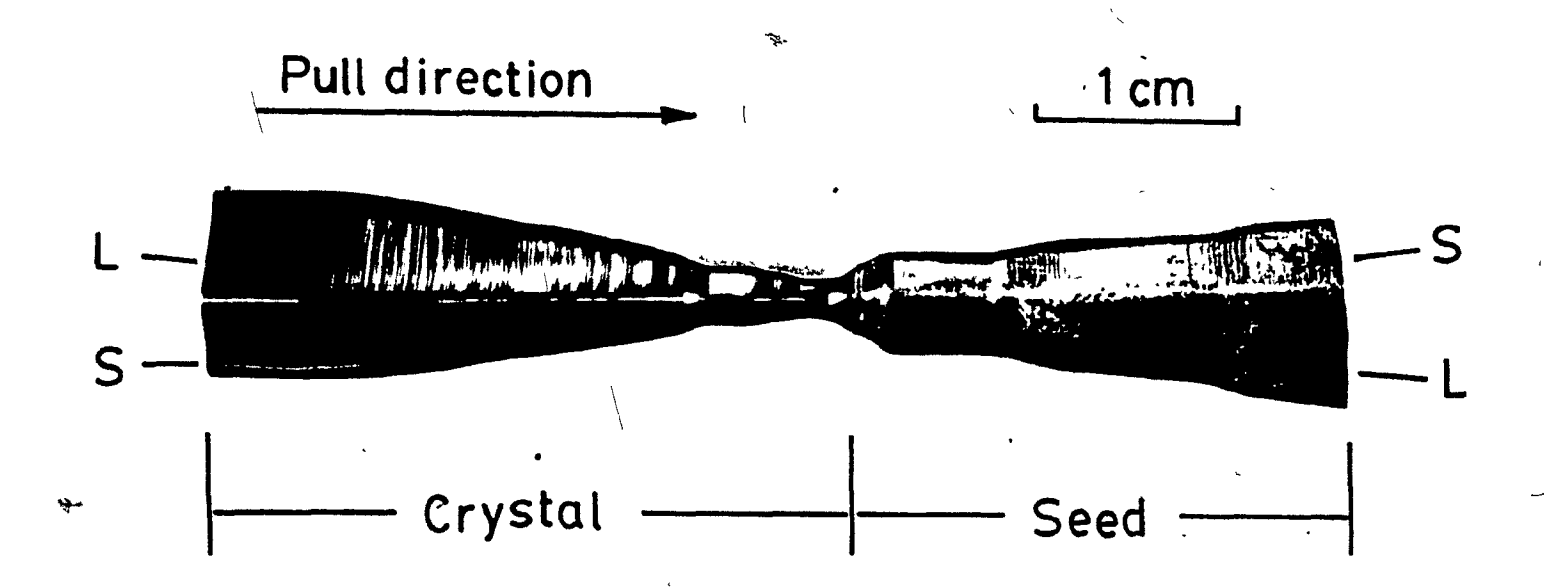


Fig. 3.3 Photograph of a tellurium single crystal grown from an "inverted" seed. It is seen that the large face (L) of the crystal has developed from the small face(S) of the seed.

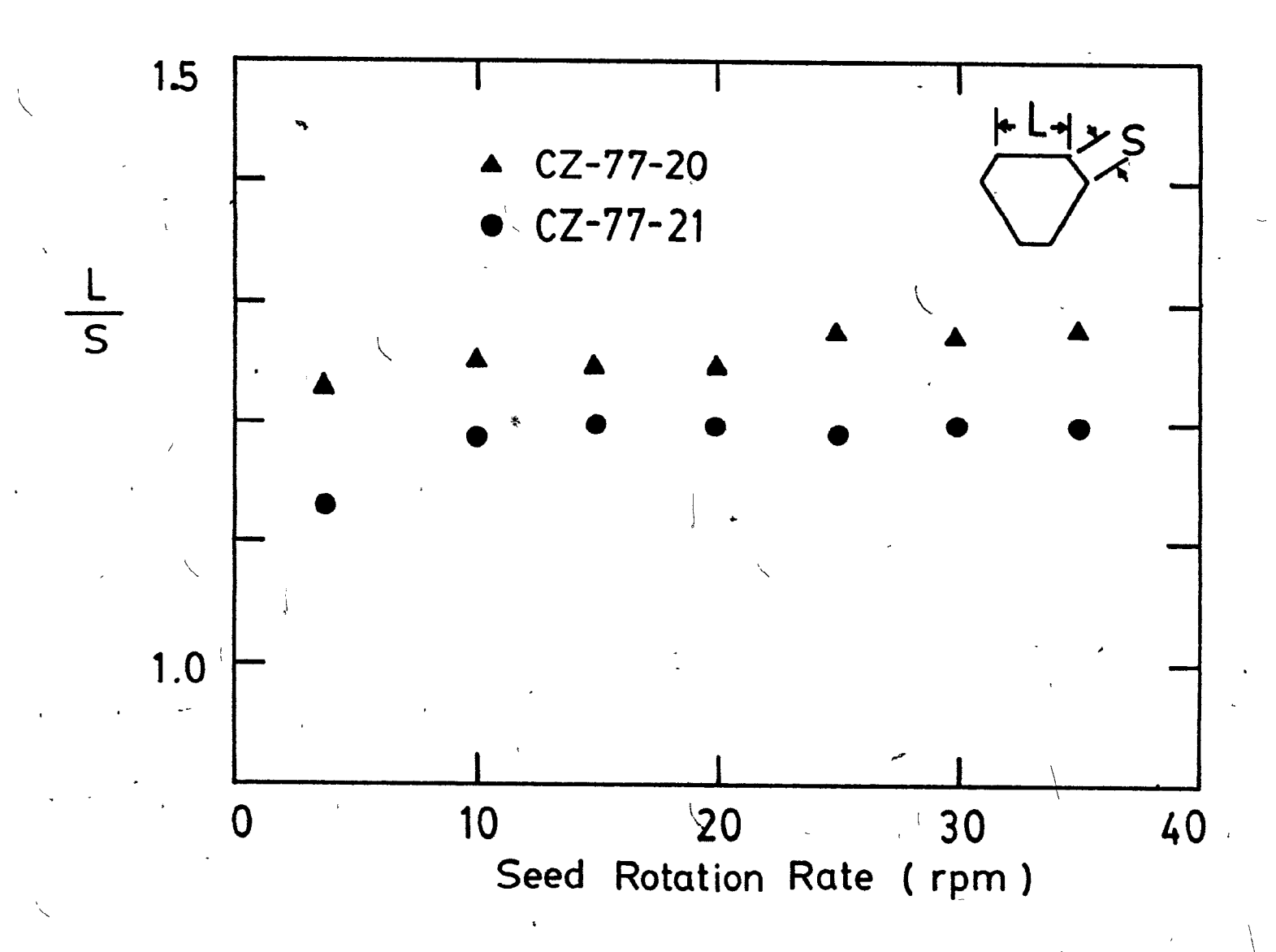


Fig. 3.4 Plot of the ratio of the long face to the short face (L/S) against seed rotation rate for two crystals grown parallel to the c-axis.

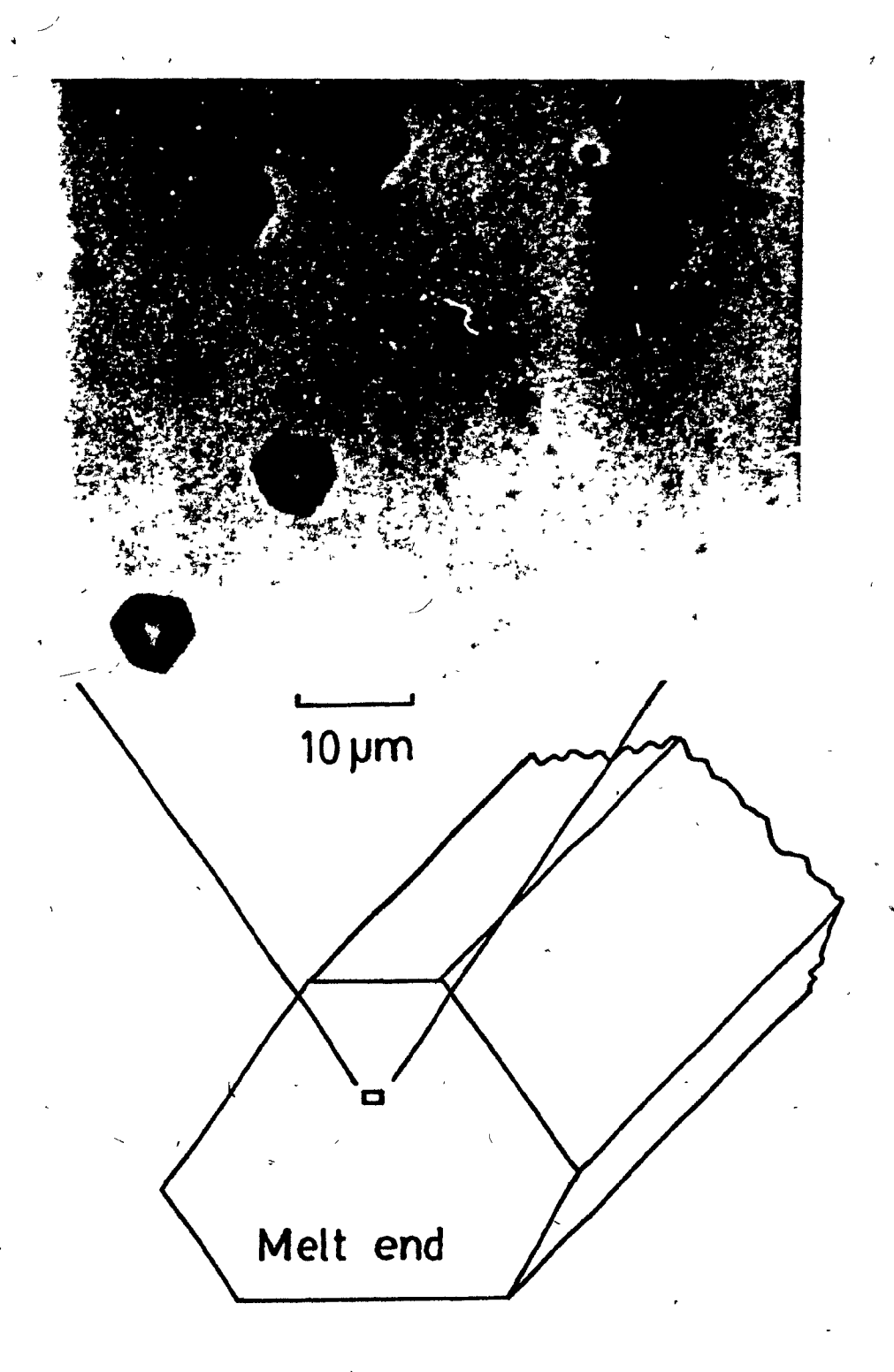


Fig. 3.5 Enlarged view of hexagonal etch pits on the (0001) surface after etching for 20 seconds at 140°C in phosphoric-chromic acid.

 \bigcirc

C

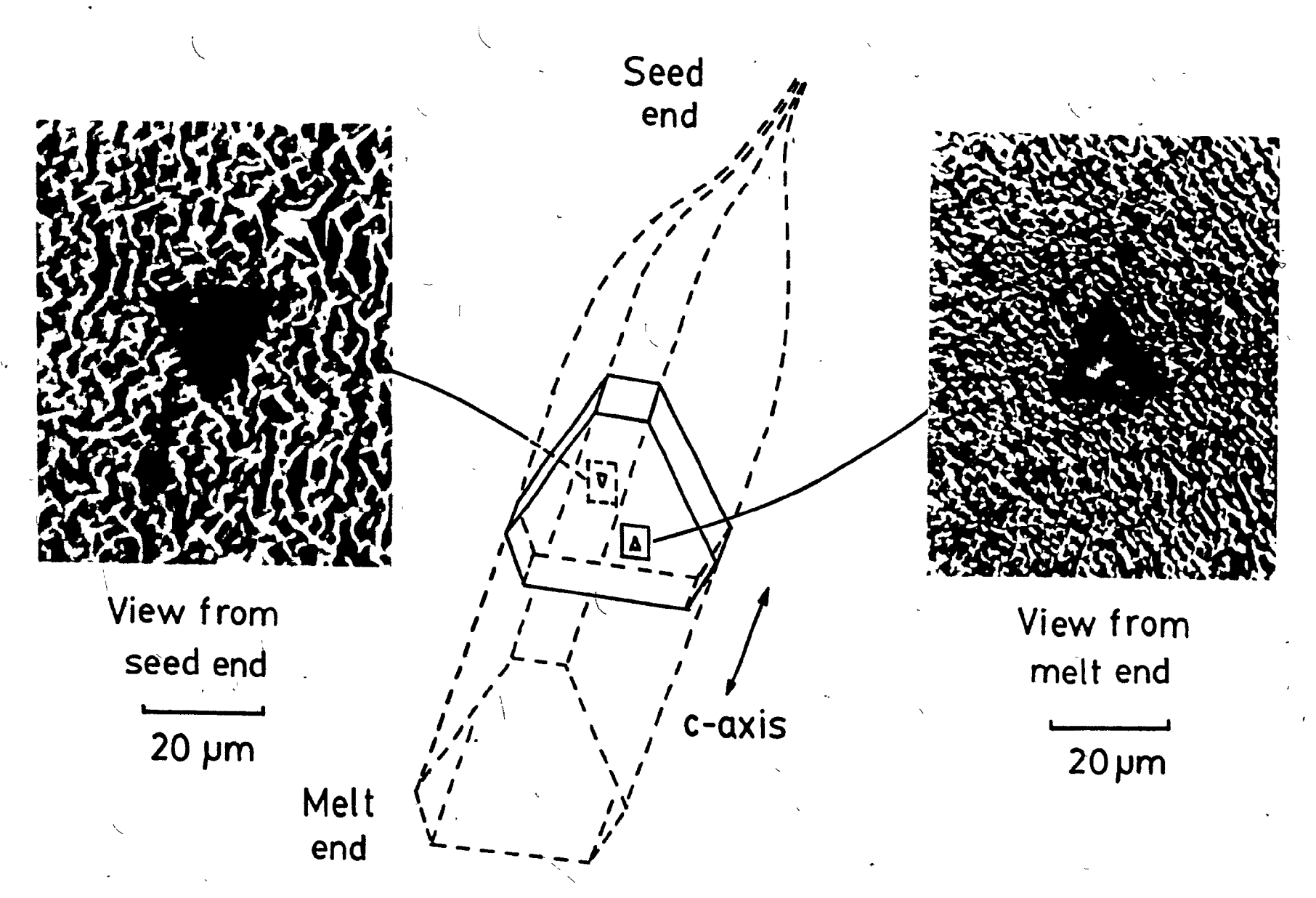


Fig. 3.6 A schematic diagram and photographs showing the orientation of the triangular etch pits on the (0001) surfaces of a c-grown crystal.

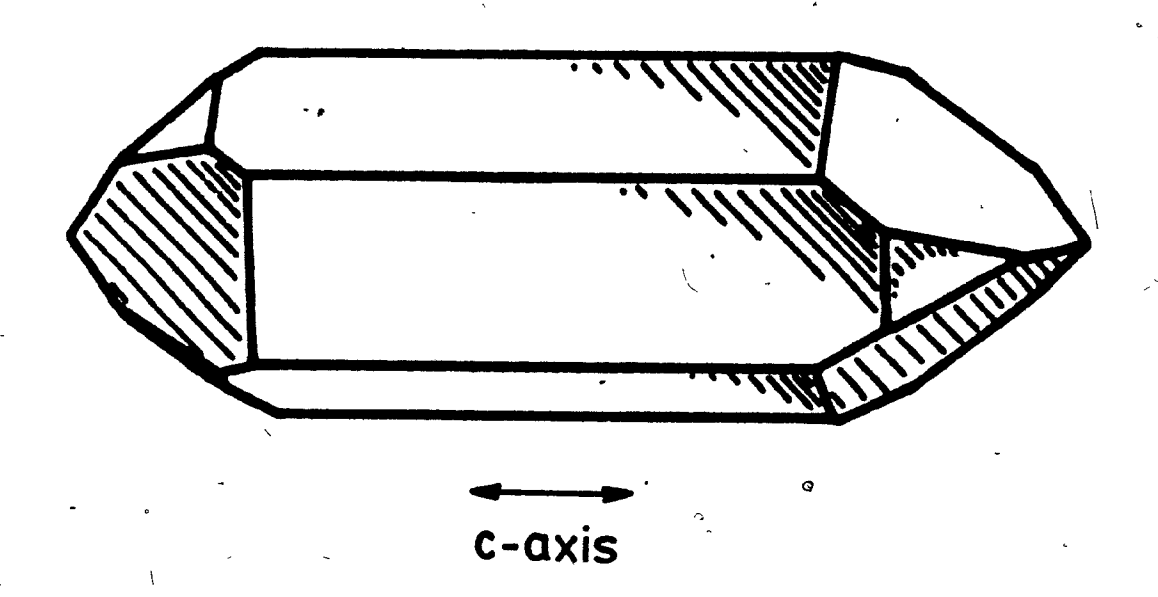


Fig. 3.7 An idealized tellurium crystal grown from the vapor phase (taken from [2.7]).

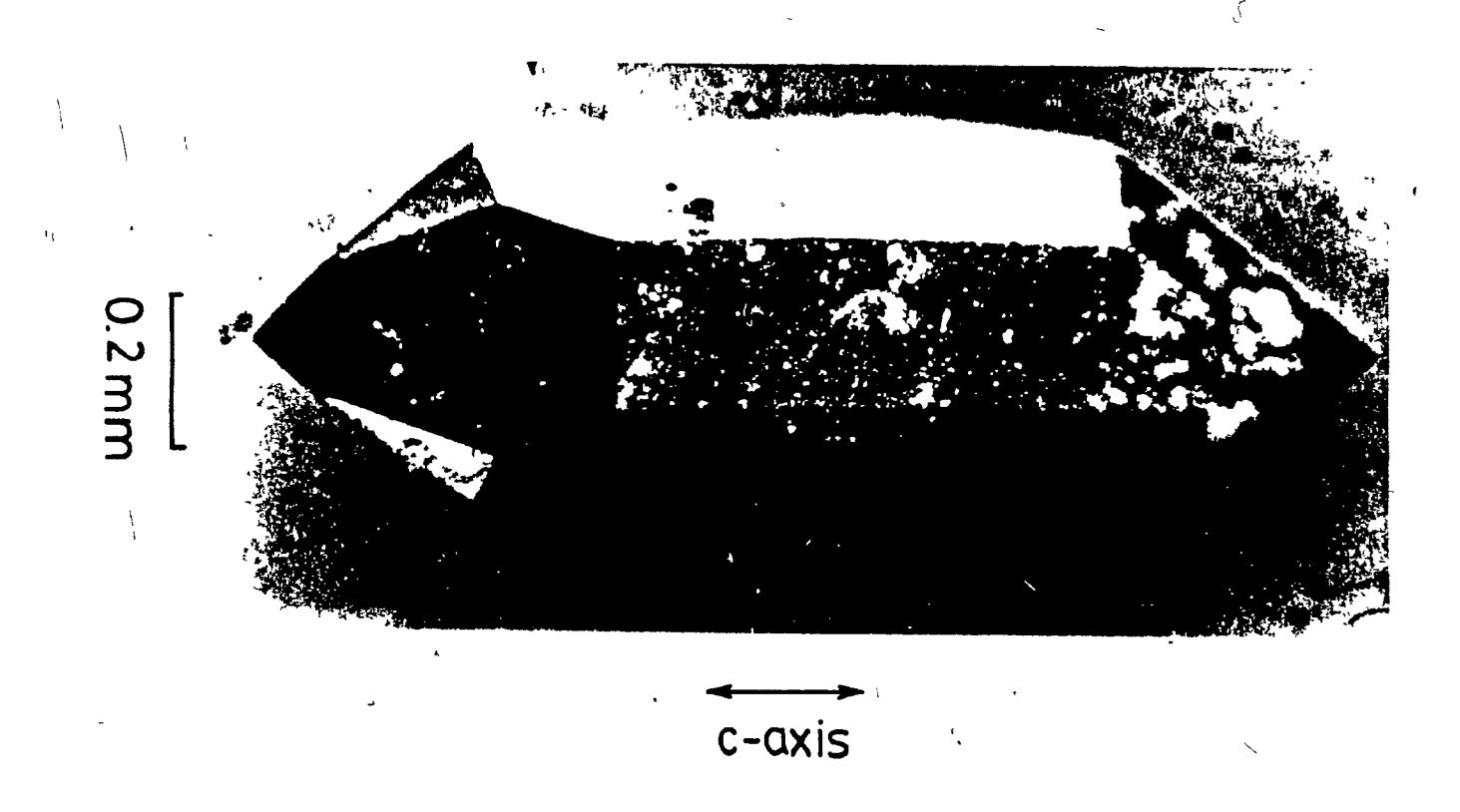


Fig. 3.8 A tellurium crystal grown from the vapor phase showing the growing faces.

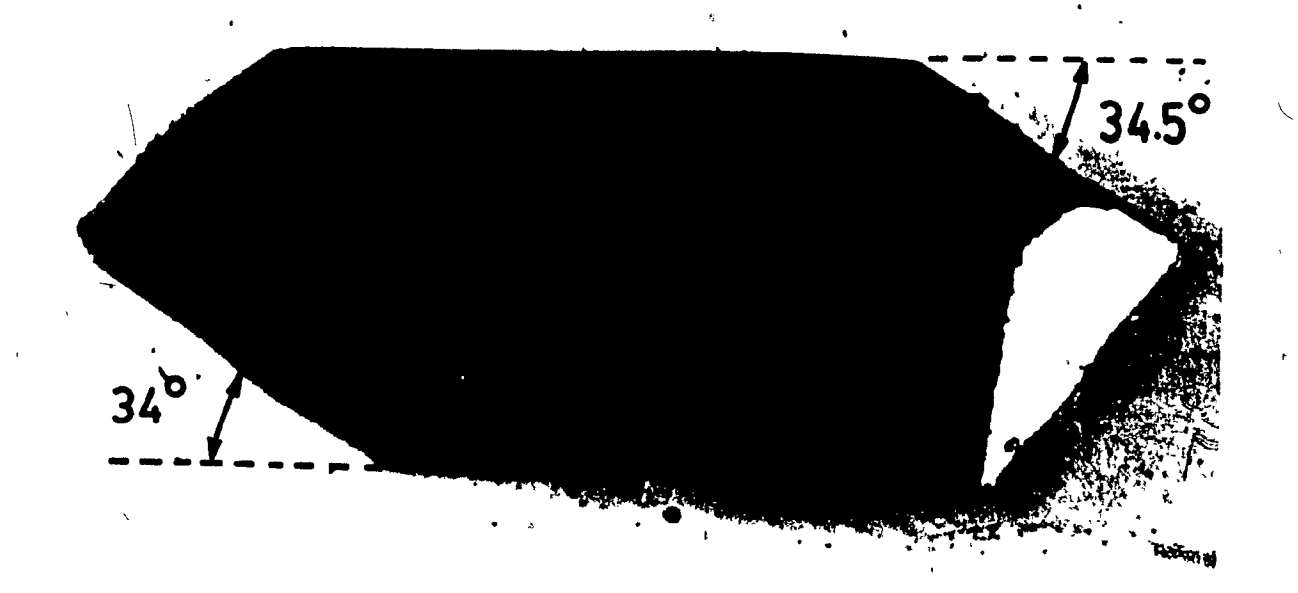


Fig. 3.9 A side view of the vapor-grown crystal of Fig. 3.8 with the angle between the larger growing planes and the (1010) planes measured to be $34\pm0.5^{\circ}$.

CHAPTER 4 EFFECT OF TEMPERATURE GRADIENTS DURING GROWTH OF TELLURIUM

4.1 Introduction

It was briefly described in chapter 2 how, in recent work in this laboratory, a technique was developed for the routine growth of tellurium crystals by the Czochralski method, which gave essentially a 100% yield, by avoiding thermal shock in the seed. At the same time, it is also well known that to obtain the highest values of extrinsic Hall mobility and magnetoresistance at a temperature of 77 K, it is necessary to anneal the tellurium crystals above 350°C for several hours [4.1,4.2]. This process apparently removes point defects which scatter or trap the holes.

It was initially believed by the writer that the improved Czochralski process produced crystals with a low concentration of point defects which were thus in an "annealed" state as grown. However, it was later realized that the Czochralski pulling process inevitably involves temperature gradients and that these might be large enough even under the "best" growth conditions, to cause strains from differential expansion. Work was therefore carried out to estimate the temperature gradients within a growing crystal. The study involved firstly making temperature measurements

within the crystal during special growth runs and comparing these with temperature values calculated from a simplified heat flow model. Secondly, samples were cut from three crystals grown with different temperature gradients arising from different background temperatures. Transport measurements were then made on them at 77 K before and after annealing. The results show that strong temperature gradients do arise during growth and that these introduce defects in the crystal which lower the extrinsic Hall mobility. However, these defects may be removed by subsequent annealing.

4.2 Temperature Distribution During Growth

In a typical Czochralski growth run, heat flows along the growing crystal from the melt and is lost from the ingot surface and through the neck. Temperature gradients therefore must exist within the ingot. To see what magnitude these would be, the temperature distribution was measured during growth of tellurium, as described below. A calculation was then done on the basis of a theory developed by Brice [4.3] and the results compared with the experimentally determined profiles.

4.2.1 Temperature measurements in a growing tellurium crystal

(a) Method

(a)

Į

A c-grown undoped tellurium crystal, about 11 cm)in length and 1.6 cm in width, was specially prepared for the temperature profile measurements. Five 1 mm diameter holes were drilled to various depths in the crystal perpendicular to (1010) planes, as shown in Fig. 4.1. Then insulated calibrated iron-constantan thermocouples, 0.25 mm diameter, were inserted into the holes. The crystal, with these inserted thermocouples, was mounted in the seed holder Czochralski puller. The crystal was then dipped into a melt of undoped tellurium under an atmosphere of argon. After slight melt-back at the start of growth, the position of the crystal was adjusted so that the thermocouples were located about 0.5 above the melt surface. The crystal length was then extended by a further 4.5 cm by vertical pulling at 1.7 cm/hr. The background heater was set so that a thermocouple mounted in the argon was 300°C; this thermocouple was located about 1 cm from the inner Pyrex chamber wall and 5 cm above the plane of the melt surface. Because of the presence of the inserted thermocouples, the crystal could not be rotated. However, the crucible was rotated at 8 rpm. During the run, the temperature the five inserted thermocouples was measured using a Hewlett Packard model 3462A digital voltmeter at different times from the start of the growth. The cold junctions were kept in a stirred ice-water mixture. Following this growth run, the crystal was melted back to the same starting position and a new growth run was made with the same conditions except

that the background temperature was raised to a new value of 360° C. With this completed, a third run was made with the background temperature set at 400° C.

(b) Experimental results

(=)

The temperatures (T) within the ingot, measured at a radial position r=0.6 cm from the central axis, are plotted as a function of the vertical distance (z) from the melt surface in Fig. 4.2 for the three background temperatures of $T_R = 300$, 360 and 400°C. Since the temperatures within the tellurium were recorded at different times, the distance z was taken as the product of pulling rate and time from the start of growth, plus 0.5 cm. It is thus assumed in this plot that the temperature variation along the ingot is independent of time. This will be true if the total heat loss from the ingot does not depend on its length or position in the growth chamber. As expected, the axial temperature decrease with distance is larger at lower background temperature and the largest gradient is near the solid-liquid interface, ie, near z=0. The axial gradients are specifically plotted against log-linear scales in Fig. 4.3, where the values were obtained from a smooth curve drawn through the points in Fig. 4.2. It noted that with a background temperature of 300°C, the gradient near z=0 was of the order of 100°C/cm, which undoubtedly must be considered a large value. Fig. 4.4 shows a

semilogarithmic plot of $T-T_{\rm BF}$ against z, where $T_{\rm BF}$ is a background temperature obtained by fitting equation (4.5) (see section 4.2.2(a)) to the experimental results in Fig. 4.2.

A plot of the measured temperatures as a function of radial position r is shown in Fig. 4.5 for the three background temperatures. The values were taken when the thermocouples were situated at z=10 mm above the melt surface. The plot assumes radial symmetry of the temperatures within the ingot. From smooth curves drawn through the points, radial temperature gradients were determined and these are plotted against r in Fig. 4.6. The largest gradients occur near the ingot surface, where the magnitude for the two lower background temperatures is some $100\,^{\circ}\text{C/cm}$. It should be mentioned that measurement errors are larger in this region.

4.2.2 Calculation of temperature distribution

(a) Theory

 \mathbf{C}

The rate of change of heat in a body per unit time and per unit volume is given by:

$$\rho c_{\mathbf{p}} \frac{\Delta \mathbf{T}}{\Delta t} = K_{\mathbf{c}} \nabla^{2} \mathbf{T} , \qquad (4.1)$$

where ρ , c_p , and K_c are respectively the density, specific heat and thermal conductivity of the material involved. In the case of a growing crystal, Brice [4.3] has considered that steady state thermal conditions apply*, namely $\Delta T/\Delta t = 0$, so that equation (4.1) reduces to $\nabla^2 T = 0$. If the temperature distribution is cylindrically symmetrical, the excess temperature $\theta = T - T_p$ at radius r and height z is obtained from,

$$\frac{\partial^2 \theta}{\partial \mathbf{r}^2} + \frac{1}{\mathbf{r}} \frac{\partial \theta}{\partial \mathbf{r}} + \frac{\partial^2 \theta}{\partial \mathbf{z}^2} = 0 \qquad (4.2)$$

where T_B is the surrounding ambient or background temperature. In Brice's treatment [4.3] the following boundary conditions were assumed to apply (Fig. 4.7) to a circular rod representing the crystal of radius a and length L.

(i) $\theta = \theta_M = T_M - T_B$ at z=0, where T_M is the temperature at the solid-liquid interface,

(ii)
$$K_c \frac{\partial \theta}{\partial r} + \varepsilon \theta = 0$$
 at $r = a$,

(t

^{*} In the case of a crystal growing at a velocity v in the z-direction, the term $\Delta T/\Delta t$ may be taken as $(\partial T/\partial t)+v(\partial T/\partial z)$. Brice [4.3] has indicated that $v(\partial T/\partial z)$ can be neglected if $8 \in K_C/[a(v \circ c_D)^2] >> 1$. In the present case, this inequality is well satisfied with the left hand side having a value of the order of 10^8 .

(iii)
$$K_C = \frac{\partial \theta}{\partial z} + \epsilon \theta = 0$$
 at $z = L$,

where $\epsilon\theta=\epsilon(T-T_B)$ is the rate of heat loss per unit area from the surface of the rod arising from radiation, convection and conduction into the surrounding gas. In condition (iii), conduction through the crystal neck is neglected.

With these boundary conditions the solution of equation (4.2) is [4.3,4.4]:

$$\theta = \theta_{m} \sum_{n=0}^{\infty} \frac{2h}{a(h^{2} + \alpha_{n}^{2})} \frac{J_{o}(r\alpha_{n})}{J_{o}(a\alpha_{n})} \frac{\alpha_{n} \cosh[\alpha_{n}(L-z)] + h \sinh[\alpha_{n}(L-z)]}{\alpha_{n} \cosh[\alpha_{n}L] + h \sinh(\alpha_{n}L)}, \quad (4.3)$$

where h= ϵ/K_{C} , J is a zero order Bessel function of the first kind and α_n represents roots of the equation

$$\alpha_n J_O'(\alpha_n a) + h J_O(\alpha_n a) = 0 . \qquad (4.4)$$

Here J' is the derivative of Jo. If $\alpha_n^2 \gg h^2$ and (L-z) $\gg \alpha_n^{-1}$, then it can be shown that equation (4.3) reduces to,

$$\theta = \theta_{\rm m} \frac{1 - (hr^2/2a)}{1 - (ha/2)} \exp[-(2h/a)^{1/2}z] , \qquad (4.5)$$

indicating an exponential decréase of temperature along the ingot axis.

(b) Estimation of h

Calculation shows that in the present case the surface heat loss coefficient h has contributions from conduction and convection in the argon gas surrounding the ingot which can be neglected in comparison with the effect of radiation. The net rate of radiative heat exchange between two concentric cylinders of radii r_1 and r_2 having respectively temperatures r_1 and r_2 and emissivities r_1 and r_2 is given by [4.5]:

$$j_{Q,rad} = \frac{\bar{\sigma}_{Q}}{\frac{1}{e_{1}} + \frac{r_{1}}{r_{2}}(\frac{1}{e_{2}} - 1)} (T_{1}^{4} - T_{2}^{4}) , \quad (4.6)$$

where σ_0 is the Stefan-Boltzmann constant.

In the present work, the average radius of the tellurium crystal (hexagonal cross-section) was r_1 =0.8 cm and its emissivity is e_1 =0.56 [4.6]. The corresponding values for the cylindrical Pyrex growth chamber were r_2 =4.75 cm and e_2 =0.85 [4.7]. During the run with a 360°C background temperature ie. T_2 =633 K, the average temperature at the surface of the ingot was found to be T_1 =655 K. Substituting

these numbers, together with $K_c = 5 \times 10^{-3}$ cal cm⁻¹sec⁻¹ K⁻¹ for tellurium at 500 K [4.6] into equation (4.6) gives the following value for h,

$$h = \frac{j_{Q,rad}}{(T_1 - T_2) K_C} \approx 0.2 cm^{-1}$$

(;

Despite the T⁴ dependence in equation (4.6), calculation shows that a 40% change in T_1 - T_2 gives only a 3% change in h, so that practically speaking, this value can be taken as constant for the fixed background temperature T_2 .

(c) Comparison of experimental and calculated profiles

Using h=0.2 cm⁻¹ and a=0.8 cm, equation (4.4) was solved numerically to obtain values for α_n . On substituting these values into equation (4.3) with r=0.6 cm and L=5.5 cm, it was found that the second (n=1) and higher order (n>1) terms were less than 5% of the first (n=0) term for all values of z. Thus only the first term was important. Further, since $(\alpha_0/h)^2 \approx 10$ and $L\alpha_0 \approx 4$, equation (4.5) was used to fit the experimental results in Fig. 4.2. Each curve was fitted with two parameters $T_{\rm BF}$ the background temperature and $T_{\rm MF}$ the temperature at z=0. The resulting $T_{\rm BF}$ values are seen to lie 20 to 30° above the measured background temperatures $T_{\rm B}$, while the $T_{\rm MF}$ values are 7 to 27° below the melting point of

tellurium (452°C). The lines indicated in Fig. A.3 were also calculated with these values of $T_{\rm BF}$ and $T_{\rm MF}$. While these calculated lines describe the trend of the experimentally determined gradients, the absolute agreement with them is only fair. In Fig. 4.4 calculated lines 'are also shown using the same $T_{\rm BF}$ and $T_{\rm MF}$ values in the exact equation (4.3) and the approximate equation (4.5). It is clear that the difference between them is small and that the experimental values of $T-T_{\rm BF}$ decrease approximately exponentially with z.

(

Calculated curves using the same T_{BF} and T_{MF} parameters are shown for the radial temperature and temperature gradient distribution in Figs. 4.5 and 4.6. It is apparent here that the agreement with the experimental points is not good.

The discrepancy between the experimental and calculated profiles arises from over-simplified boundary conditions in the Brice theory. In the present case the constant background temperature assumptions of negligible heat loss through the crystal neck may not be valid. Some of the disagreement must be due to error in temperature measurement from heat losses along the thermocouple wires. Never-the-less, the measurements do give the magnitude of the temperature gradients in the tellurium

crystal during growth.

4.3 Crystal Growth and Transport Measurements

4.3.1 Crystal and sample preparation

Three complete single crystals were grown under the same background temperatures of 300, 360 and 400°C employed in the runs described in section 4.2.1 but without the inserted thermocouples and with rotation of the seed at 6 rpm. A photograph of the three crystals is shown in Fig. 4.8. In each case, the crystal was expanded from the seed, after the start of growth, to a constant diameter of about 1.6 cm, which was maintained for 1.5 hours with a pull rate of 1.7 cm/hr. The diameter was then gradually reduced to about a millimeter over a period of about 2 hours. This tapering was done to avoid the effect of the sudden temperature fall when the ingot is separated from the melt. After the melt separation, the crystal was gradually cooled to room temperature over a period of about 4 hours.

Two rectangular samples, having approximate dimensions of 2x1x8 mm³, were cut from each crystal using an acid saw. One sample was cut with its long axis parallel and the other perpendicular to the c-direction, as indicated schematically in the inset to Fig. 4.9. Each sample was etched in a mixture

of CrO₃:HCl:H₂O, in the ratio 1:1:2 by weight, for about 5 minutes to remove surface layers. This was followed by a 3 minute immersion in 30% HCl solution and a rinse in deionized water. Platinum wires, 0.002 inch in diameter, were attached to each end using solder of composition 50%Sn, 47%Bi, and 3%Sb for current leads. For voltage probes, two platinum wires of the same diameter were melted into one side of the sample and one into the other. The sample was then mounted in a Teflon holder and placed in a dewar between the poles of a conventional electromagnet for transport measurements.

4.3.2 Transport measurements

()

With a current (I) of 0.2 mA through the sample and a "weak" transverse magnetic field of 4 kG, Hall coefficient ($R_{\rm H}$) and electrical conductivity (σ) were measured at 77 K. Transverse magnetoresistance ($\Delta\rho/\rho_{\rm O}$) was also measured at 9 kG. The apparent extrinsic hole concentration $p_{\rm O}$ was taken as $1/(R_{\rm H}q)$, where q is the electronic charge, and the hole mobility as $R_{\rm H}\sigma$. Anisotropy was confirmed for σ (between I parallel or perpendicular to the c-axis) but essentially no anisotropy was found for $R_{\rm H}$.

It was assumed that the maximum axial and radial temperature gradients experienced by the samples during growth were the same as those measured in the first part of this

chapter (section 4.2). With this assumption, p_0 is plotted against maximum temperature gradient in Fig. 4.9 for each of the three background temperatures. It is seen that p_0 increases with decrease of temperature gradient, either axial or radial. Fig. 4.10 shows a plot of $R_{\rm H}\sigma$ against maximum temperature gradient. Because of the anisotropy of σ , two sets of $R_{\rm H}\sigma$ values are plotted. In either case it is evident that the Hall mobility product decreases with increase of gradient.

Extrapolation of the trend to the ordinate in Fig. 4.10 indicates an R_H^{σ} value, for I parallel to c-axis, of some 5,000 cm 2 volt $^{-1}$ sec $^{-1}$. This would seem to correspond to a crystal grown with no temperature gradients and thus no thermal stresses. However, higher values have been reported [4.1,4.2] in the literature for tellurium after annealing, so that it would appear that not all the carrier-scattering defects are gradient-related. For instance, imperfections can result from fluctuations of the solid-liquid interface due to flow instability of the melt [4.8].

4.3.3 Annealing experiments

()

For annealing experiments, a further tellurium piece was cut from each of the three crystals. Each of these was placed in a quartz ampoule and sealed off under argon gas at a pressure of 300 Torr. The ampoule was then placed in a

Lindberg Heviduty furnace and the temperature increased to 390 °C over a period of about 3 hours. It was then maintained at this temperature to within ± 2 °C for 150 hours, following which the temperature was reduced to room temperature over about 24 hours. The ampoule was then broken open and a Hall sample was cut from the annealed piece in such a way that none of the original surfaces of the piece formed the faces of the sample for measurement. Hall coefficient, electrical conductivity and transverse magnetoresistance were then measured on each of the three samples. The results are given in Table 4.1.

Ci

It is noted from the table that for all three background temperatures during growth, annealing produced an increase of the Hall mobility by about a factor of two. Transverse magnetoresistance was also increased but by a smaller amount. The direction of change of p_O was not as consistent but the final value after annealing was essentially the same for all three samples.

4.4 Discussion and Conclusions

The present studies clearly show that to avoid defects which affect the extrinsic transport properties, it is not enough to grow a tellurium crystal under the "best" conditions; it is also necessary to give the material a

subsequent annealing treatment. In this case, $R_{\mathbf{r}^{\sigma}}$ values approaching about 10,000 cm²volt⁻¹sec⁻¹ (for I //c) can be obtained at 77 K. The interpretation of the transport results after annealing does not appear to be simple because the increase in Hall mobility is not accompanied by a large increase in magnetoresistance, as would be expected from a one-carrier theory. Never-the-less, since both $R_{\mu\sigma}$ and $\Delta\rho/\rho_{\alpha}$ increase, it appears that the heat treatment reduces the The relatively small concentration of the point defects. change in the magnetoresistance suggests that the mean free path of the carriers is only little affected. in Hall mobility is thus due to a macroscopic mobility increase, which could arise from a decreae in the density of traps rather than of microscopic scattering centres of the holes.

0

The decrease of Hall mobility with decrease of background temperature during growth is thus interpreted as an increase in the concentration of scattering or trapping centres. This in turn is ascribed to the increase in maximum temperature gradient within the ingot with decrease of background temperature, as established in the first part of this chapter. Imperfections would be created by stresses from differential expansion in a strong temperature gradient. An alternative explanation is that, with a lower background temperature, the rate of cooling with time is more rapid

during growth and that this causes a quenching-in of defects created at higher temperature.

Ö

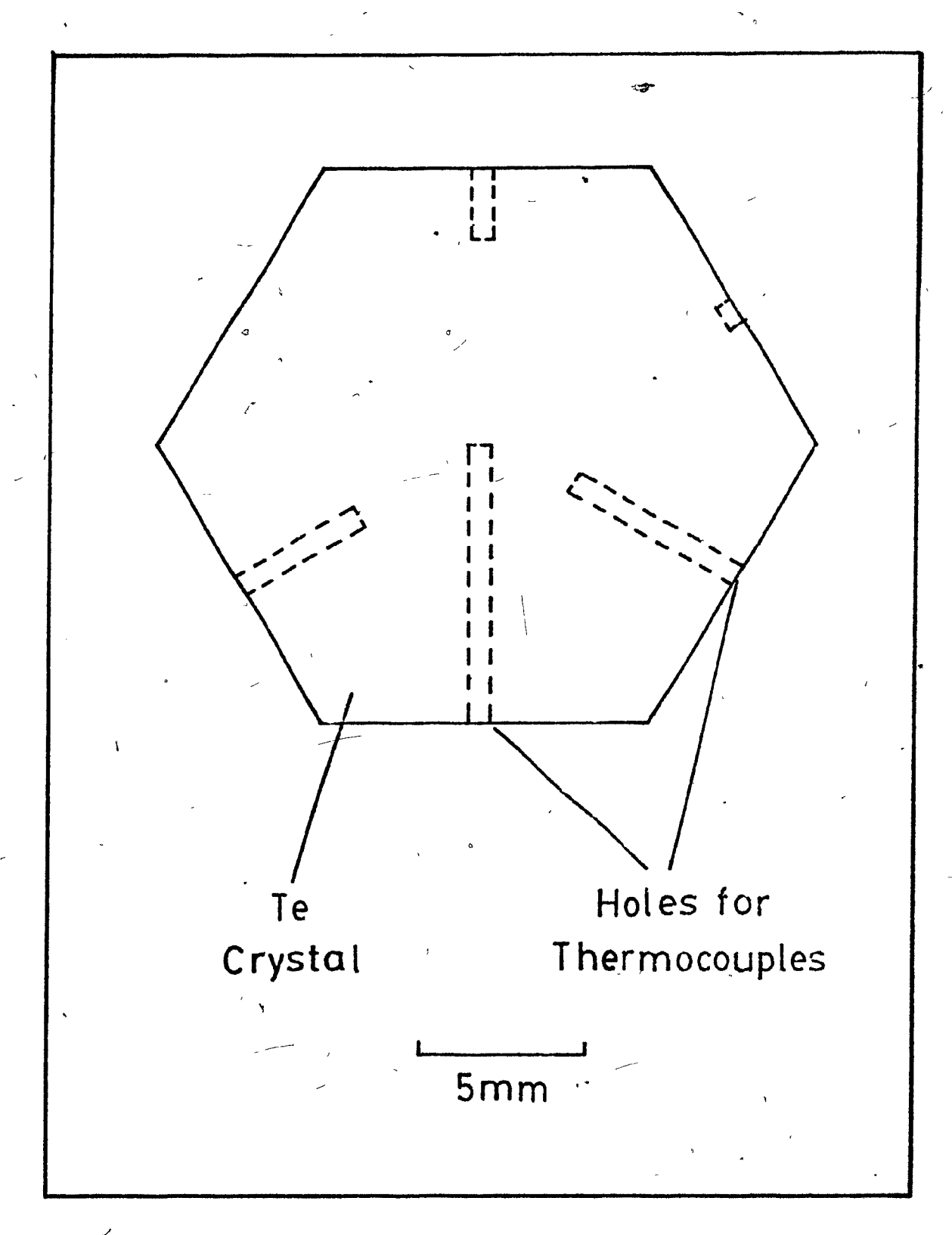
In the first part of this chapter there was only limited agreement between temperature profiles measured and calculated. The discrepancy between theory and experiment is due probably to over-simplification in the boundary conditions of the theory. However, a closer agreement was not pursued in this area of the study since the intention was only to verify the magnitudes of the measured gradients.

Table 4.1

Transport Parameters on Annealed and Unannealed Samples.

Sample No.	Annealed *	R _H o** at 4 kG (cm ² volt ⁻¹ sec ⁻¹)	$p_o = 1/R_H^e$ at 4 kG $(10^{14} cm^{-3})$	Δρ/ρ ₀ at 9 kG (%)	Crystal Growth Conditions	
					Background Temperature, (°C)	Maximum Axial Gradient, (°C/cm)
			· ·			
78-10-2	No	2,750	1.09	7.8	200	1
78-10-5	Yes ·	6,510	1.29	8.4	300	120
78-11-2	No	*3,940	1.54	7.3	. 360	70
78-11-5	Yes	9,420	1.24	9.0		
78-12-2	No	4,230	3.69	8.4		20
78-12-5	Yes	8,560	1.25	10.5	400	

^{*}At 390°C for 150 hours. ** I//c



C}

Fig. 4.1 Cross-sectional view of the Czochralski-grown tellurium crystal used for temperature profile measurements, showing the five holes drilled to receive thermocouples.

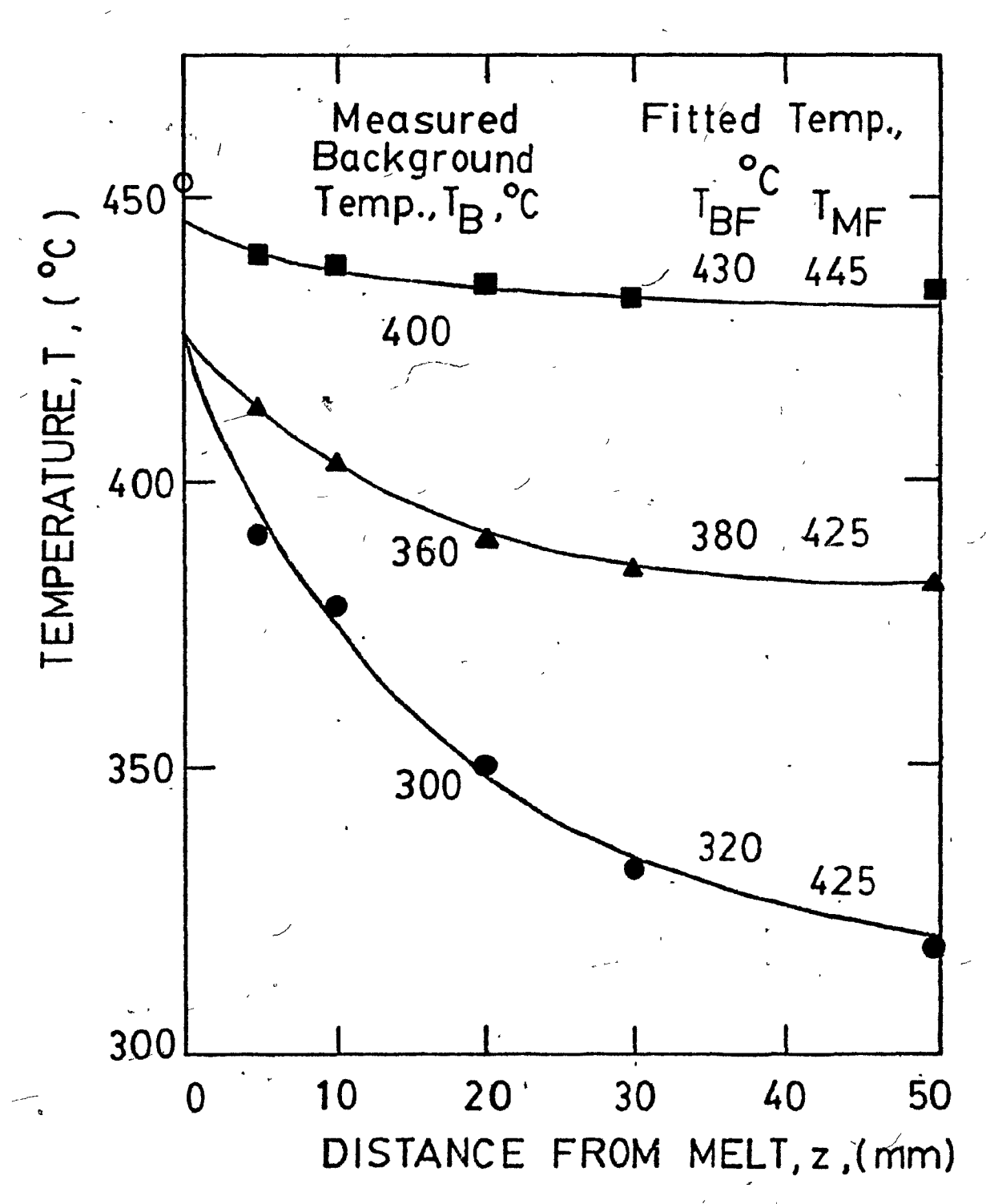


Fig. 4.2 Temperature, measured at r=0.6 cm within a tellurium ingot during extension of its length by Czochralski growth, plotted against z, the vertical distance from the solid-liquid interface, for three different background temperatures. The solid lines correspond to equation (4.3) with the parameters T_{pp} and T_{pp}.

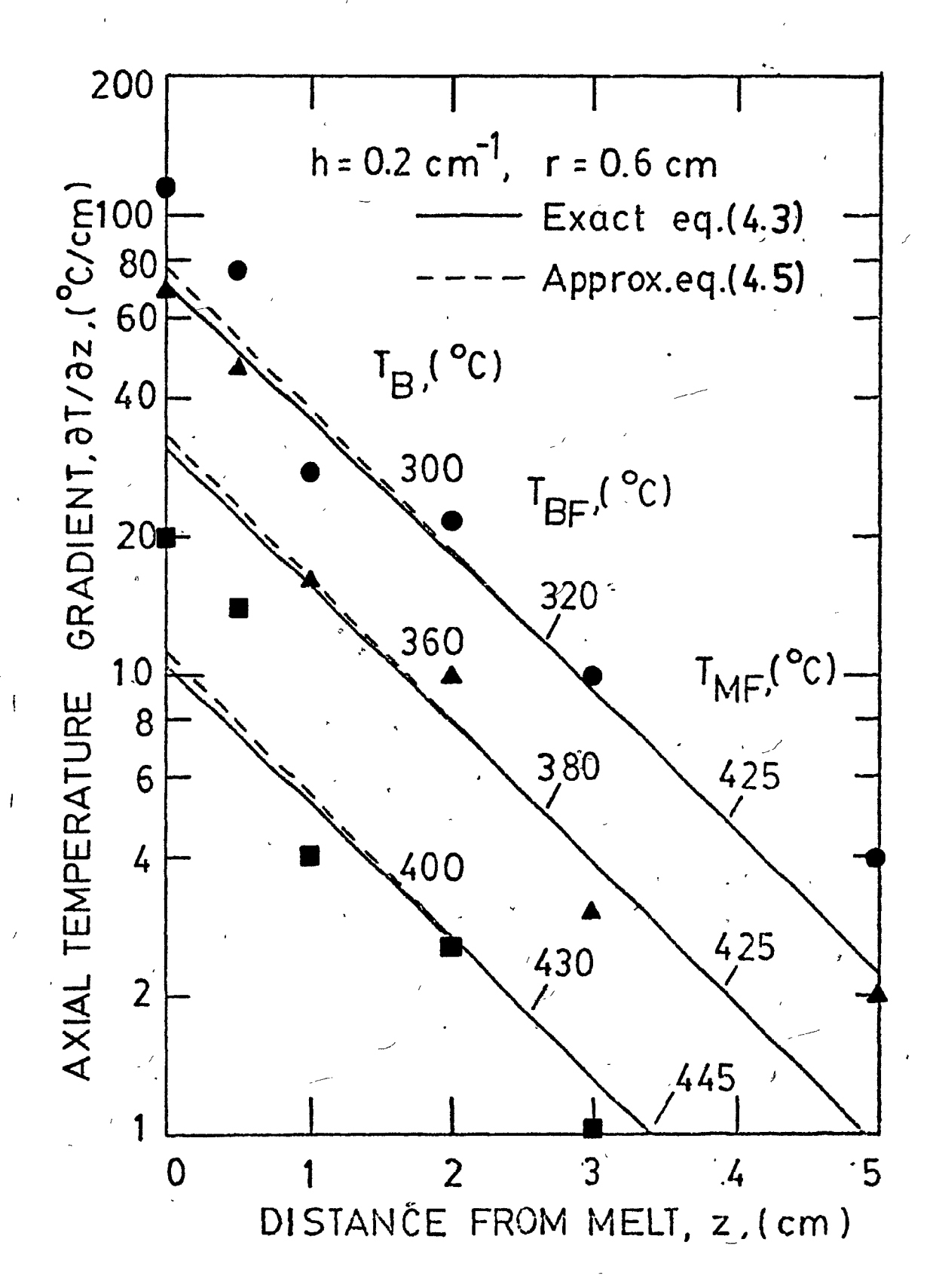


Fig. 4.3 Axial temperature gradient within tellurium ingot, obtained from a smooth curve through the points of Fig. 4.2, plotted against z, for the three background temperatures. The solid lines correspond to equation (4.3) and the broken lines to approximate equation (4.5); the parameters, T and T, are from the fit in Fig. 4.2.

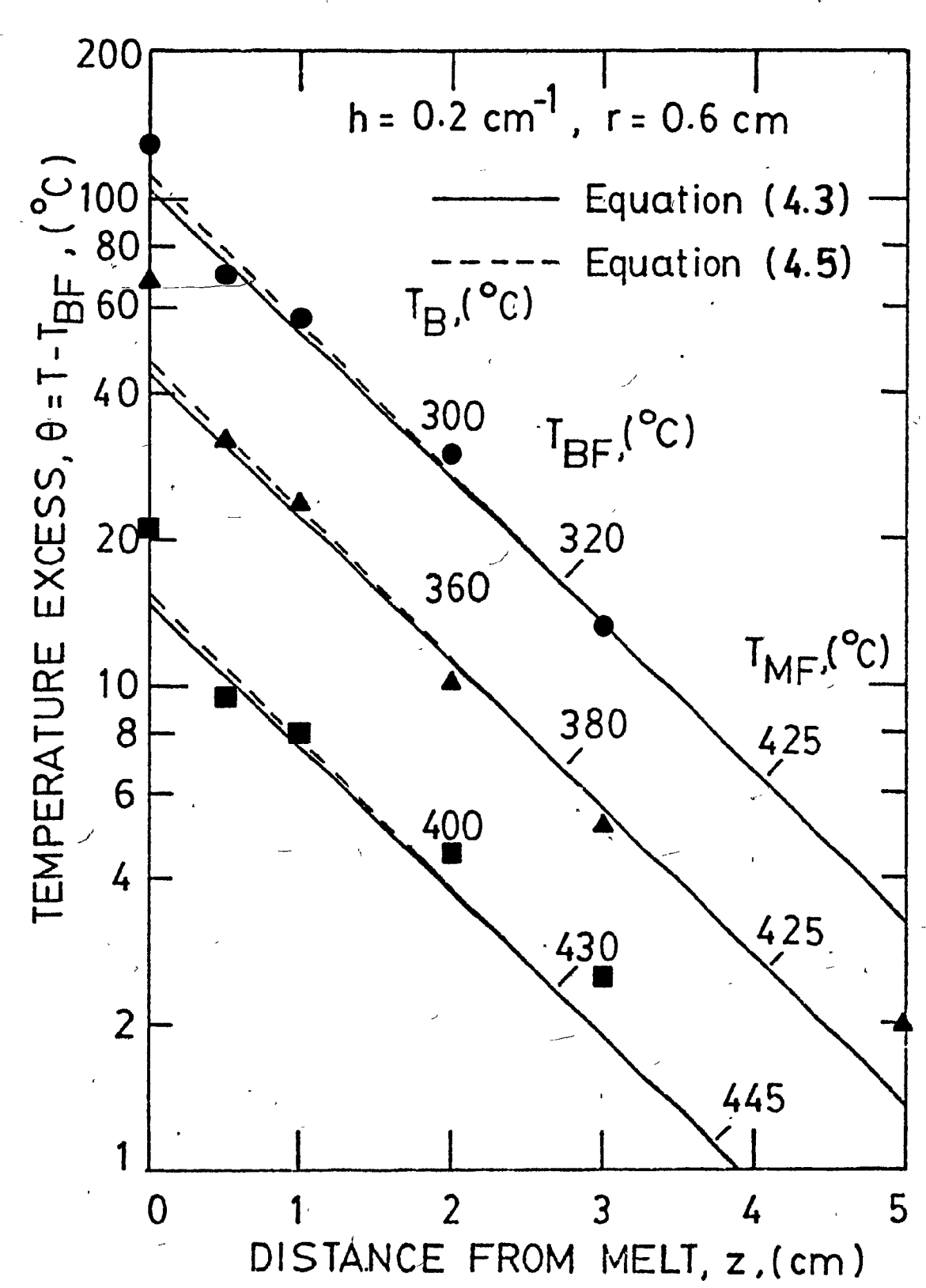


Fig. 4.4 Plot of T-T_{BF}, the excess temperature over the fitted background temperature, against z. The solid lines correspond to equation (4.3) and the broken lines to approximate equation (4.5), with the fitted parameters T and T from Fig. 4.2.

BF MF

0

(i

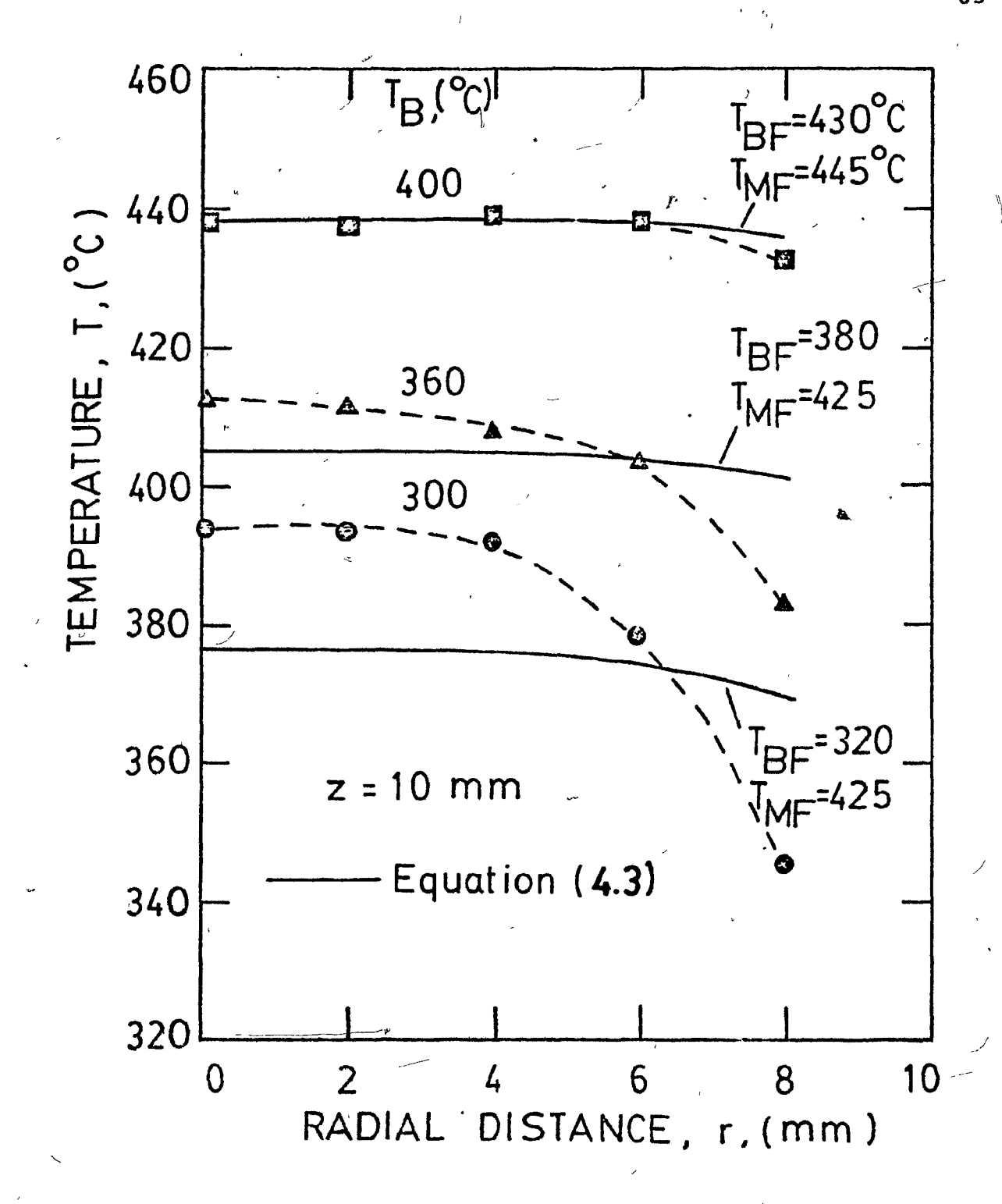


Fig. 4.5 Temperature, measured at z=1 cm within tellurium ingot during extension of its length by Czochralski growth plotted against r, the radial distance from the ingot centre, for three background temperatures. The solid lines correspond to equation (4.3) with the parameters TBF and TMF from Fig. 4.2. The broken lines are smooth curves through the experimental points.

(

0

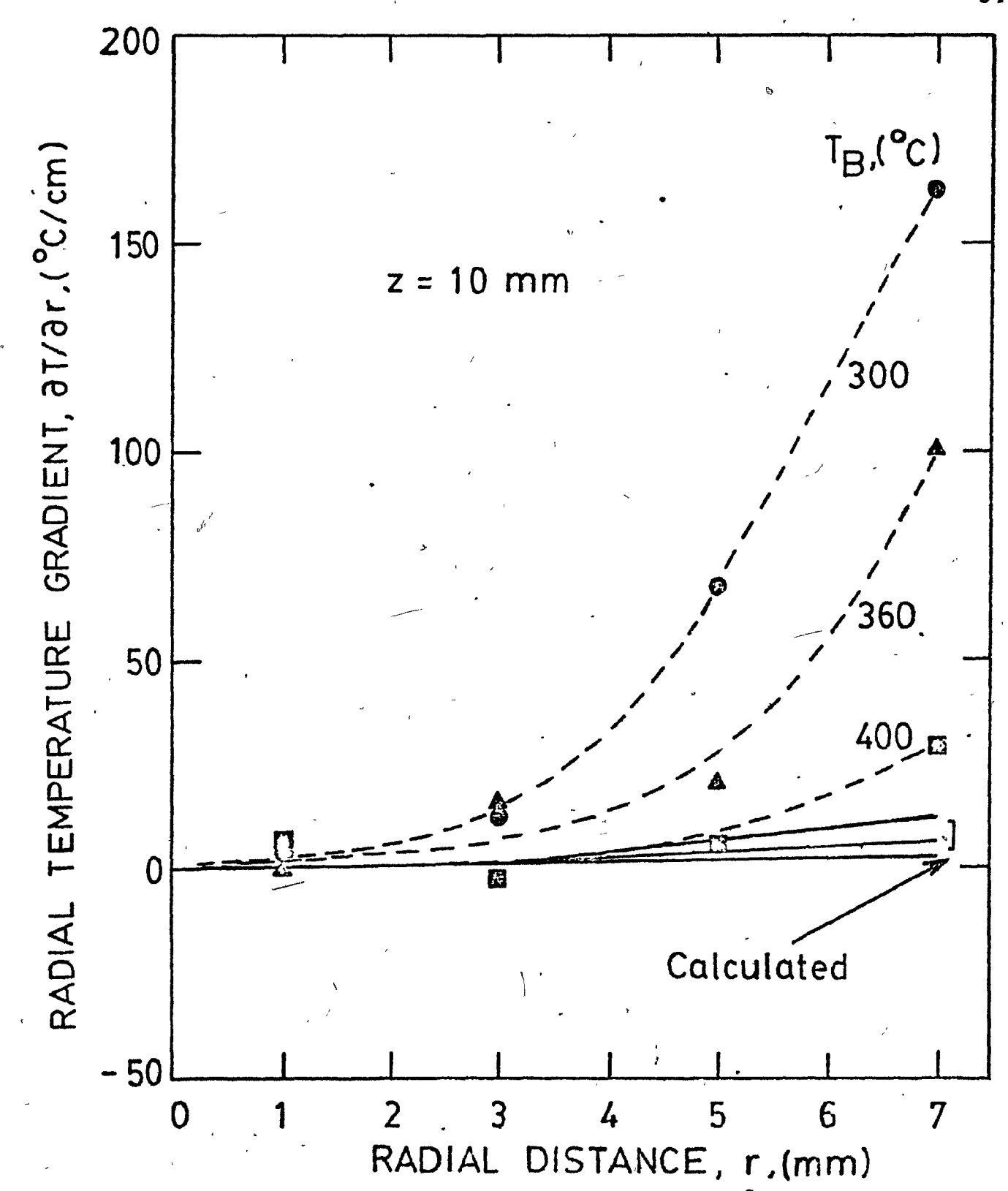


Fig. 4.6 Radial temperature gradient, at z=1 cm, determined from Fig. 4.5, plotted against r for the three background temperatures. The solid lines are calculated from equation (4.5) using the parameters taken from Fig. 4.2. The broken lines are smooth curves drawn through the experimental points.

0

O

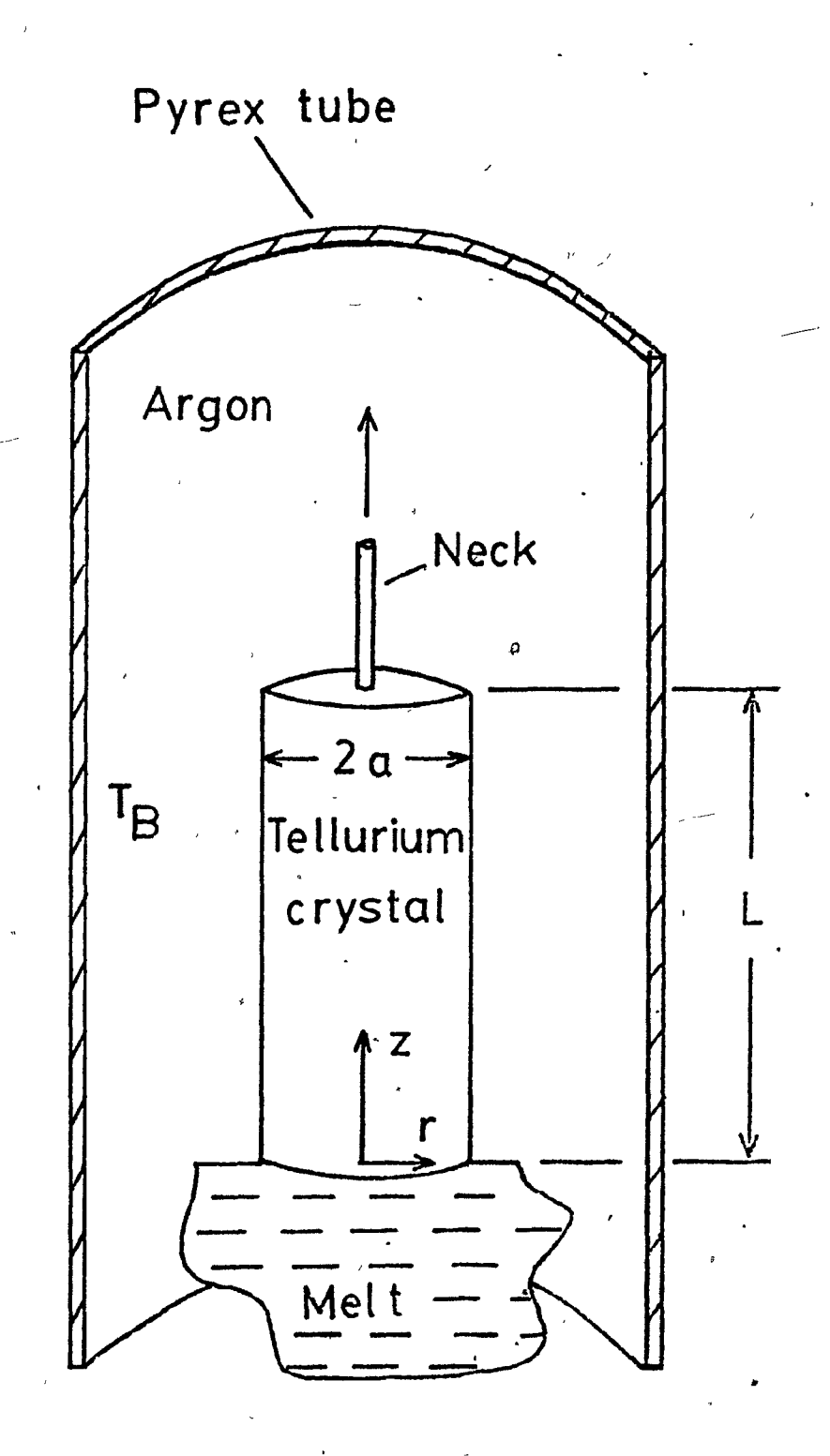


Fig. 4.7 Schematic view showing the axes and dimensions of the growing crystal.

2 cm CZ-78-12 CZ-78-11 CZ-78-10 T_B=400°C TB=3.60°C TB=300°C

Fig. 4.8 Photograph of the three tellurium crystals Czochralski-grown with background temperatures of 300, 360 and 400°C. The tapered ends were so grown to minimize thermal shock on separation from the melt.

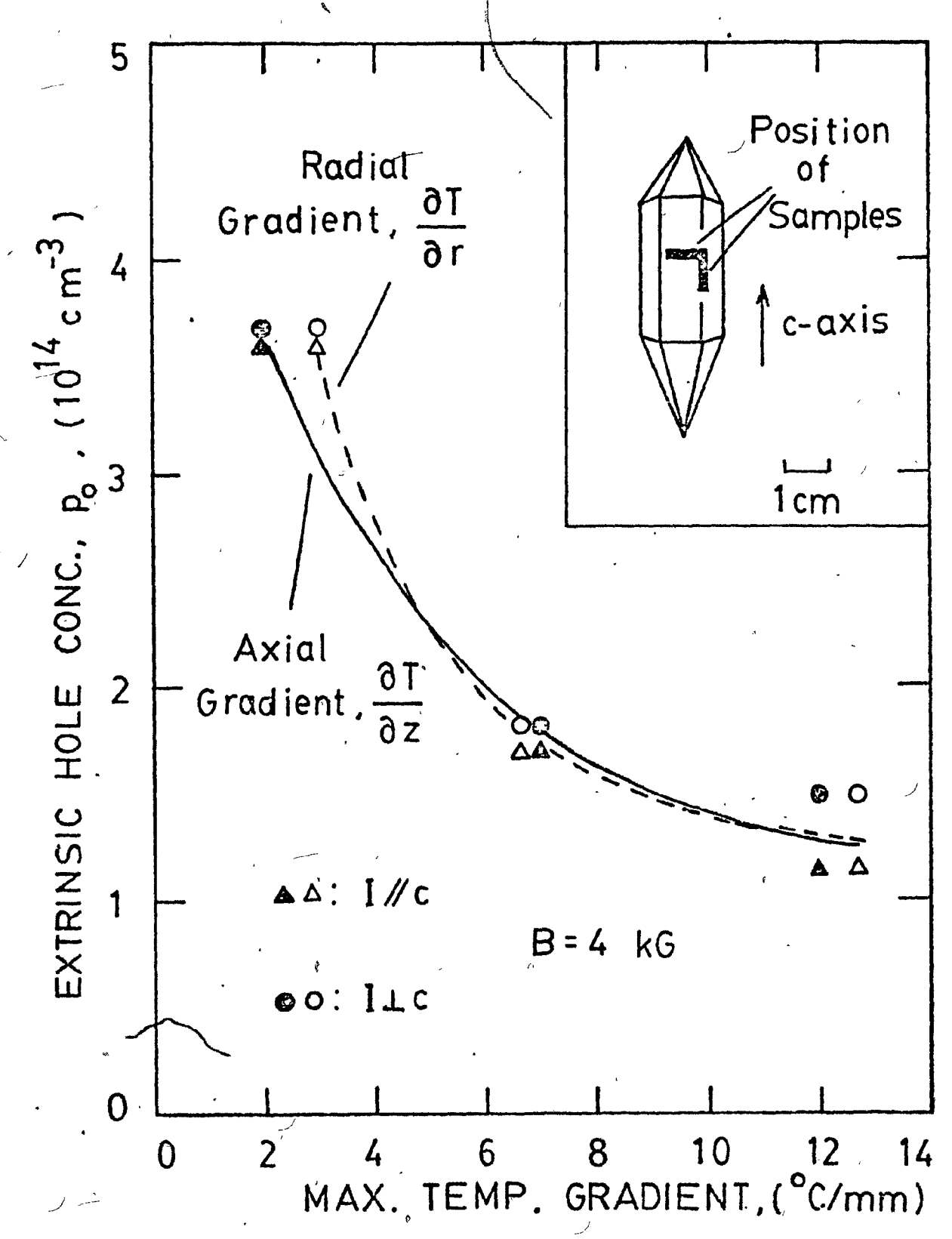


Fig. 4.9 Extrinsic hole concentration, p_0 (=1/ $R_{\rm H}q$), measured on samples cut from ingots shown in Fig. 4.8 (positions shown in inset), plotted against the maximum temperature gradient (axial and radial) as obtained from the profile experimental results.

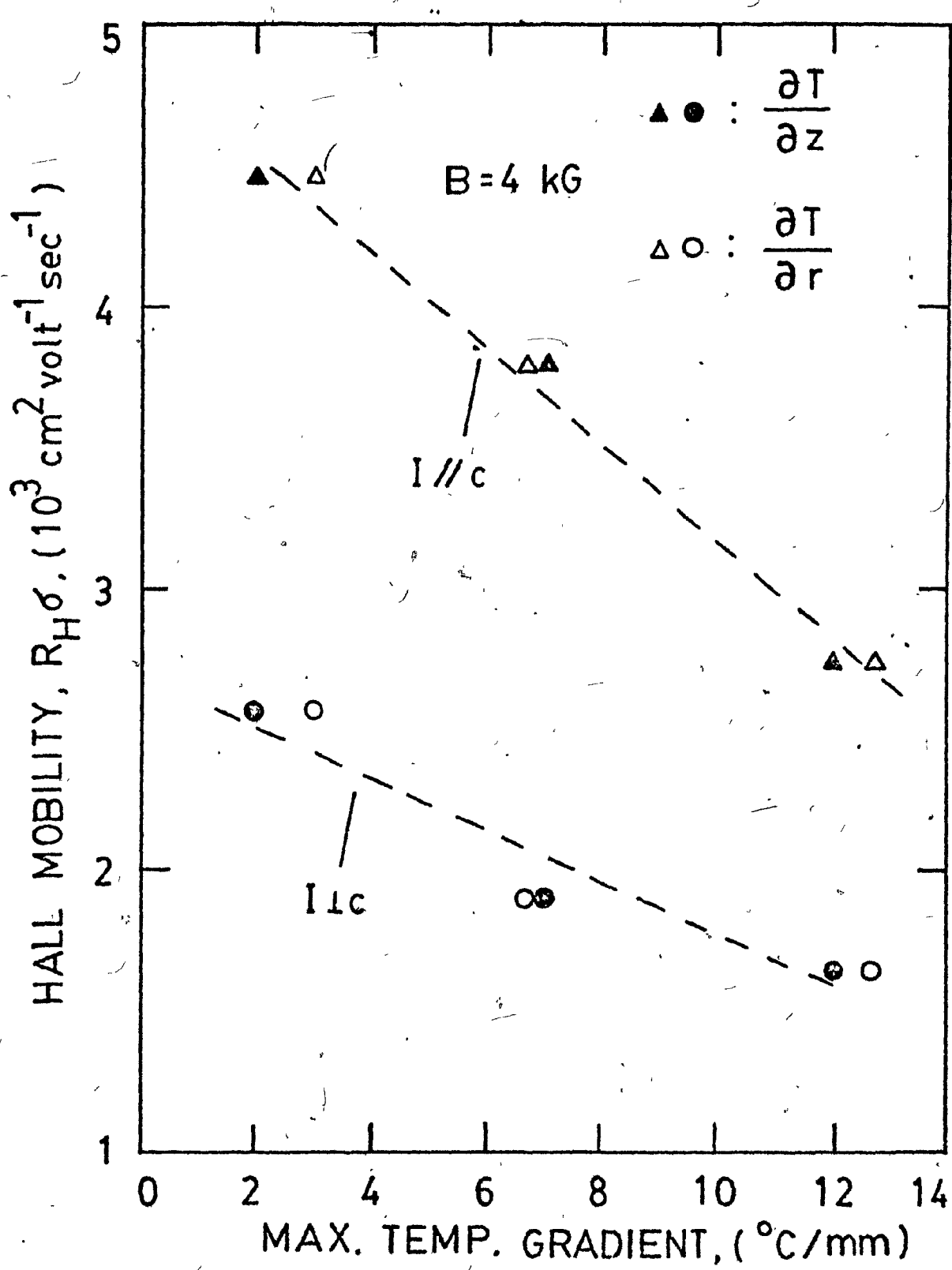


Fig. 4.10 Hall mobility product, RHO, measured on samples cut from the ingots shown in Fig. 4.8 (positions shown in inset to Fig. 4.9), plotted against maximum temperature gradient, as obtained from the profile experimental results.

 \odot

î.

C

CHAPTER 5 CRYSTALLINE GROWTH OF SexTe1-x ALLOYS

(-)

J. 1.

5.1 Introduction

As described earlier in chapter 2, the most successful attempts at crystal growth from the melt of $Se_{x}Te_{1-x}$ alloys have been by the Bridgman method. However, with the success of obtaining monocrystals of pure tellurium routinely by the Czochralski method, it was wondered if the same technique of avoiding thermal shock in the seed would be successful to grow $Se_{x}Te_{1-x}$ crystals. Accordingly, growth attempts were made by the Czochralski method using the slowest pull rates possible ° and the results are described in this chapter. As will be seen, the growth of Se-Te alloys is much more difficult than that of, tellurium and monocrystals were only obtained at the ends of the composition range, that is for the .Te-rich and Se-rich alloys. For intermediate compositions, crystalline samples were needed for the photoconductivity measurements to be presented in chapters 7 and 8, a slow used. These samples, while cooling method was monocrystalline, showed an appreciable degree of crystalline alignment.

The chapter begins with constitutional supercooling considerations to demonstrate the need for slow growth. Next the Czochralski results and the slow cooling results are

presented. Finally the evidence for monocrystallinity and composition of the alloys is given.

5.2 Limiting Growth Rate Considerations

When growth proceeds from a melt with a solute having a distribution coefficient less than unity, the dopant is rejected into the melt at the solid-liquid interface. This will result in a liquid layer containing a higher dopant concentration near the interface and cause the freezing point to be lowered in this region. The variation of the freezing point with distance into the melt, therefore, will not be linear but will have the shape shown in Fig. 5.1. If the temperature gradient is small (such as line l in Fig. 5.1), then there is a region, shown shaded, where the liquid is supercooled and in which spontaneous random crystallization can take place, resulting in polycrystallinity. This is known as constitutional supercooling. If, however, the temperature gradient is large enough, such as line 2 in Fig. 5.1, then the effect can be avoided. This can be shown to apply if [5.1],

$$\frac{\mathbf{v_G}}{\mathbf{G}} < \frac{\mathbf{D_{\ell}}}{\mathbf{m}(\mathbf{C_g-C_{\ell}})}, \qquad (5.1)$$

where G is the temperature gradient at the solid-liquid interface, v_G is the growth rate, D_{ℓ} is the diffusivity of the

solute in the melt, C_S and C_ℓ are the solute concentrations in the solid and liquid respectively, and m is the slope of the liquidus line at C_ℓ . Thus, from inequality (5.1), the growth rate v_G should be low and the temperature gradient G should be large for single crystal growth.

44. 3

The phase diagram of the selenium-tellurium system was reported by Lanyon and Hockings [5.2] to consist of simple liquidus and solidus curves as shown in Fig. 5.2. Using the data (C_{ℓ} , C_{s} and m) given in the phase diagram and further assuming $G=20^{\circ}/cm$ and $D_{\ell}=2x10^{-6}cm^{2}/sec$, Keezer, Griffiths and Vernon [2.14] calculated the limiting growth rate $v_{G,max}$ given by inequality (5.1). The variation of $v_{G,max}$ is shown by the solid line in Fig. 5.3, where the large increases in magnitude near pure Se and pure Te are due to reductions in $C_{a}-C_{\ell}$.

It is thus evident from Fig. 5.3 that very low growth rates down to about 0.1 mm/hr are required for monocrystalline growth of the Se-Te alloys. While such rates are somewhat below the capability of the usual Czochralski apparatus, the present growth experiments were undertaken because the limiting curve in Fig. 5.3 was based only on estimated data. For instance, if the estimated diffusion coefficient were larger, the limiting growth velocity would also be larger. In any case, the predicted supercooling does not necessarily

completely rule out monocrystalline growth.

5.3 Growth Procedures

The growth experiments in this study were carried out in the Czochralski puller used for pure tellurium but modified for very low pull rates by the use of an additional step-down gear box. The heating was obtained from rf induction either directly into the melt or into the metal crucible base. Additional heat was provided from the strip heater wound around the growth chamber, as shown schematically in Fig. 1.1.

Weighed amounts of tellurium and selenium (nominal purity 6-9's and 5-9's respectively) for the alloys were introduced into a silica crucible. After melting within the Czochralski chamber, the mixture was maintained at a temperature of about 50°C above the melting point and stirred to ensure homogeneity of the liquid by the rotation of an off-axis rod of 3 mm diameter turning at about 60 rpm. During the pulling, a rotating seed of pure Te was used for the Te-rich alloys and a second one for the Se-rich alloys. The rotation and vertical pull rates were often changed from run

to run.

5.4 Te-rich Alloys

All the growth runs for the Te-rich alloys were carried with pulling in the c-direction. Ingots from melts containing up to 8 at. Se were obtained without special difficulty using a vertical pull rate of about 5 mm/hr. However, with a pull rate of 10 mm/hr, an ingot(not shown) from a 5 at. 8 Se melt, showed a depression on one of its prism faces and striations on all of them. For growth runs from melts with more than 8 at. 8 Se it was found that the meniscus between the liquid surface and the seed would often break, that is, as the seed was slowly raised after immersion, the short liquid column would become thinner and then collapse, preventing the formation of an ingot. However, with special care and patience, ingots were obtained from melts containing up to 16 at. % Se. With melts containing larger concentrations, repeated attempts showed that it was impossible to obtain an ingot.

The cause of this breaking away of the meniscus would appear to be as follows. From the phase diagram (Fig. 5.2), it is clear that at a given temperature, there will be a higher concentration of Se in the liquid immediately adjacent to the freezing interface than in the bulk of the melt; this excess

selenium alloy will tend to remain at this location because its diffusion is slow and because it has a smaller density than the bulk melt and thus will float. Accordingly, the liquid alloy close to the seed will have a lower freezing point than the rest of the melt. Thus, when the temperature has been adjusted to be slightly above the melting point of the bulk melt, it will be well above that of the liquid within the meniscus, so that the solid-liquid interface rises (see Fig. 5.4). As the seed is moved upwards, the interface also rises. Eventually, however, the weight of the liquid column exceeds the surface tension and contact with the melt is lost.

(i

It was hoped that the addition of thallium, by lowering viscosity, would help to increase the diffusion of the excess selenium away from the interface. Accordingly, two runs, one with 1% and the other with 0.01% Tl in a 10 at.% Se melt, were made but the problem was not alleviated. Table 5.1 gives the growth parameters of the ingots grown. It is to be noted that ingot CZ-86, obtained from a 16 at.% Se melt, was grown at the rate of 0.4 mm/hr. A photograph of this ingot is shown in Fig. 5.5.

5.5 Se-rich Alloys

At the Se-rich end of the composition range sufficient rf induction heating currents are not induced in the melt, as

they are in the case of Te-rich alloys, because of the high resistivity of the material. However, a stainless steel base under the crucible served as a susceptor from which heat was passed to the liquid alloy. Keezer, Griffiths and Vernon [2.14] indicated that in Se-rich alloys the limiting crystal growth rate is controlled by viscosity rather constitutional supercooling. Therefore their technique lower viscosity by adding 1 at. thallium to the Se-Te melts was also used in this work. Except for one run, all ingots were grown from the (1010) plane of a tellurium seed; that is the growth direction was perpendicular to the c-axis. With a pull rate of 0,3 mm/hr, it was possible to grow ingots from Se-rich melts containing 0 to 10 at.% Te. Growth parameters are given in Table 5.2. Fig. 5.6 shows a photograph of selenium ingot pulled from a 100% Se melt. Attempts were also made to grow crystals from melts containing 13 and 15 at.% Te but these were unsuccessful due to the meniscus separation effect observed for the Te-rich melts. The scum problem [2.10] was found to be more severe for reported earlier Se-rich melts than for Te-rich alloys, perhaps due to the lower purity of the selenium. Furthermore, to obtain an ingot with a tellurium content greater than 2 %, it was necessary to allow a large region of the lower part of the "melt" solidify, so that the liquid floating on top just under the seed, had the right temperature for controlled growth.

(4

A run was also made from a 100 at.% Se melt (plus 1 at.% Tl) with the tellurium seed c-axis vertical. The result was an ingot with many small oriented grains, thus corroborating the conclusions of Keezer, Wood and Moody [2.20] that growth parallel to the [0001] direction is unfavorable.

5.6 Crystallization by Slow Cooling Method

As mentioned earlier, crystalline samples of Se_XTe_{1-X} were needed at many concentrations for photoconductivity measurements. However, since it was not possible to grow monocrystals from melts with compositions in the range 16 to 90 at.% Se by the Czochralski method, another method was tried. In this method the alloy concerned was simply melted in a quartz crucible and cooled slowly to room temperature over a period of about one week by slowly reducing the rf power of the induction heater. It was found that this resulted in regions of solidified material where appreciable crystalline alignment had taken place. These were cut out for visual inspection. Fig. 5.7 shows such a piece obtained from a 50 % Se melt.

5.7 Laue Patterns and Compositional Analysis

5.7.1 Laue patterns

The degree of monocrystallinity was assessed from Laue back reflection patterns taken at several points obtained by lateral displacement of the ingot. Fig. 5.8 shows the Laue pattern from a grown (1010) surface of the ingot prepared from the 16 at. % Se melt, while Fig. 5.9 shows the pattern from a (1120) plane of the ingot from the 90 at. % Se melt (95 at. % Se in the solid). In both cases, there is some mosaic structure are essentially monocrystalline. the ingots polycrystallinity was found in the 16 at. % Se melt alloy but only at a region where the ingot diameter was rapidly expanded. Fig. 5.10 is a pattern for the (1120) plane of an ingot grown from a 100 at. & Se melt (+1% Tl). In this case, the clear round spots are evidence for an excellent single apparent mosaic structure. crystal with no orientation of the Se crystal follows that of the seed was confirmed from Laue patterns taken on seed and crystal (not shown).

Laue back reflection patterns were also taken from the samples selected from the slowly cooled materials. The results generally showed less spots compared with those from the Czochralski grown ingots. Fig. 5.11 shows the pattern from a cleaved surface of a sample selected from the 50% Se material.

It is well known that a tellurium crystal can easily be cleaved along the (1010) surfaces. Preliminary experiments

also showed that the same planes cleaved for the Se-rich ingots. However, unlike tellurium crystals, which have mirror-like cleaved surfaces, the Se-rich ingots were found to have corrugated surfaces after attempted cleavage, consisting of needle-like material parallel to the c-axis of the ingots, as shown in Fig. 5.12.

5.7.2 Compositional analysis

Samples cleaved from the Se-rich ingots and samples cut (by chemical means) from the Te-rich ingots were then polished using Al₂O₃ powder for compositional analysis. The composition of the frozen melts and ingots was determined by X-ray fluorescence from a 20 µm electron beam analyser operating at 15 kV. In addition, in the case of the Te-rich alloys, the compositions were also determined by chemical analysis. Results for the two methods are compared in Fig. 5.13, where the Se concentration in the ingots is plotted against the Se concentration in the corresponding melt. It is noted that good agreement exists between the determinations by the two This reinforces confidence in the electron probe method, which was used to obtain the compositions of all the other alloys. Fig. 5.13 also shows that the Se content in the solid is about half that in the liquid, which is roughly consistent with the phase diagram. It is noted in particular that the ingot pulled from the 16 at. 8 Se melt actually

contained an average of 9 at. 8 Se in the solid.

Electron probe analyses were also obtained series of points along straight lines on the ingots parallel and perpendicular to the growth directions. Data from the points along the c-direction for three of the Te-rich ingots in Fig. 5.14. It is evident that are shown concentration along the pull direction is quite uniform for melt compositions of 4 and 12 at. 8. However, for the 16 at. 8 Se alloy there is an increase of about 1 at. % Se per cm of ingot, which is presumably due to an increase of concentration in the melt, as expected from the phase diagram. Concentration profiles for three Se-rich alloy ingots are shown in Fig. 5.15, where the tellurium concentration is seen to be reasonably uniform. It is further to be noted that the Te concentration in the ingots is much less than in the corresponding melts. This would seem to be in contradiction to the phase diagram, which at the Se-rich end indicates that the Te concentration should be much larger in the solid than in the liquid. However, it must be recalled that during the ingot growth it was necessary to have the larger part of the "melt" actually frozen, thus depleting the remaining liquid of its Te-content.

The compositions of the slowly cooled samples were also determined by electron probe analysis (see Table 5.3). Fig.

5.16 shows the actual selenium content in the selected samples plotted against the selenium concentration in the original melts. It is seen that these two quantities are roughly equal over the whole compositional range.

5.8 Discussion and Conclusions

In the present work, using pull rates down to 0.3 mm/hr, monocrystals were obtained by the Czochralski method for compositions containing 0 to 10 at.% Se in the solid at the Te-rich end and 95 to 100 at.% Se in the solid at the Se-rich end of the range. This is a slight advance over the corresponding values of 0 to 5 at.% and 100 at.% Se obtained by Keezer and co-workers. The present results thus tend to confirm that Se_XTe_{1-X} can be grown by the Czochralski method if the pulling rate is slow enough, coupled with sufficient temperature stability. For concentrations in the 50 % region, growth rates of the order of a millimeter per day would probably be required.

At the Se-rich end, high viscosity limits the growth velocity. However, at the Te-rich end, the limitation in the present work was not exactly constitutional supercooling but the related meniscus separation problem. Like constitutional supercooling, this arises from a build-up of interfacial selenium whose alloy has a lower freezing point than the rest

of the melt. However, rather than polycrystallinity, this leads to a rupture of the meniscus. While a steeper temperature gradient along the seed and pull-rod would help to keep the meniscus length short, the larger temperature drop would amount almost to thermal shock in the seed, which is known to be deleterious to monocrystalline growth [2.12].

Hence, except at the ends of the composition range it is more difficult to grow monocrystals of $\mathrm{Se_xTe_{1-x}}$ alloys by the Czochralski method than the Bridgman method. In the latter, the solid is below and the liquid is on top, so that excess selenium rejected at the interface tends to float upwards, because of its lower density, away from the critical growth region.

During the present studies several alloy samples were prepared by the slow cooling method consisting of simply allowing Se_xTe_{1-x} melts to freeze slowly in a silica beaker over a period of about a week. The frozen mass, while not monocrystalline, contained regions which were well aligned crystallographically.

Table 5.1

Details of Growth Runs of Te-rich Se Te Ingots

	se Conc. in Melt (at%)	Dopant in Melt	Pull Rate (mm/hr)	· Rotation Rate		•
Ingot No.				Pull Rod (rpm)	cru- cible (rpm)	Remarks
		3	6	9	26	Hex. cross-sec., shiny surface
cz-80	4.0	Undoped		[∞] 8	15	Hex. cross-sec.
cz-81	8.0	Undoped		8	40	Hex. cross-sec., shiny surface
.` CZ-82 ·	10.0	Undoped	4		00	Hex. cross-sec., shiny surface
		T1 0.01%	4	12	20	
CZ-83	10.0		4	8	20	Depressions on 2 faces
CZ-84	10.0	T1 1.0%	•	8	16	Hex. cross-sec.
cz-85	12.0	Undoped	4			Rough surface with depressions
CZ-85	16.0	Undoped _	0.4	6	28	Wug

Table 5.2

Details of Growth Runs of Se-rich Se Te Ingots

	× ,			Rotation Rate			-		
Ingot No.	•	Te Conc. in Melt (at%)		Pull Rod (rpm)	Cru- cible (rpm)	٨	Remarks		
CZ-90		0		3	10 7	· · · · · · · · · · · · · · · · · · ·	1 4		
CZ-91		0		5	9		•		
CZ-92		3 %		6	. 10	•			
CZ-93		5	1	6	7	/	Oval Cross-sec., Monocrystalline		
CZ-94.	ţ	8 ,-		` 6	11	,	•		
CZ-95		10		5	7		a ·		

Notes:

- 1. Pull rate is 0.3 mm/hr.
- 2. Melts contain 1 at. % Tl.

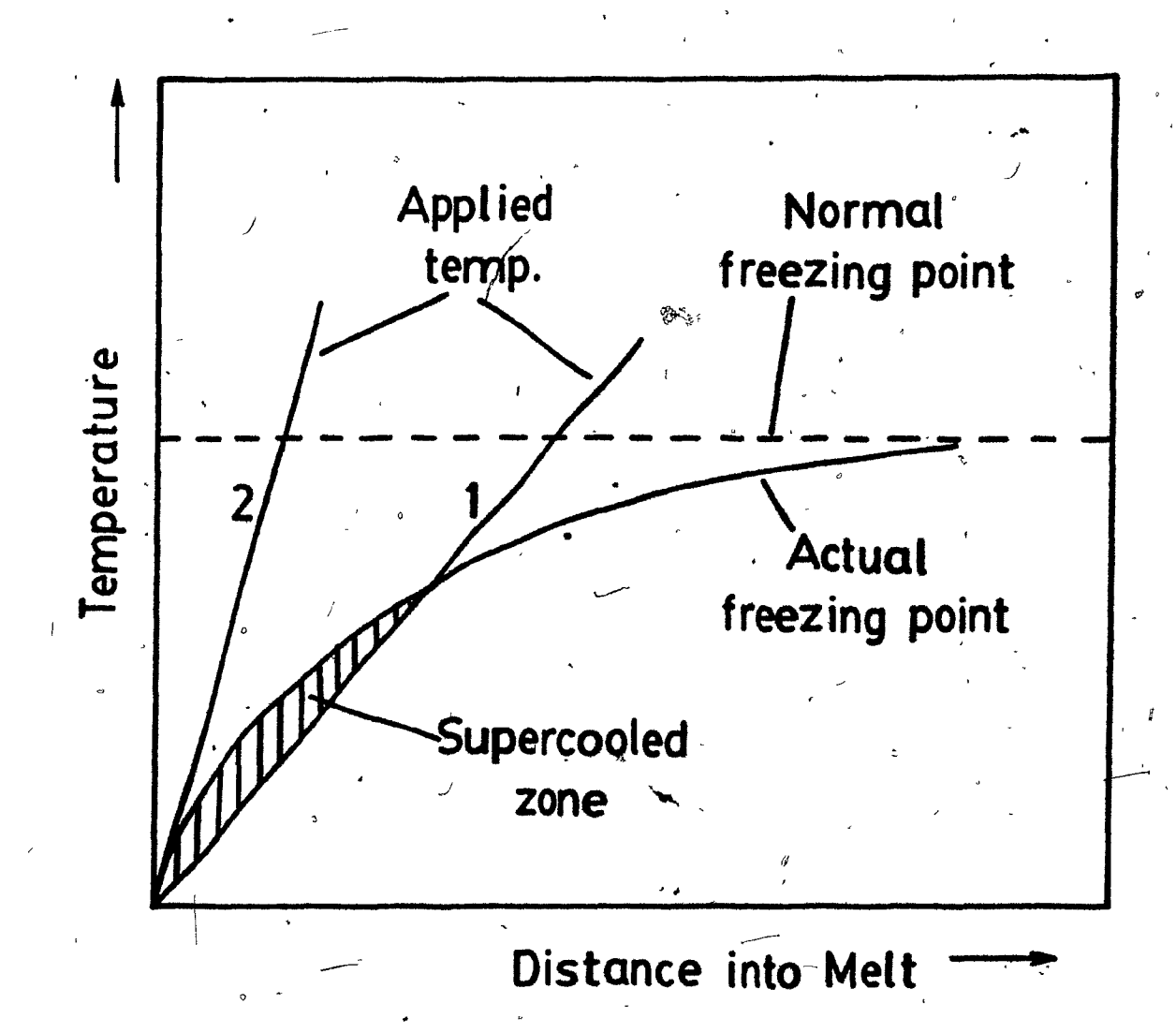
Table 5.3

Se-Te Alloy Slow Cooling Runs

	Run* No.	Se Conc. in Melt	Se Conc. in the Selected Sample	Nominal** Melting Point	
		(at.%)	(at.%)	(_o c)	' ,
•	SC-1	10	8	419	
	SC-2	20	. 18	392	
	SC-3	30	23	365	0
	SC-4	40	28	342	
	SC-5	50	45	319	- *
	SC-6	60	54	294	
	SC-7	70	58	~ 271	~~
•	SC-8	[*] 80	75	248	
	SC-9	90	86	231	(

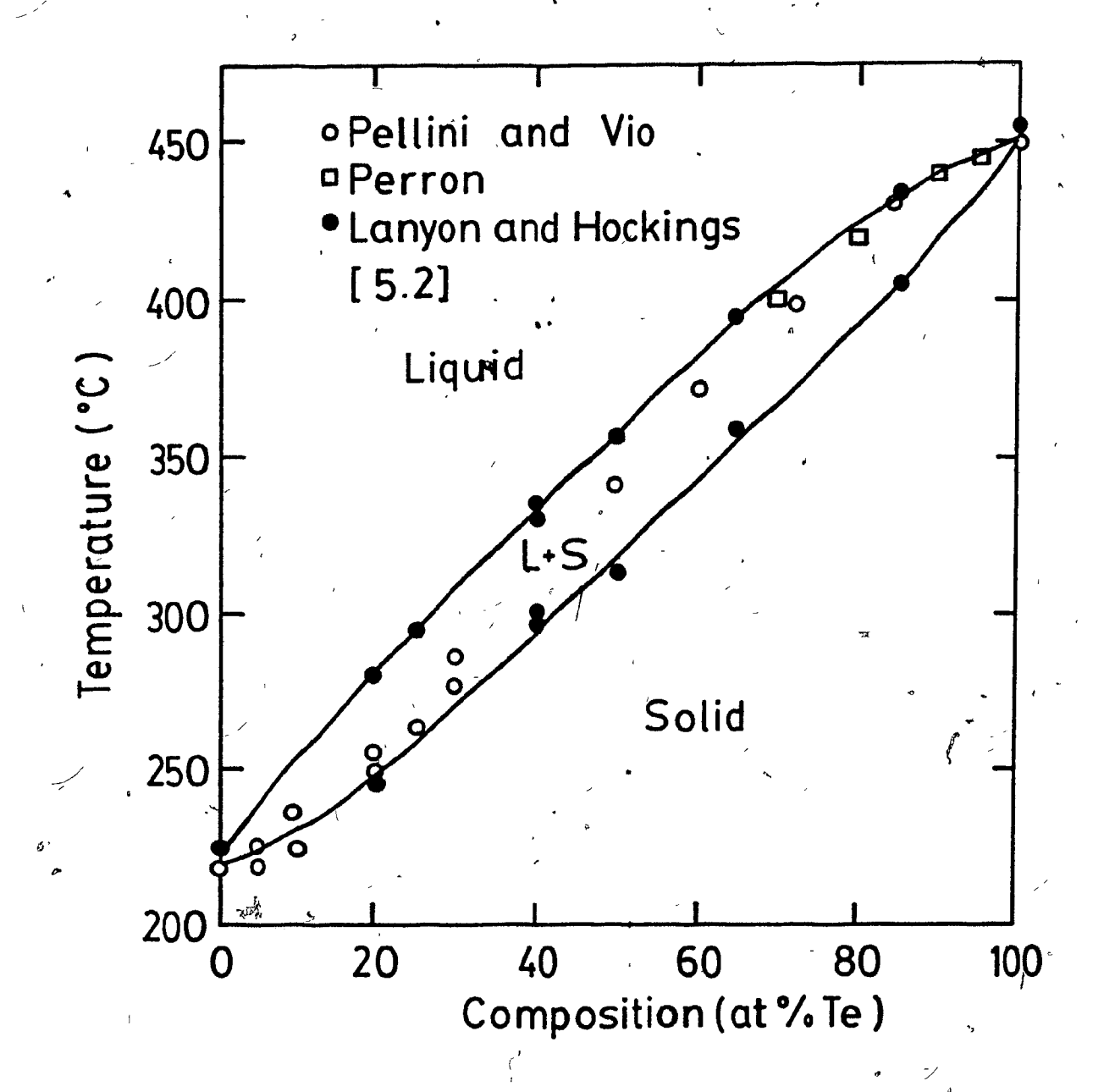
^{*} Cooling time about 160 hrs.

^{**} Ref.[5.2].



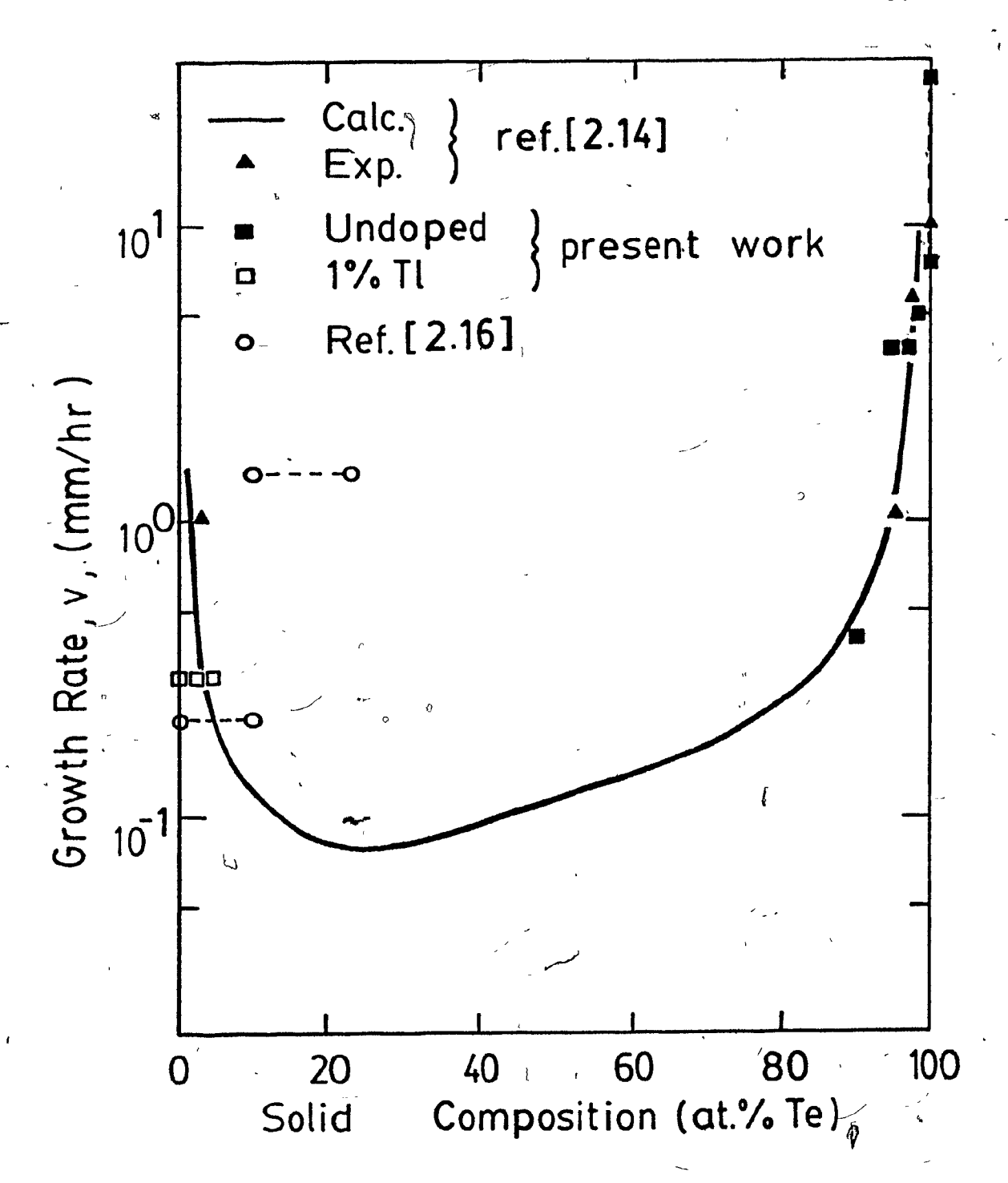
O

Fig. 5.1 Diagram showing the freezing point and the applied temperature in the melt at the solid-liquid interface.



(

Fig. 5.2 Tellurium-selenium phase diagram (taken from [5.2]).



(1

Fig. 5.3 Plot of limiting growth velocity against composition for single crystal growth, calculated from constitutional supercooling considerations (reference [2.14]). Shown also are experimental results using Czochralski and Bridgman methods.

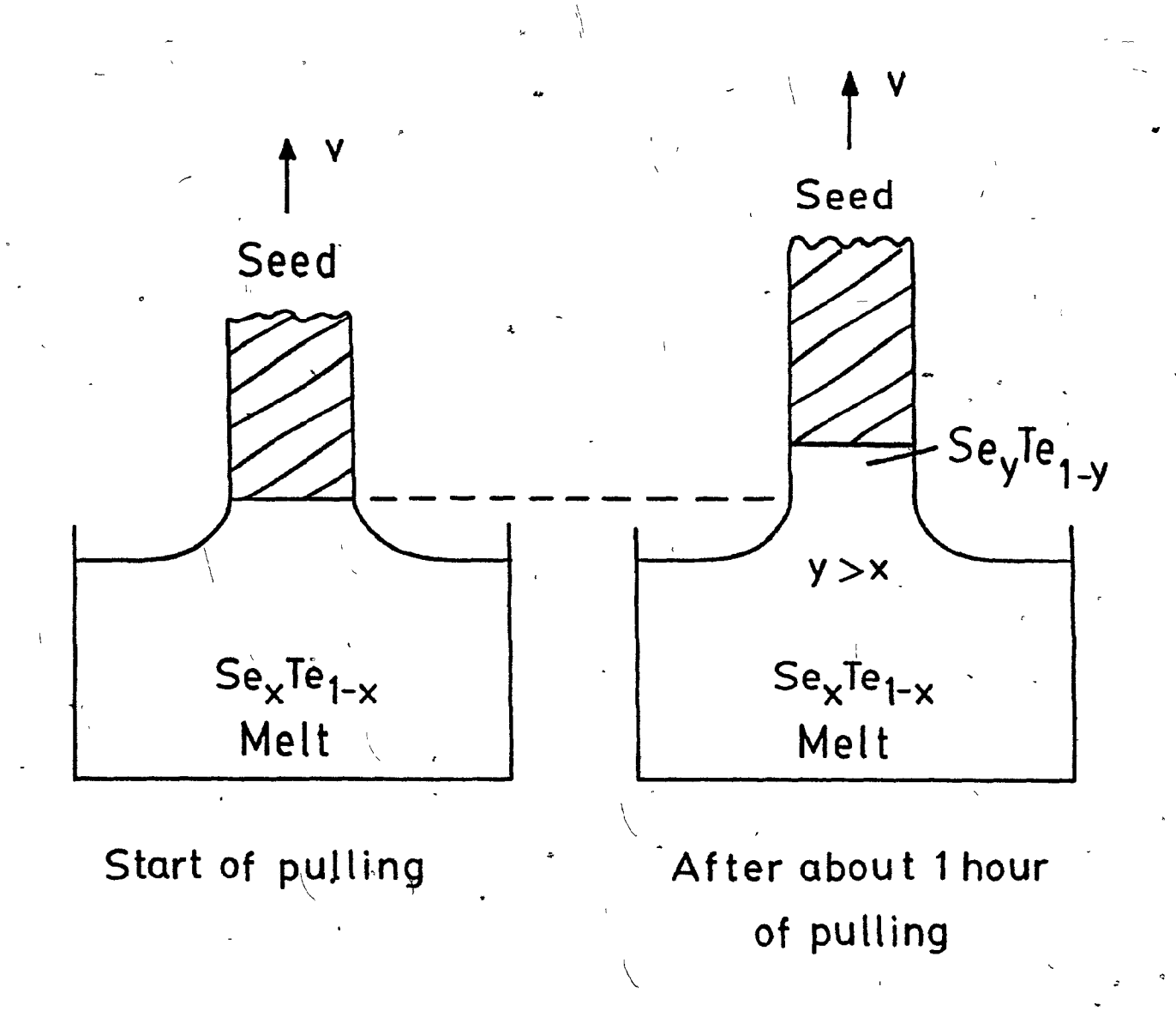
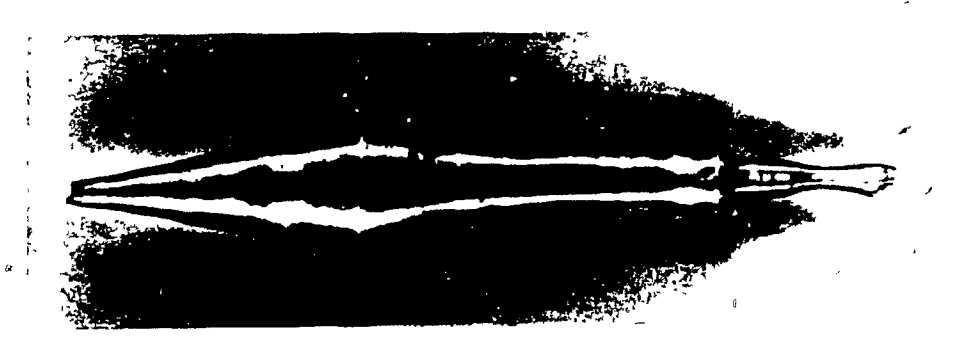


Fig. 5.4 Schematic diagram showing extension of the liquid column immediately below the seed tip during the crystal pulling. This effect arises from the build-up of Se-richer alloy near the freezing interface.



c-axis

1 cm_

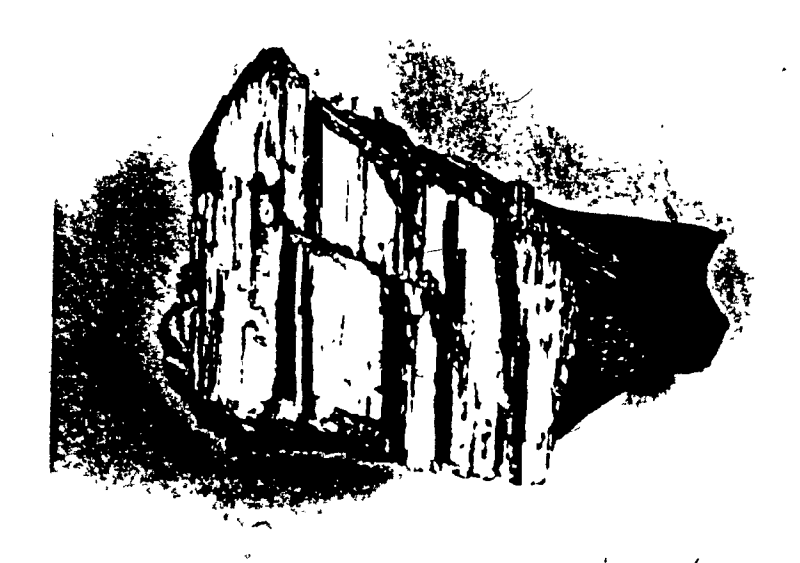
Fig. 5.5 A Se_{0.1}Te_{0.9} alloy (ingot number CZ-86) grown parallel to the c-axis from a melt containing 16 at.% Se.



1 cm,

Fig. 5.6 A selenium monocrystal (ingot number CZ-91) grown perpendicular to the c-axis from a melt containing 1 at.% T1.

9



1 cm

Fig. 5.7 Photograph showing a cleaved sample obtained from a slowly cooled melt containing 50 at. % Se.

~_

na – Irobiya () Kiliya karazal yang dalam Milika king alak.

the confidence of the state of the

ام و ا و ۱۸۰

्रा । सर्वे क्षण्डारीका

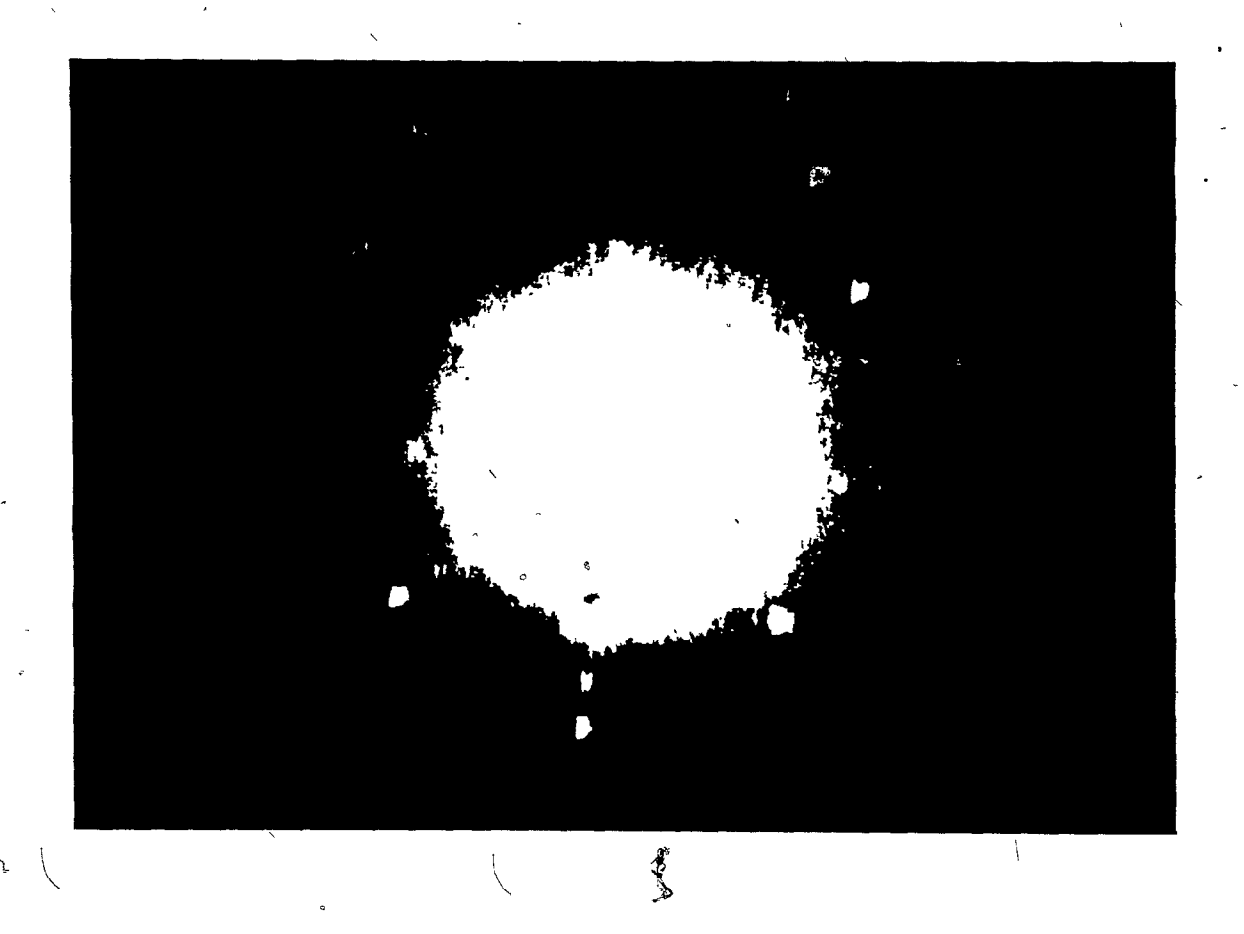


Fig. 5.8 Laue reflection pattern (from two regions separated by about 4 mm) of a (1010) plane of the Se_{0.1}Te_{0.9} ingot (number CZ-86).

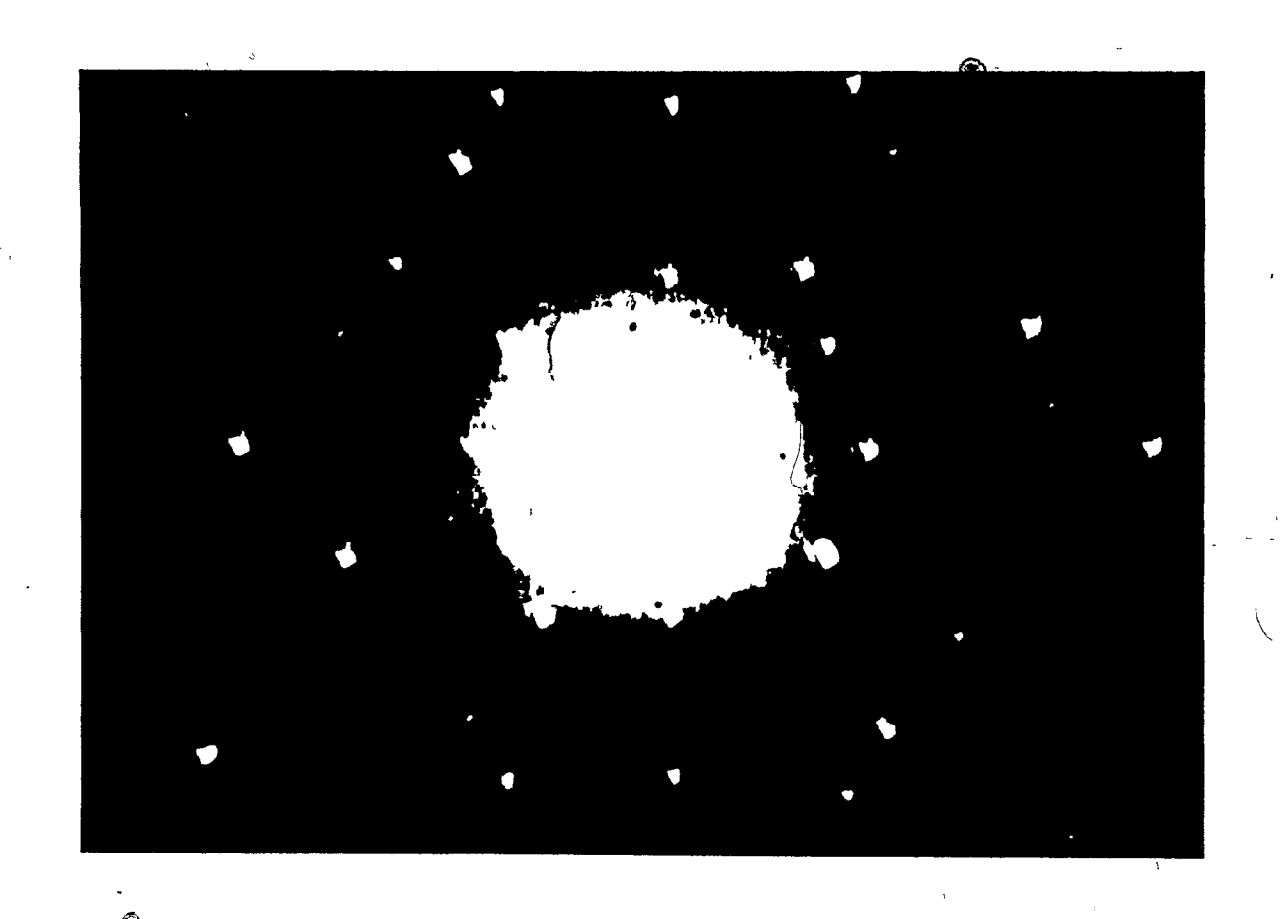


Fig. 5.9 Laue reflection pattern (from two regions about 4 mm apart) of a (1120) plane of the Se_{0.95}Te_{0.05} ingot (number CZ-95).

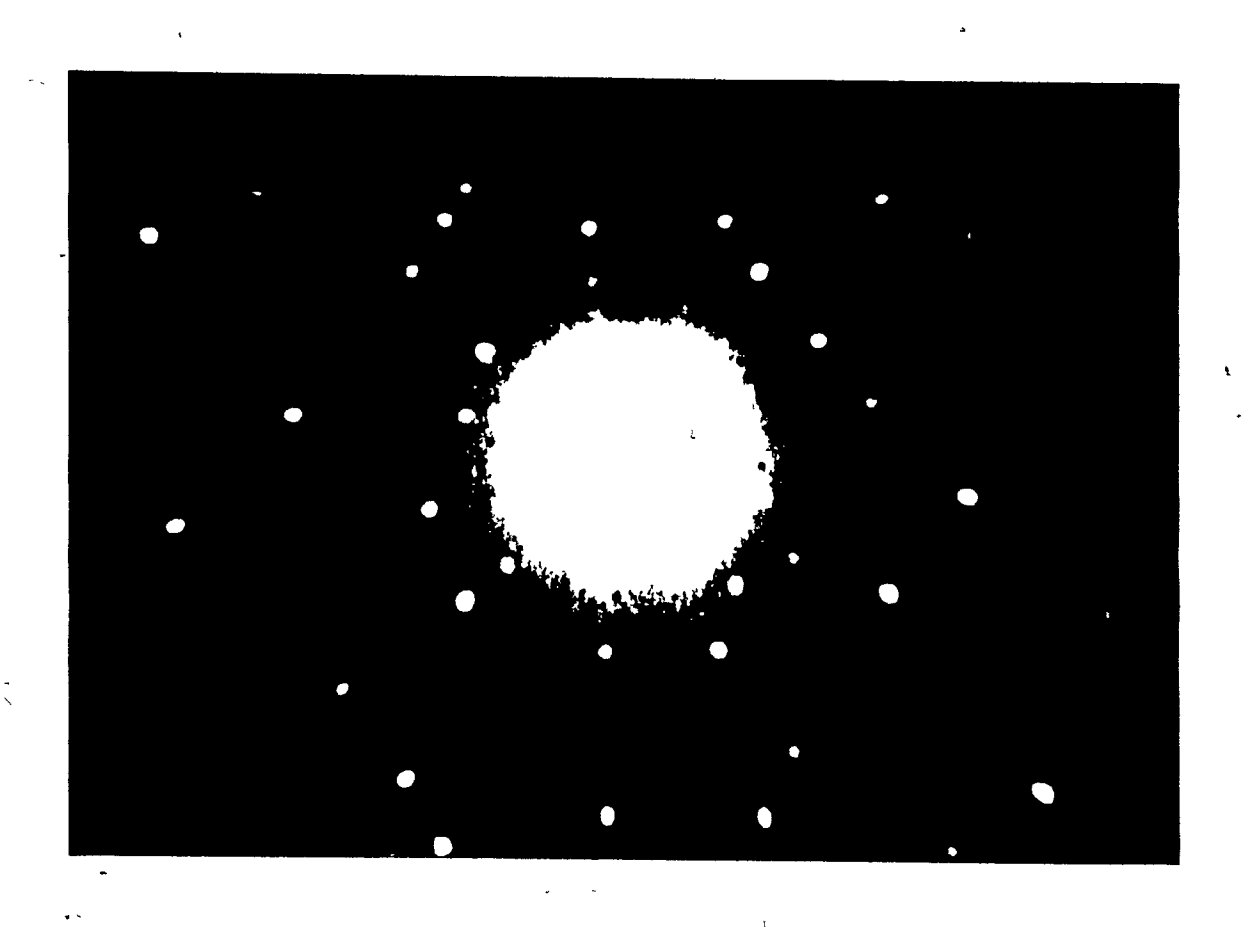


Fig. 5.10 Laue reflection pattern (from two regions about 4 mm apart) of a (1120) plane of the Se ingot (number CZ-91).

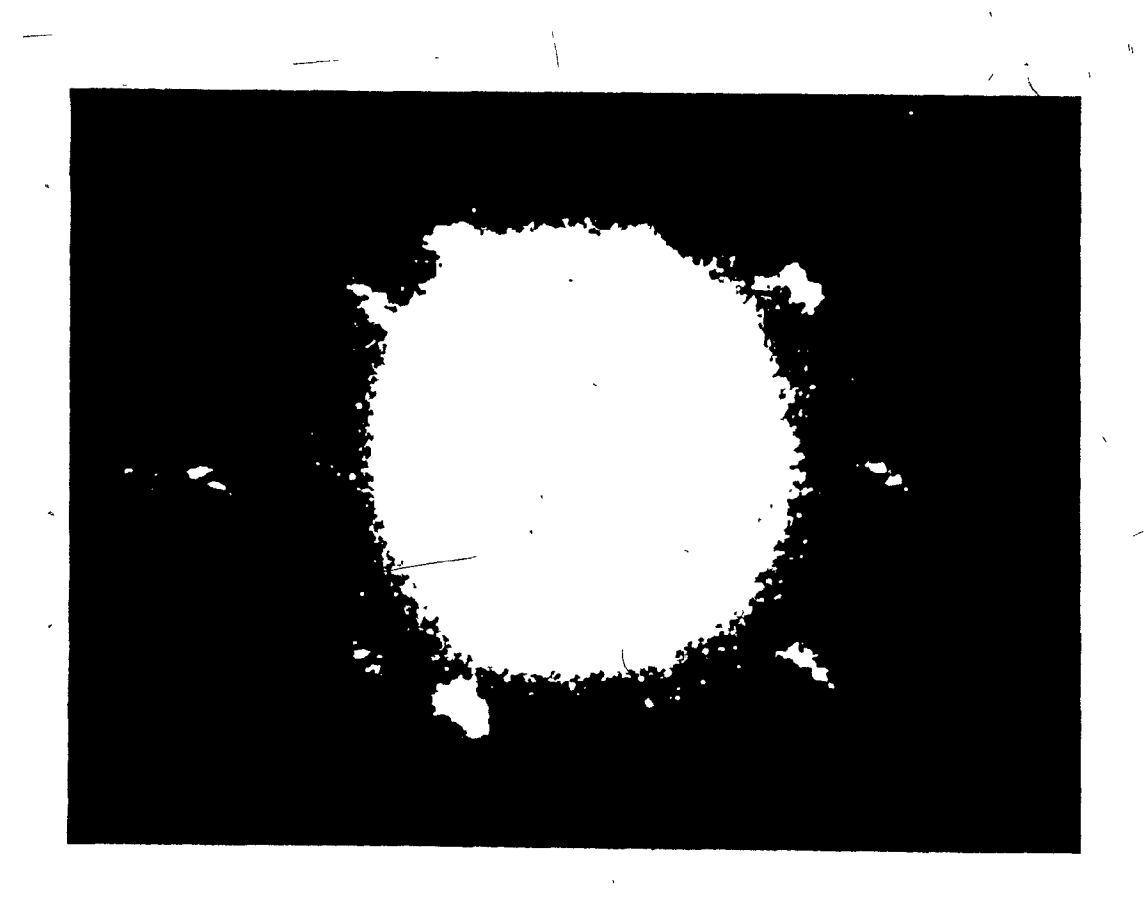
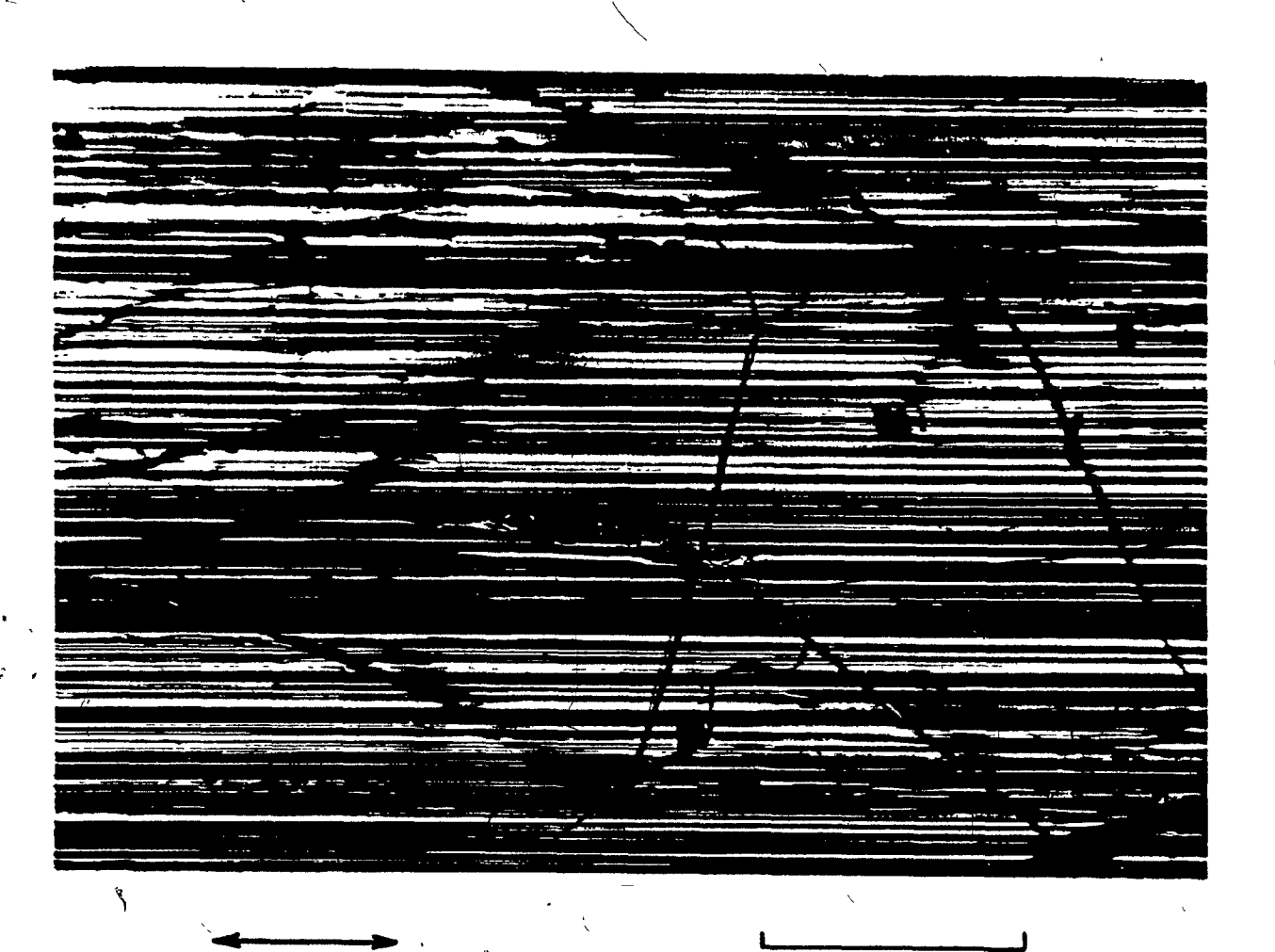


Fig. 5.11 Laue reflection pattern (from two regions about 4 mm apart) of a cleaved plane of a sample selected from slowly-cooled Se_{0.5}Te_{0.5} material.



c-axis

200 µm

Fig. 5.12 A photomicrograph of a cleaved (1010) plane of a Seq. 97Teq.03 ingot (number CZ-93), showing needle-like material parallel to the c-axis.

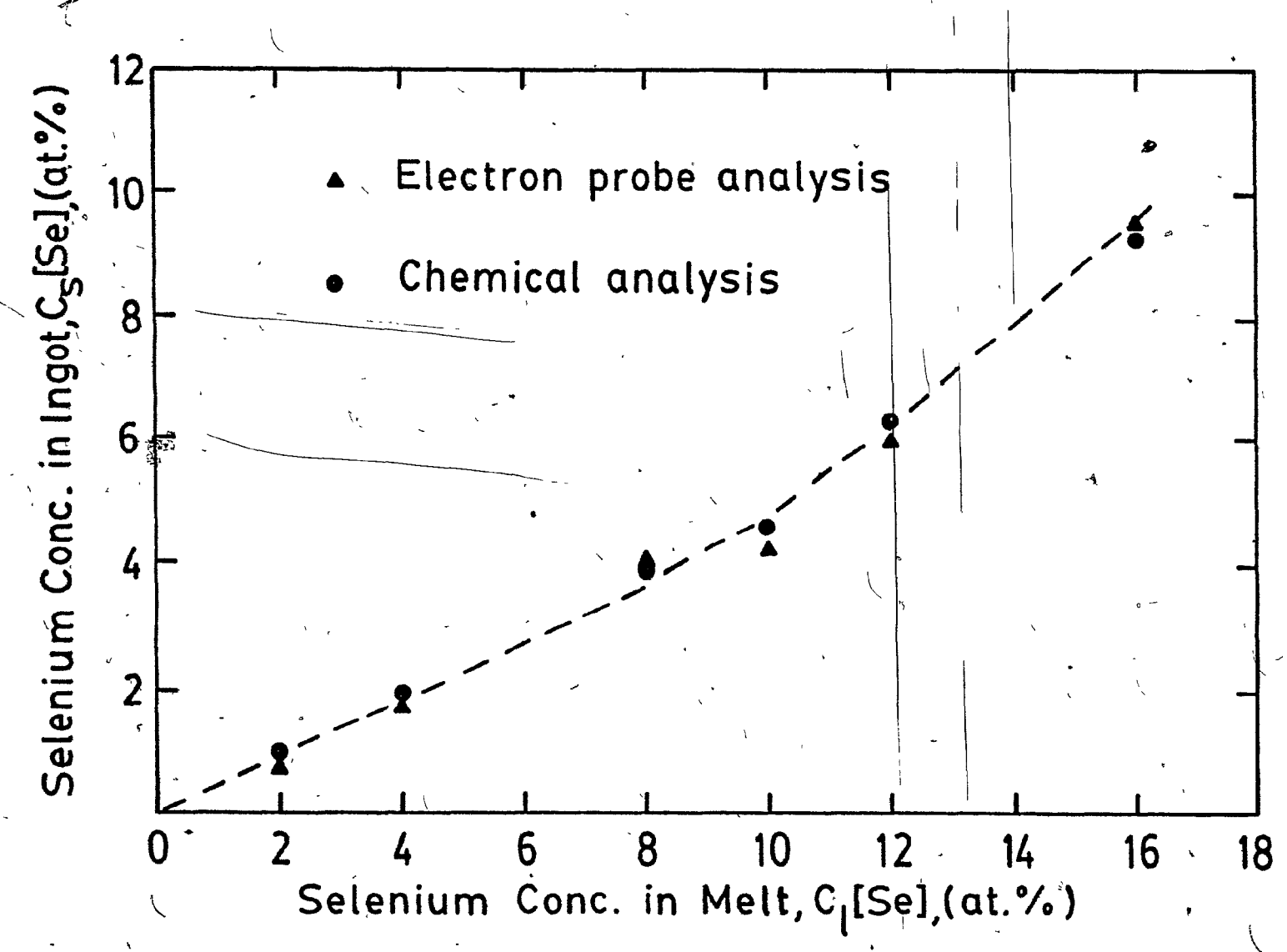


Fig. 5.13 Selenium concentration in ingots plotted against selenium concentration in the corresponding melts for the Te-rich alloys. The concentrations were determined by both electron probe and chemical analysis methods.

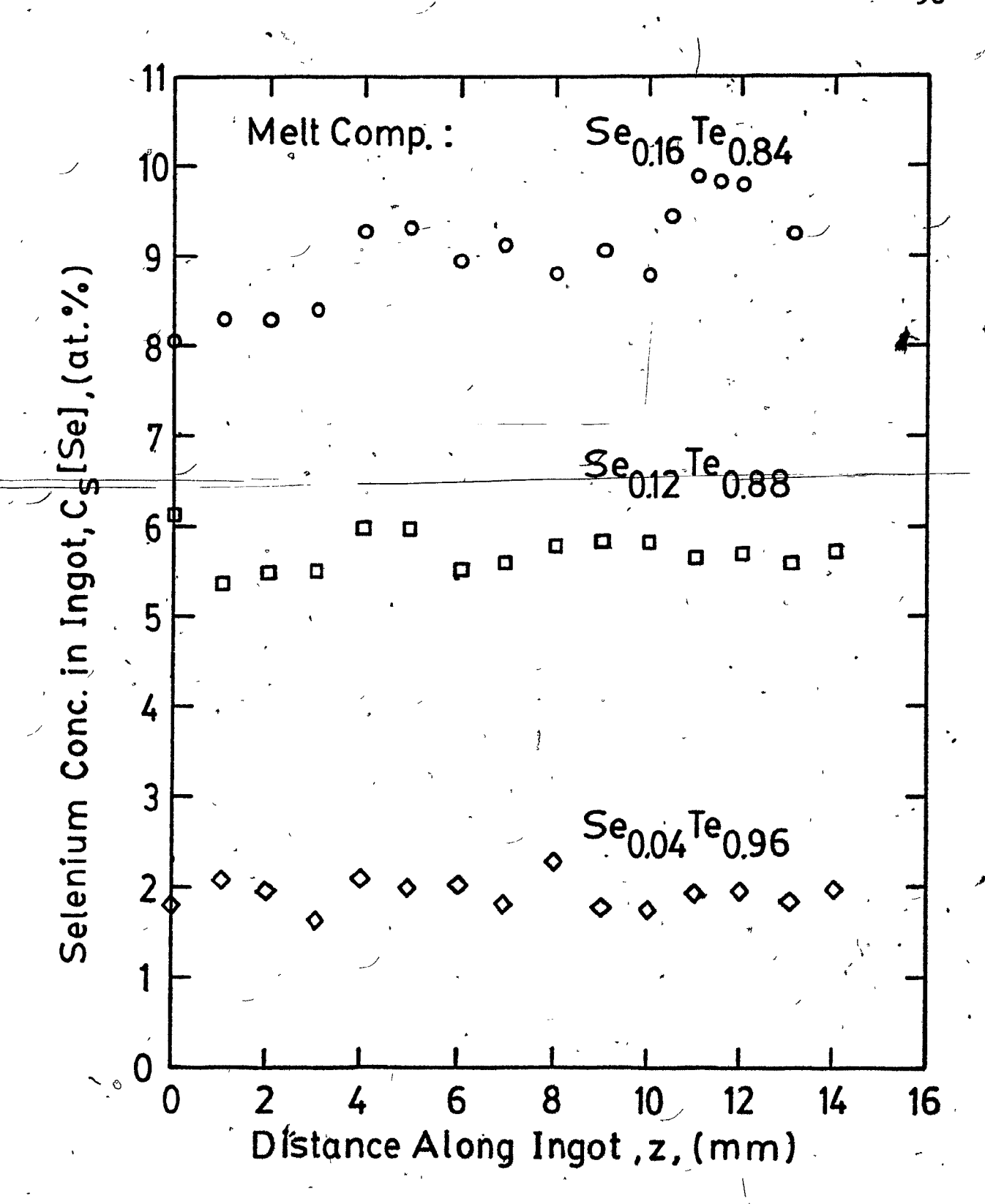


Fig. 5.14 Selenium concentration in the solid, determined by electron probe analysis, plotted against distance along the ingot for three of the melt compositions.

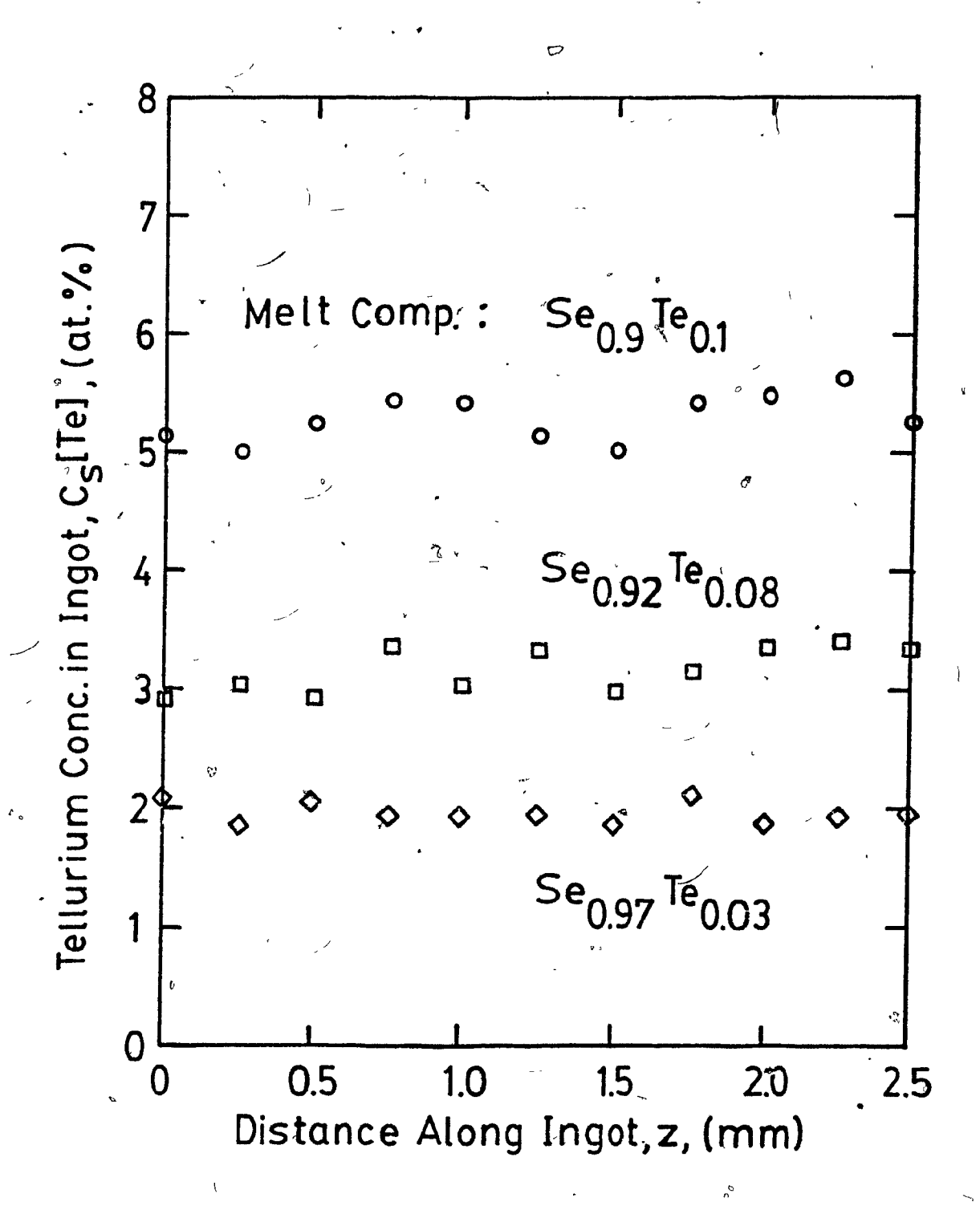


Fig. 5.15 Tellurium concentration in the solid, determined by electron probe analysis, plotted against distance along the ingot for three of the melt compositions.

. €

C

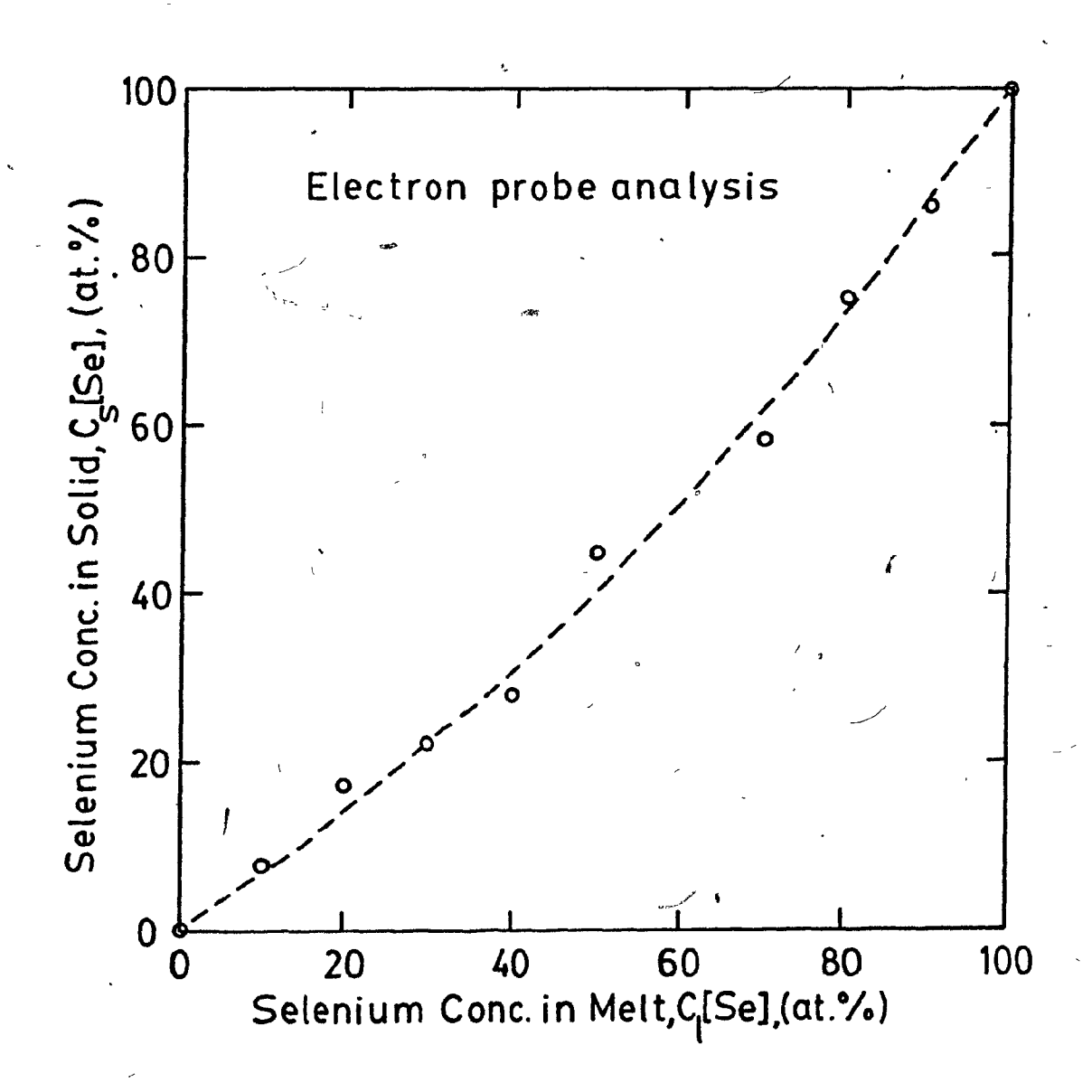


Fig. 5.16 Selenium concentration in the selected slowly cooled alloy samples plotted against selenium concentration in the corresponding melts.

CHAPTER 6 MEASUREMENT APPARATUS AND METHODS

6.1 Introduction

In the present work, the principal measurements made on Se Te tellurium alloys and photoconductivity as a function of wavelength and, to a lesser extent, as a function of temperature, and of time. measurements of the frequency response of photoconductivity and 'of noise voltage were also carried out on the pure tellurium samples. In this chapter the apparatus and methods to obtain these measurements are described, together with the procedure to prepare the samples for the measurements. While measurements were also made of Hall coefficient, electrical conductivity and magnetoresistance on some of the samples, the apparatus involved will not be described, since it is fairly standard, at least for low resistivity samples.

6.2 Sample Preparation

The method of normal sample preparation is now described. Special annealing and abrasive treatments were given to some of the tellurium samples but these will be described separately in chapter 7.

6.2.1 Czochralski-grown Te and Te-rich alloys

For Czochralski-grown tellurium and Te-rich alloys the samples for photoconductivity measurements were chemically cut initially as wafers from the ingots with a string saw using a solution consisting of HCl:CrO₃:H₂O in the ratio 1:2:4 by weight. The wafers were then mounted on aluminum blocks and chemically polished successively on two parallel (1010) faces using a solution of composition HNO₃:CrO₃:H₂O in the ratio 1:2:4 by weight. The final dimensions were about 8 mm in length (parallel to c-direction), 2 mm in width (parallel to the [1120] direction), with thicknesses from 0.15 to 2.2 mm for the tellurium samples and about 1.5 mm for the Te-rich alloy samples. Orientation of the samples is shown in Fig. 6.1.

Three side-probes for potential measurements were attached to each sample (see Fig. 6.2) by melting in 0.002 inch diameter platinum wires. The two ends of each sample were coated with a solder of composition 50%Sn, 47%Bi and 3%Sb*(by weight). A fine copper wire was attached to one end of the sample and the other end was soldered to a brass plate, the central part of which was covered with an insulator blackened to minimize reflection. A thick rectangular paper window served to screen light away from the end contacts as indicated by the broken line in Fig. 6.2.

6.2.2 Czochralski-grown Se-rich and slow-cooled alloys

In the case of the $Se_x Te_{1-x}$ alloys which were grown either by slow cooling or, in the case of the Se-rich alloys, by the Czochralski pulling, the samples were prepared by cleavage from the bulk material, followed by abrasive polishing on all four lateral faces using 0.05 μ m diameter Al_2O_3 powder. Orientation of the samples was same as that for Te-rich case. While chemical cutting and polishing methods would have been preferable, such techniques are not yet developed for these compositions. The attachment of the measuring side probes and the mounting of the samples were the same as those for the Te-rich samples as described above.

6.3 Apparatus

6.3.1 Cryostat

A metal cryostat was designed and built to enable the photoconducitvity to be measured from liquid nitrogen temperature to room temperature. As shown in Fig. 6.3, it consists of a cylindrical stainless steel tank with a copper block (2.5x2.0x0.8 cm³) embedded in the lower portion. A feeder tube coming out of the tank is welded to a top plate. The tank is surrounded by a cylindrical brass jacket containing a circular aperture for the optical window. A window consisting of a disc of ZnS (Kodak IRTRAN 2) was used for the measurements between wavelengths of about 1 and 4.5 µm

and a disc of SiO, for wavelengths between 0.4 and 2.0 µm. The sample, mounted in its holder, was attached to the copper block, the temperature of which was measured iron-constantan thermocouple (TCl in Fig. 6.3). between the tank and the jacket was evacuated to a pressure about 10⁻³ Torr using a rotary and diffusion pump combination. The low pressure provided a sufficiently good thermal insulation to conserve the liquid nitrogen and also to prevent vapor condensation on the sample after cooling. The insulated copper wires used for current and voltage were long enough and cooled enough, by winding them around the tank, to minimize heat flow reaching the sample by conduction along them. obtain temperatures other than 77 K, the sample was mounted on a second copper block (B3) which was attached to a thin metal piece (the other end fixed to the bottom block B2 in Fig. 6.3). A copper wire was connected between the copper block (B3) and the top plate to supply heat to the sample block. By suitable choice of the dimensions of the copper wire and the thin metal piece, a stable temperature could be obtained between 77 and 300 K.

6.3.2 Optical system

(a) Monochromator

The monochromatic radiation required for the

measurements was obtained, from a Perkin Elmer model 13 spectrophotometer. Fig. 6.4 shows a schematic diagram of the optical arrangement of the instrument, which consists essentially of a Nernst glower light source, a 13 hertz light chopper, a prism monochromator and a vacuum thermocouple detector unit. For the measurements between wavelengths of 1 and 5.5 μ m an NaCl prism was used and for the range 0.4 to 2 μ m an SiO₂ prism was employed. By rotating the prism, the different wavelengths λ were obtained at the exit slit (S1), whose width controlled the bandwidth $\lambda\lambda$. The light energy from the spectrophotometer was measured by the vacuum thermocouple (Reeder & Co., Inc.) which had a KBr window. Its output was fed to a 13 hertz amplifier and thence to a chart recorder.

(b) External optics and detector calibration

The light from the exit aperture of the monochromator was allowed to fall on a concave mirror (M1) of radius 10 cm which focused the radiation on to the sample as indicated schematically in Fig. 6.4. For polarization of the radiation, a wire grid polarizer (Molectron Corp., model / IGP25) was positioned between the concave mirror and the sample.

The relationship between the energy of light falling on the sample and the output reading of the vacuum thermocouple was determined with a photovoltaic InSb detector (Judson

With constant slit width of 0.2 mm, $\Delta\lambda$ = 0.008 to 0.14 μm as λ changes from 0.6 to 6 μm .

Infrared Inc.) calibrated between 1 and 5.5 μm . This detector had the same window material (IRTRAN 2) as the cryostat when used in this wavelength range. For the wavelength range between 0.4 and 1.1 μm , the calibration was done with a silicon detector (Photo Research model 301). Allowance was made for the transmission of the quartz window used in this case.

(c) Electrical measuring circuit

The sample was supplied with steady current from a battery pack having a voltage up to 500 volts in series with a resistor of up to 100 megohms. The measuring circuit used is shown in Fig. 6.5. For the samples with small and medium concentrations of selenium the alternating potential arising from the chopped incident radiation on the sample was measured by connecting the two adjacent side probes to a lock-in amplifier (Princeton Applied Research model 124A), using its internal reference frequency. The dark steady voltage between the side probes was measured using an electrometer.

For the Se-rich samples, where the resistance was very high (about 10 megohms), both the alternating and the steady state potentials were measured with an electrometer (Keithley Instruments model 610C) having an input impedance of about 14 ohms.

Suppose $R_{\rm O}$ and R are respectively the dark and illuminated resistance of that portion of the sample not covered by the mask, and $R_{\rm S}$ is the resistance of the series resistor (plus that of the covered part of the sample and that of the two contacts). The relative change of conductivity resulting from illumination is then given by,

$$\frac{\Delta \sigma}{\sigma_{o}} = \frac{v_{o}^{-v}}{v} \frac{R_{s}^{+R}}{R_{s}} \frac{R_{o}}{R}$$

where v and v_0 are the potentials across the uncovered portion of the sample respectively during illumination and in darkness. Since for the low illumination levels used in the experiments $\Delta v/v_0$ was less than 0.1%, the relation can be written,

$$\frac{\Delta \sigma}{\sigma_{o}} = \left(1 + \frac{R_{o}}{R_{s}}\right) \frac{\Delta v}{v_{o}}$$

The highest sample resistance was that for selenium, having a value of about 10 megohms. The illuminated part corresponded to about a third of the sample length making $R_0 = 3$ megohms. Thus with a series resistance of R = 100 megohms, we have,

$$\frac{\Delta \sigma}{\sigma_{\rm O}} = \left(1 + \frac{3}{100}\right) \frac{\Delta v}{v_{\rm O}} = 1.03 \frac{\Delta v}{v_{\rm O}}$$

Since the 3% difference is less than the experimental error, no correction was made. Therefore, for all samples it was assumed that a constant current was present during the readings.

(d) Pulsed source

For photoconductive decay measurements, the sample was illuminated with a pulse of white light. In initial work, this was obtained from the monochromator using chopped white light from the Nernst source. Later, the source was changed to a General Electric Strobotac with a pulse duration of 10 µsec, or a spark source (Xenon nanopulser model N-789B) having a 20 nanosec pulse duration. The repetition rate for the two units was set to about 2 pulses/sec.

6.4 Measurement Method

6.4.1 Steady state photoconductivity

Liquid nitrogen was first slowly introduced into the cryostat so that the sample was cooled to 77 K over a period of about 50 minutes. Faster cooling introduces imperfections into the sample. A constant air current was directed on to the optical window to minimize possible vapor condensation due to cooling.

The current for the Nernst glower was then increased to preset value and the slit width was adjusted to give sufficient ~ light through the monochromator photoconductivity detection and at the same time narrow enough to obtain, a small bandwidth $\Delta\lambda$ for resolution. The monochromator was then set at a given wavelength. current flowing through the sample, the 13 hertz alternating voltage between the side probes Δv was measured using the lock-in detector in the case of the Te-rich alloys. The vacuum thermocouple voltage was also recorded at this wavelength. The measurement was then repeated at another wavelength until the whole range was covered. The steady voltage between the side probes was also noted.

In the case of the samples having intermediate compositions, the chopping of the light was done at 2 hertz because of the longer time constants involved. The intensity of incident radiation was monitored by recording the vacuum thermocouple voltage at each wavelength. For the Se-rich samples, where the time constants were very long, the monochromatic radiation beam was periodically interrupted manually over periods of up to ten minutes. Because of the output voltage from the thermocouple was low in the wavelength range below 1 µm, the radiation intensity was measured by using the same silicon detector for calibration described in

section 6.3.2.

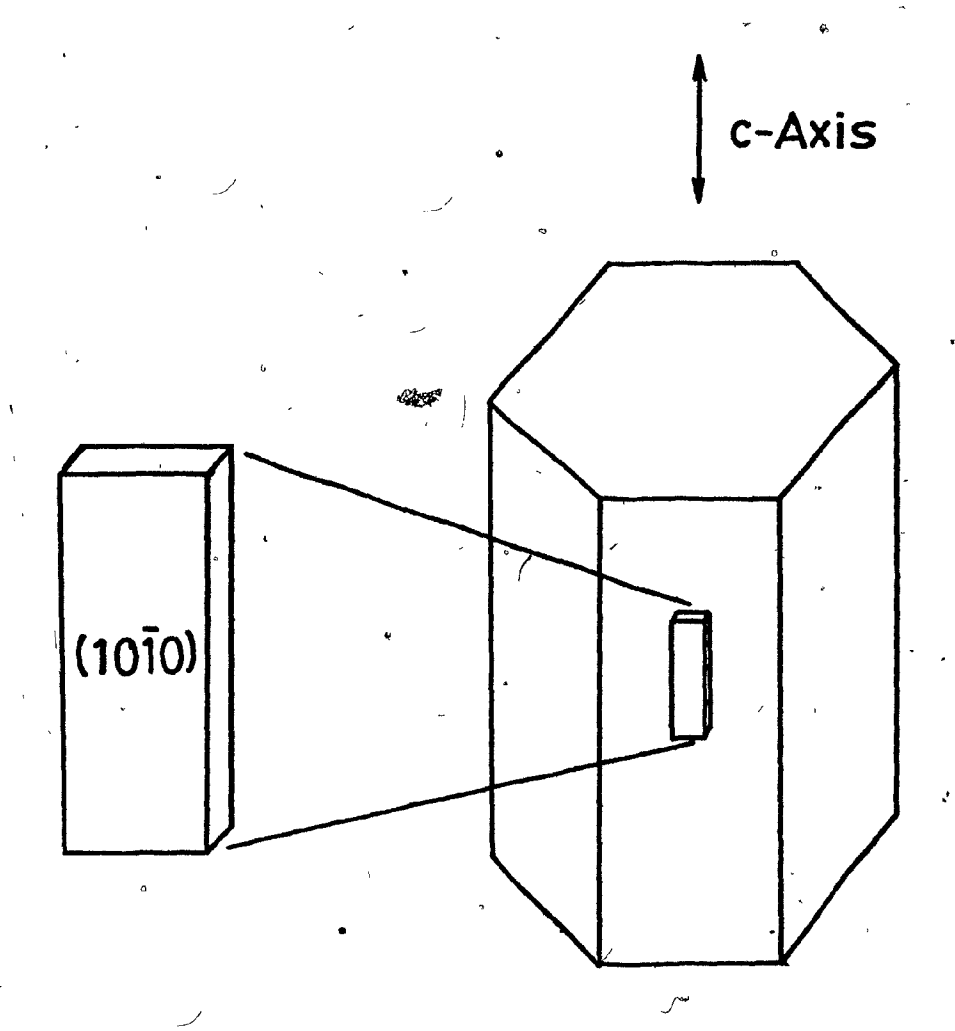
6.4.2 Transient decay

The photoconductive decay following illumination of the sample pulsed light was measured þу oscillographically the voltage between the side \probes (see Fig. 6.6). However, in the case of the Se-rich alloys, the slower photoconductive decay was measured with an X-Y recorder connected to the output from the electrometer. The constant of the measuring circuits was estimated to be less than 1% of that for the sample itself. It may be noted that while the spark source of the nanopulser was more intense than the chopped light from the Nernst source, the largest change of conductivity $(\Delta \sigma/\sigma)$ for the tellurium sample was still less than 0.001.

6.4.3 Frequency dependence and noise measurements

In the case of the tellurium samples, photoconductivity at a fixed wavelength was measured as a function of chopping frequency from 13 to about 1000Hz. The chopping was done using a rotating disc chopper (Princeton Applied Research model 125A). In this case, the different frequencies were obtained by changing the chopper disc.

The average noise voltage was also measured in tellurium as a function of frequency of detection. This was done by measuring the average of the random voltages appearing at the sample probes using the lock-in amplifier set at the different frequencies. The noise voltage was determined in the dark with and without current through the sample.



C

(3)

Fig. 6.1 View showing the crystallographic orientation of the sample.

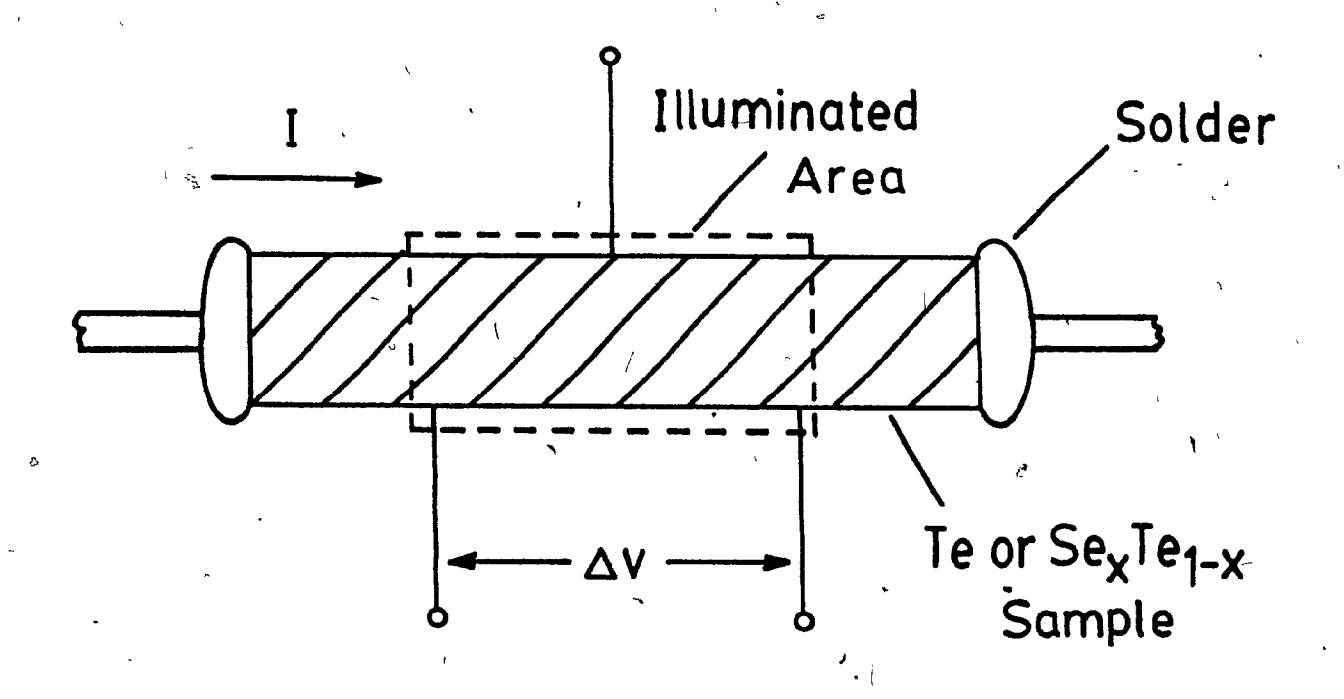
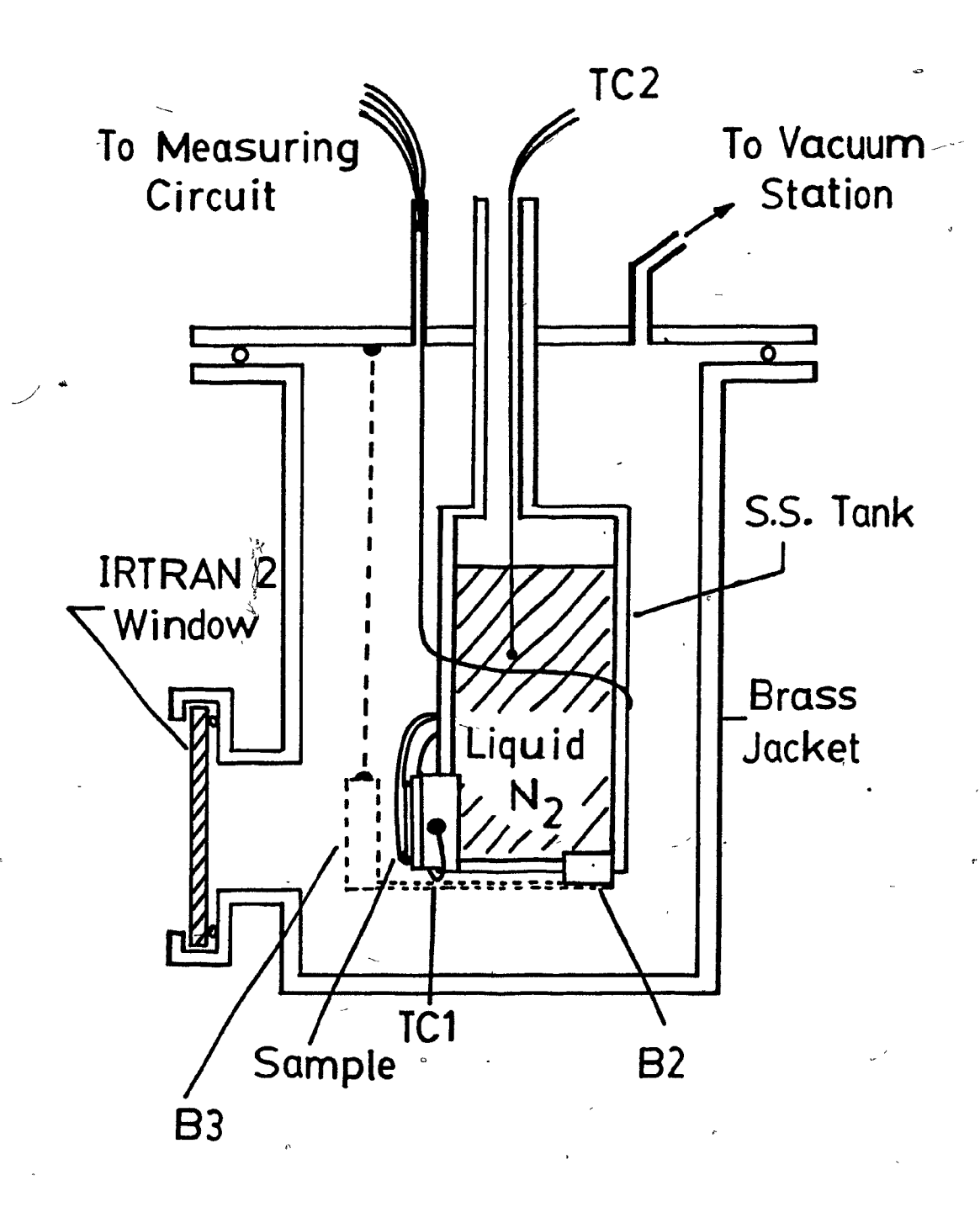


Fig. 6.2 View of the sample with the current leads and the side probes for measurements.



(

Fig. 6.3 A cross-sectional view of the cryostat to cool the sample during photoconductivity measurements.

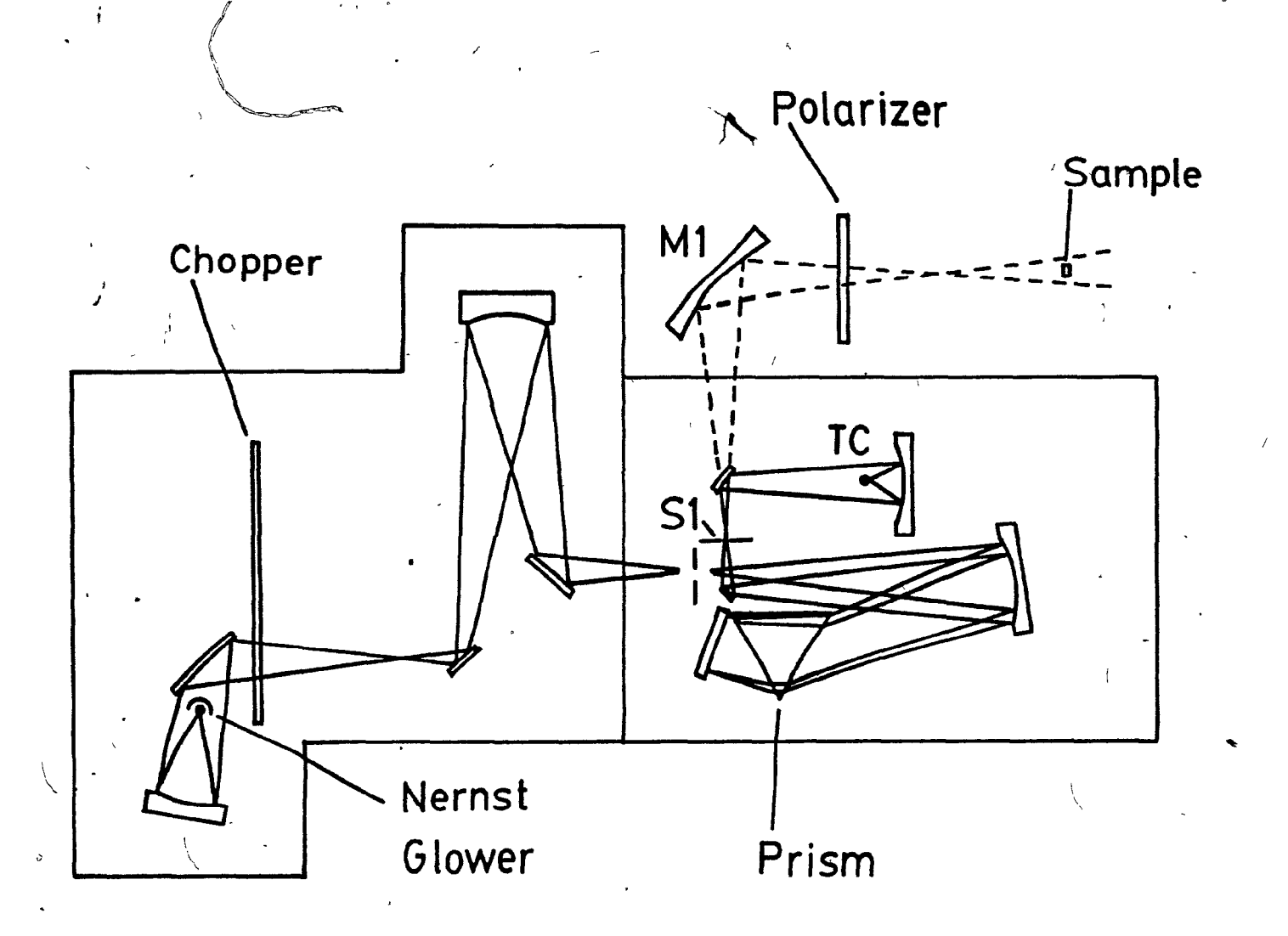


Fig. 6.4 Schematic diagram of the spectrophotometer and the external optics.

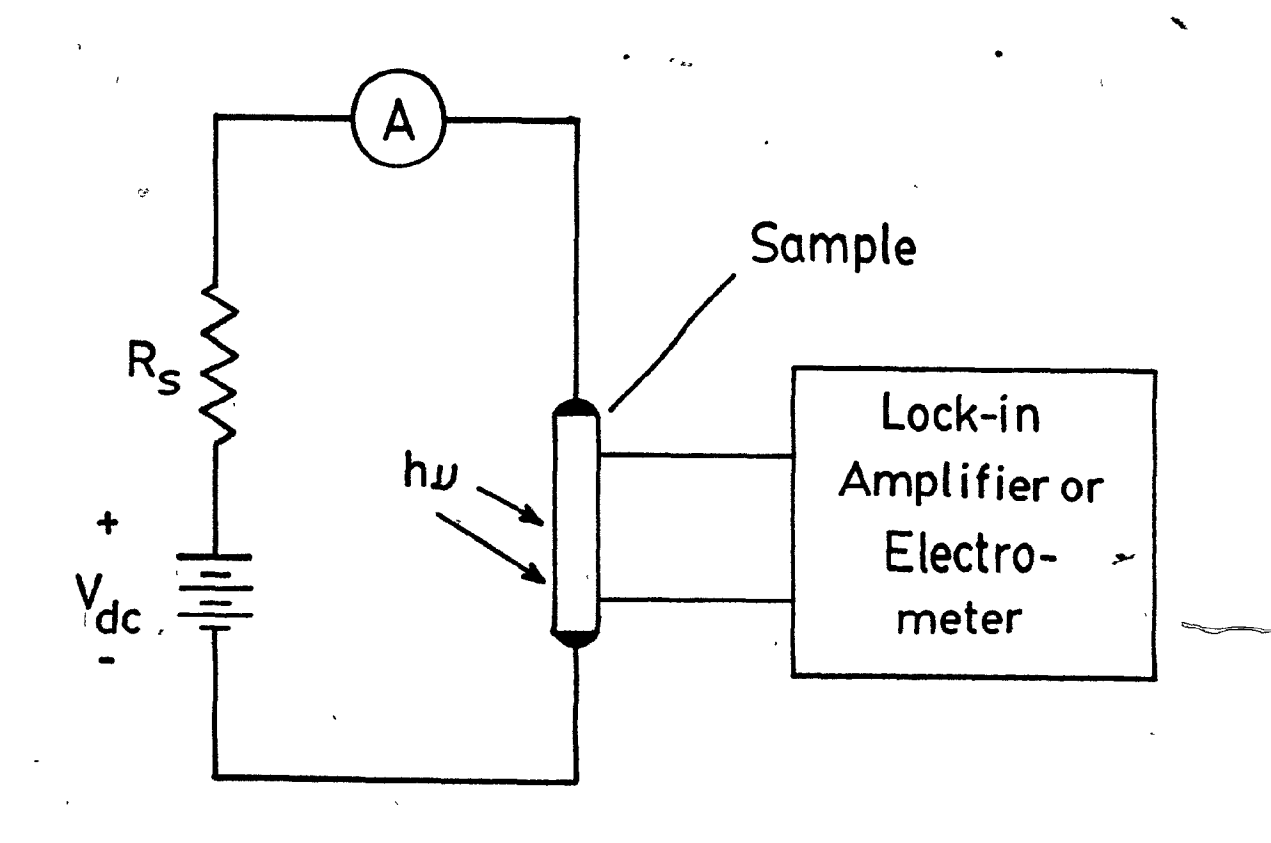


Fig. 6.5 Circuit for steady state photoconductivity measurements.

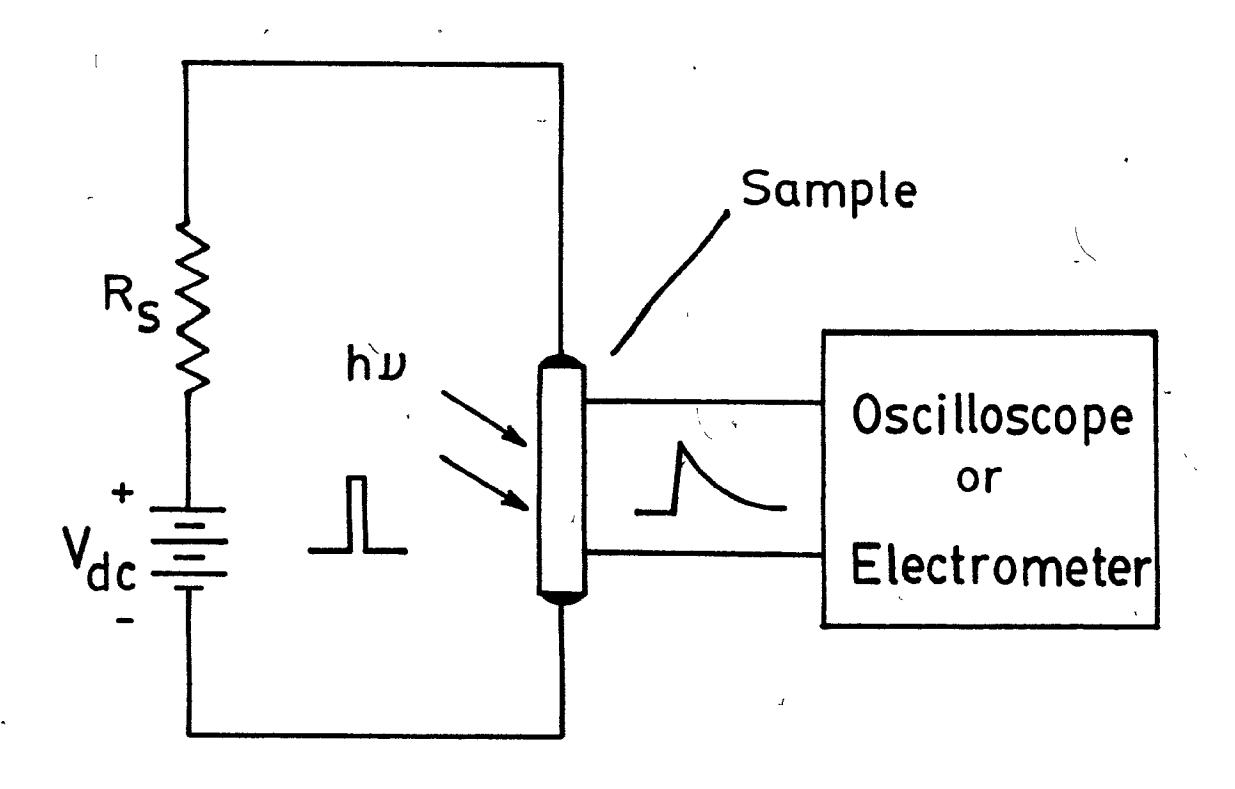


Fig. 6.6 Circuit for transient decay measurements.

CHAPTER 7 PHOTOCONDUCTIVITY RESULTS IN UNDOPED TELLURIUM

7.1 Introduction

The results of measurements made on undoped tellurium samples are presented in this chapter. They consist of photoconductivity as a function of wavelength from 1.4 to 4.4 µm at 77 K, as a function of temperature from 77 to about 200 K and as a function of frequency to 1 kHz. Results are also reported on transient photoconductivity at 77 K and on current noise in the samples. Of special interest is the effect on the results of sample treatment and of changes in the sample thickness.

In the section where the results of noise measurements are given, some estimates are also made of the photoconductive detectivity. This is done as a preliminary re-assessment of the potential of tellurium as a material for an infrared detector operating near 3.5 µm.

7.2 Special Sample Treatment

The results given in this chapter were obtained on 5 samples chemically cut from the same single crystal tellurium ingot (No. CZ-78-11). The dimensions are given in Table 7.1. After the normal chemical polishing described in chapter 6,

one of the samples (CZ-78-11-AB) was given an abrasive polish on the two (1010) surfaces using 0.05 µm Al₂O₃ powder on glass for 2 minutes. Two other samples (CZ-78-11-AN and 78-11-ANT) were annealed. This was done by placing a chemically cut slice in a quartz ampoule, pumping it out and back filling with argon at 300 Torr pressure and sealing off. The ampoule was then maintained at 395°C for 168 hours. After slow cooling to room temperature over a period of about 50 hours, the slice was taken out and the two samples were chemically cut from it and then chemically polished. Two more samples (CZ-78-11-11 and 11-T) were chemically cut and polished without further treatment.

7.3 Low Frequency (13 Hz) Photoconductivity Results

7.3.1 Variation with temperature

The spectral variation of $\Delta\sigma/(\sigma_{O}E_{q})$ with wavelength between about 1.4 and 4.4 μm , measured at three different temperatures for E/c and EIc, is shown in Fig. 7.1. Here $\Delta\sigma$ is the conductivity change due to illumination, σ_{O} is the dark conductivity and E_{q} is the photon flux incident on the sample. It is noted that with increase of temperature the photo-response decreases and for EIc the peak values shift towards shorter wavelength and the peak-to-"plateau" ratios decrease. The variation of $\Delta\sigma/(\sigma_{O}E_{q})$ at 3.5 μm over a wider

temperature range is shown in Fig. 7.2. The change near 77 K is seen to be relatively flat with a stronger decrease as the temperature is raised. The rapid decrease above about 180 K (ie. 1000/T=5.5) occurs in the intrinsic region, where the Hall coefficient has a negative sign. Within the extrinsic region (below 180 K) the photoconductivity changes by about an order of magnitude. The average photoconductive decay time τ , also plotted in Fig. 7.2, changes by a similar amount, suggesting that this quantity predominantly controls the temperature variation of photoconductivity.

The relative change of conductivity $\Delta\sigma/\sigma_{0}$ at 77K is plotted against irradiance E at a wavelength of 3.8 µm in Fig. 7.3. It is seen that up to an E value of 20 µW/cm² at least, the variation is linear. This is consistent with the results of Vis [2.25] according to whom nonlinearity only occurs above a $\Delta\sigma/\sigma_{0}$ value of about 0.01.

7.3.2 Effect of sample treatment and thickness

The spectral photoconductive response at 77 K of three samples of similar thickness is shown in Fig. 7.4 where each has had a different final preparational treatment; one was chemically polished, another annealed and then chemically polished and the third chemically polished and finally abrasively polished as described in section 7.2. It is noted

that the photoconductivity is much higher for the annealed sample and that the fall-off of photoconductivity with decreasing wavelength for the abrasively prepared sample is much stronger than the other two. At shorter wavelengths the difference between the curves for the abrasive and annealed samples amounts almost to two orders of magnitude.

The effect of annealing is also shown for the two thinner samples in Fig.7.5. Here the annealed sample 11-ANT has about three times the responsivity of the unannealed sample 11-T at all wavelengths.

The effect of sample thickness is evident from the results on the two non-annealed samples in Fig. 7.6. Here the photo-response for the thinner sample (0.20 mm) lies well above that of the thicker (1.16 mm) sample, except above 4 μ m wavelength where the curves cross. This is in accordance with theory as described in an earlier paper [7.1].

7.4 Transient and Frequency Response Results

7.4.1 Photoconductive decay

The form of the photoconductive decay at 77 K, following spark source excitation, is shown for one of the samples by the oscilloscope trace in the inset to Fig. 7.7.

Readings from this trace are shown as a semilogarithmic plot in the main part of the figure. The decay clearly does not correspond to a simple exponential but an approximate fit to the experimental results can be made with sum of two exponentials of the form $I_f \exp(-t/\tau_f) + I_s \exp(-t/\tau_s)$. The solid curve in Fig. 7.7 represents such a fit. Table 7.1 lists the parameters obtained by fitting the decay curves of four of the samples. It is noted that the fast decay time constant τ_f is about an order of magnitude smaller than the slower time constant τ_s and that generally I_f is greater than I_s .

During one of the decay measurements, the sample was also illuminated with unchopped white background light, which reduced I_s but left I_f essentially unaffected. This suggests that τ_s may arise from trapping. Vis [2.25] reported that the decay time decreased with increase of background light presumably because of the decreased contribution of τ_s . The effect of annealing on the decay characteristic is not entirely clear but for the thin samples, Table 7.1 shows that both decay times τ_f and τ_s were increased by the thermal treatment.

7.4.2 Frequency response

The variation of the normalized photoresponse with

chopping frequency measured on the two thin samples is shown in Fig. 7.8. The signal is seen to decrease by some 7% from the low frequency value to that at 900 Hz for the unannealed sample and by about 20% for the annealed sample.

It is easily shown that if the photoconductive decay can be described by a simple exponential decrease with a single time constant τ , then the change in the rms value v(f) of the fundamental of the signal voltage, with chopped light, is given by,

$$v(f)/v_0 = (1 + \omega^2 \tau^2)^{-1/2}$$
 (7.1)

Here ω is the angular frequency, and v_0 is the value of v(f) when $\omega\tau < 1$. An attempt to fit this relation to the experimental points in Fig. 7.8 is shown by the two solid lines. The τ values for these curves are 60 and 170 µsec, which are respectively larger than the τ_s values of 30 and 130 µsec for these two samples obtained by photoconductive decay. This difference may be due to the decay having a more complex time dependence than that expressible as a two-time constant function. In any case, it may be said that the decrease with frequency only starts to become important when ω exceeds $1/\tau_a$.

7.5 Calculated Photoresponse at Low Frequency

With equation (9.1) of chapter 9, values of $\Delta\sigma/(\sigma_0^E_{\sigma})$ were calculated using parameters appropriate to the unannealed samples 11-11 and 11-T on the one hand and the annealed samples 11-AN and 11-ANT on the other. These values are shown by the solid lines in Fig. 7.9 where $\Delta \sigma/(\sigma_0 \overline{E_q})$ is plotted against sample thickness for the case of E/c at a wavelength of 2 µm. The parameters diffusion coefficient D and extrinsic concentration powere obtained hole from transport measurements on the samples at 77 K and the absorption coefficient K value was taken from the work of Tutihasi et al [7.2]. The bulk lifetime \(\tau\)-values used, correspond to the fast photoconductive time constant τ_{f} , since this quantity made the larger contribution to the photoconductive decay. The s-values were chosen to fit the experimental points for the four samples indicated. Values of s larger by an order of magnitude would have been needed if t had been used instead of Tf.

The difference in parameters of the calculated curves needed to fit the experimental points indicates that the increase in photoresponse after annealing is not due to a single cause but to the combined effect of increased mobility

and lifetime and decreased surface recombination velocity. Continuation of the calculated curves to smaller thicknesses (not shown) indicates a maximum photoresponse at a sample thickness of about 6 μm .

7.6 Excess Noise and Detectivity Results

Measurements of the noise from the sample with the current on and off showed that most of it arises from the passage of the current. Therefore, it is appropriate, following Vis [2.26], to use an excess noise parameter defined as $(\mathbf{v}^2 - \mathbf{v}_{\mathrm{T}}^2)/(\mathbf{v}_{\mathrm{dc}}^2 \ \Delta f)$, where \mathbf{v} and \mathbf{v}_{T} are respectively the noise voltages measured with and without sample current, \mathbf{v}_{dc} is the steady voltage between the measuring probes with current flowing and Δf is the bandwidth of the lock-in amplifier-detector. A plot of this excess noise parameter against frequency f on log-log scales is shown in Fig. 7.10 for two of the samples at 77 K; the results of Vis [2.26] are also indicated for comparison. The fall-off with frequency is strong and in one case is steeper than l/f.

The normalized spectral detectivity is defined as $D^*=(A \Delta f)^{1/2}/(NEP)$, where A is the illuminated area and NEP is the noise equivalent power of the detector [7.3]. From the noise voltage and photoconductive responsivity at 900 Hz the D* values were calculated between 1 and 4.2 μ m for the two

thinner samples 11-T and 11-ANT and are plotted against wavelength in Fig. 7.11. The broken line is a curve for a melt-grown sample of Edwards, Butter and McGlauchlin [2.24], which has a maximum D* of 6.4×10^{10} cm Hz $^{1/2}$ W⁻¹. The results for annealed sample 11-ANT are, however, about twice as high as these with a maximum value near 3.5 µm of 1.3×10^{11} cm Hz $^{1/2}$ W⁻¹ (see Table 7.1, column 9). This value is in fact the highest D*-value yet reported at 77 K for melt-grown tellurium [2.24]. Even higher values should be possible for thinner samples and the solid curve shown is an estimate of what should be possible. Here the peak value is that limited by radiation from a 300 K background with a field of view of 180° .

7.7 Discussion and Conclusions

In the present work it is very clear that even fine abrasive surface polishing of the tellurium surfaces greatly decreases the photoconductive response at 77 K, the effect being particularly large at shorter wavelengths below 2 µm. Conversely, annealing results in increased photoconductivity. This is apparently not due to one cause but to the combined effects of increased mobility, increased lifetime and decreased surface recombination velocity.

For tellurium, intrinsic at room temperature, the

photoconductivity increases by more than an order of magnitude with decrease of temperature down to 77 K. Most of the change takes place in the extrinsic range and reflects the increase in the decay time constant with decreasing temperature. With spark source illumination, the photoconductive decay appears to involve a fast decay process with a time constant (τ_f) of a few microseconds, together with a slower one with a time (τ_s) of a few tens of microseconds. non-exponential decay does not arise from a high level of excess carriers, because $\Delta\sigma/\sigma_{o}$, resulting from the spark source excitation, amounts only to about 0.001 or fact that the magnitude of the larger time contribution (Ig) is reduced with steady white background light suggests that it arises from traps. In this case the fast decay contribution may correspond to bulk recombination.

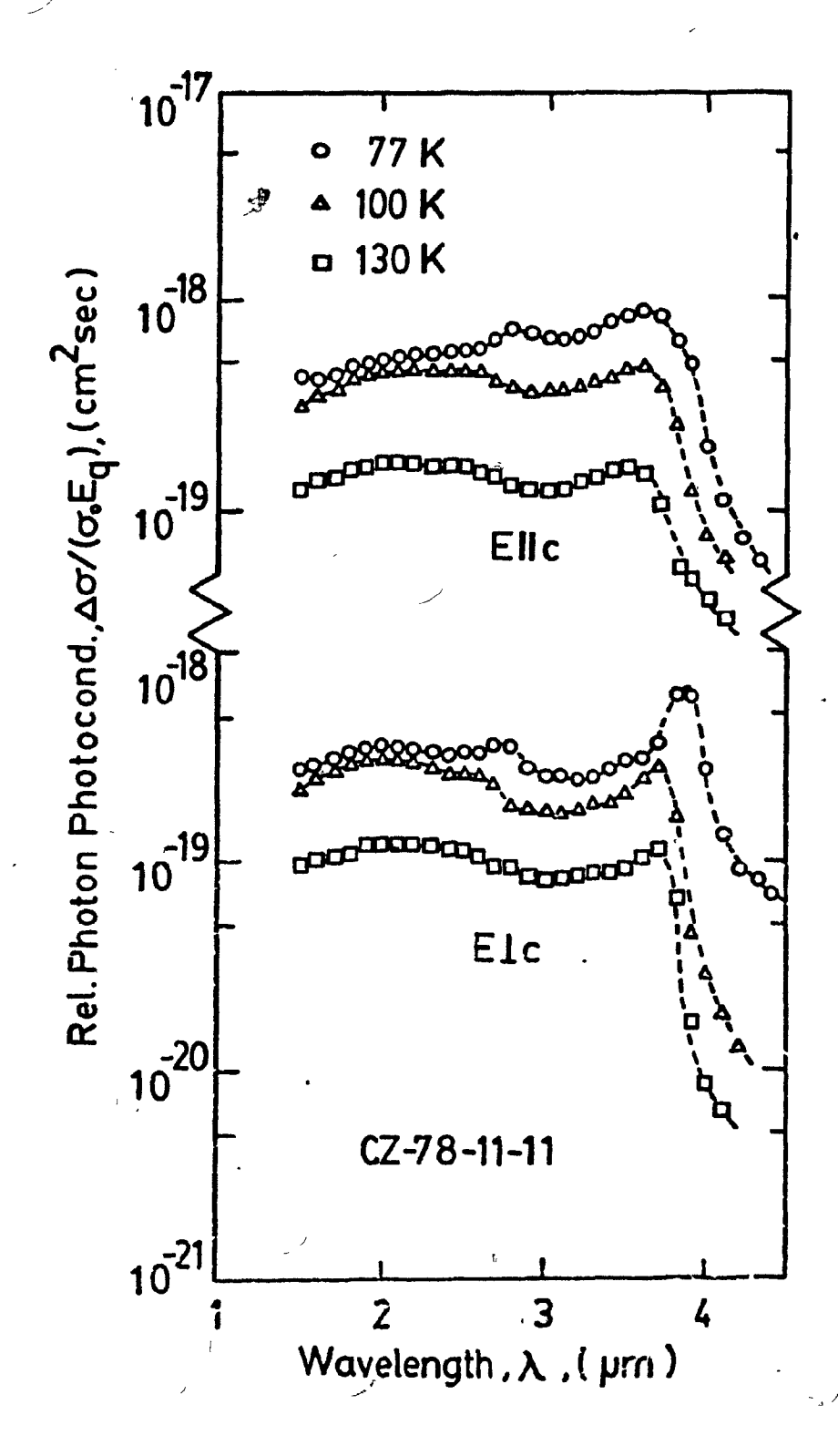
It is found that the excess current noise parameter falls off with frequency at least as fast as 1/f. On the other hand, the decrease of responsivity with frequency is much smaller, so that the signal-to-noise ratio improves with increase of frequency. It may be noted that while annealing increases the responsivity, it also increases the fall-off with frequency. At 900 Hz and a 1 Hz bandwidth, a D* value at 3.5 µm has been obtained which is the highest yet reported for melt-grown tellurium. A value up to the background limited detectivity should be possible with an annealed sample having

a thickness in the range 10 to 100 μ m. Thus with sufficient effort it would appear that melt-grown tellurium could be shown to be of interest for use as an infrared detector material operating at 77 K near a wavelength of 3.5 μ m for application at least up to 1 kHz. However, it could still not compete with InSb at higher frequencies and longer wavelengths [7.3].

C

Table 7.1 Photoconductivity Results in Undoped Tellurium Samples

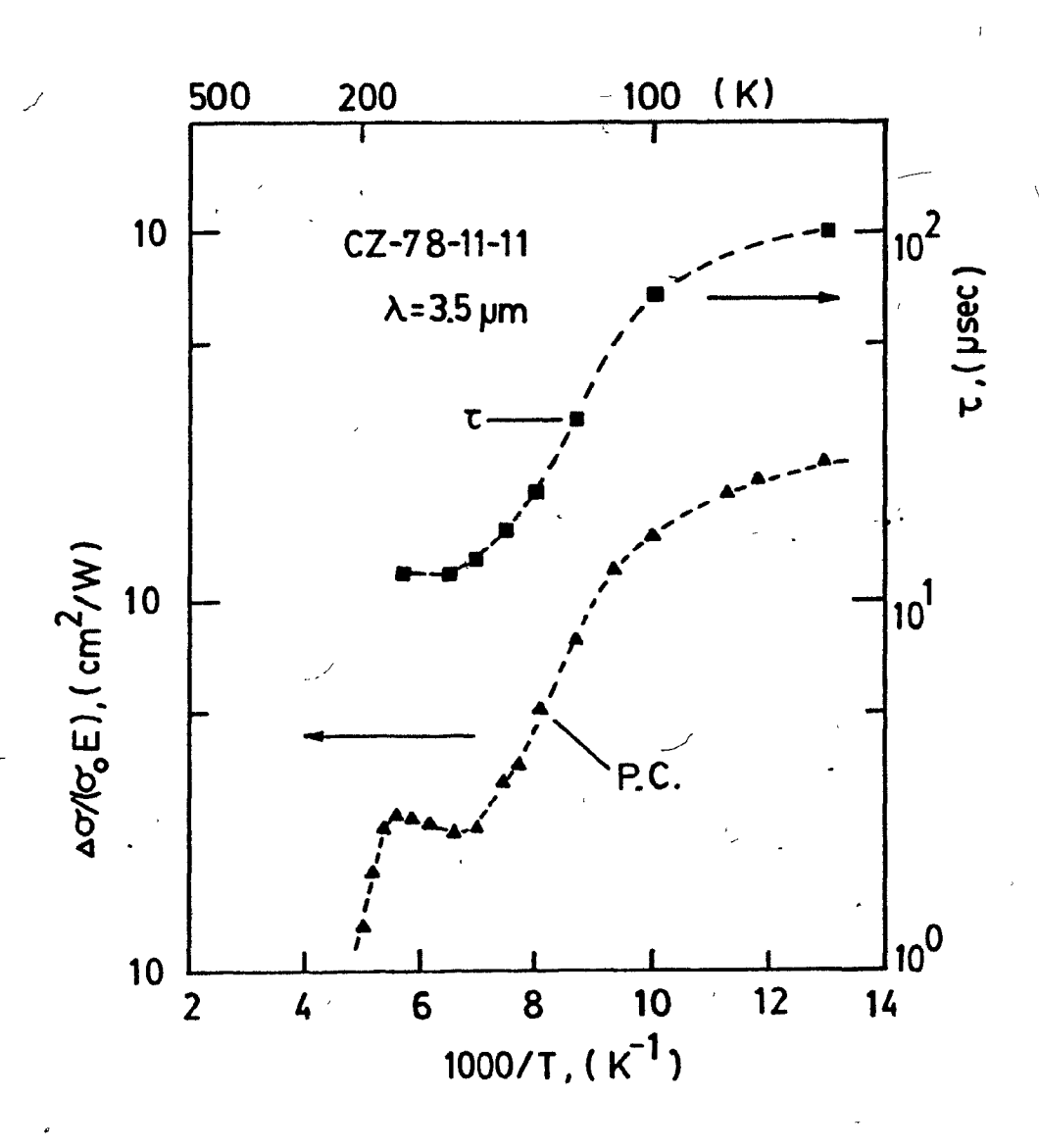
Sample Thickness (Dimension parallel to incident light) (mm)	Width (mm)	Thermal Treatment	Max. $\Delta \sigma / (\sigma_0^E_q)$ at 77 K $(10^{-18} \text{cm}^2 \text{sec})$	Photoconductive Decay at 77 K			Maximum D* at 77 K
				^τ f (μs)	^τ s (μs)	I _f /I _s	900 Hz, 1 Hz BW (cm Hz ^{1/2} W ⁻¹)
1.16	1.75	None	0.6	5 \	70	1	1.8x10 ⁹
1.40	2,20	395 ^O C 168 hrs	2.2	4.5	21	1	
1.51	2.28	None, abrasi- vely polished	0.5				
0.20	1.05	None	2.0	4	30	2	3.7x10 ¹⁰
-		395 ⁰ C	`				,
T 0.15	1.25	168 hrs	5.3	10	130	-c. 1.7	1.3x10 ¹¹
	(Dimension parallel to incident light) (mm) 1.16 1.40 1.51	(Dimension parallel width to incident light) (mm) (mm) 1.16 1.75 1.40 2.20 1.51 2.28	(Dimension parallel Width to incident light) (mm) (mm) 1.16 1.75 None 1.40 2.20 395°C 168 hrs None, abrasi-vely polished 0.20 1.05 None 395°C	to incident light) (mm) (mm) (mm) 1.16 1.75 None 1.40 2.20 395°C 1.51 2.28 None, abrasi- vely polished 0.20 1.05 None 2.0 395°C	to incident light) (mm) (mm) (mm) (mm) (10 ⁻¹⁸ cm ² sec) Tf (µs) 1.16 1.75 None 0.6 5 1.40 2.20 395°C 1.51 2.28 None, abrasi- vely polished 0.20 1.05 None 2.0 4 395°C	to incident light) (mm) (mm) (mm) (mm) (10 ⁻¹⁸ cm ² sec) T f T s (μs) (μs) 1.16 1.75 None 0.6 5 70 1.40 2.20 395°C 1.51 2.28 None, abrasi- vely polished 0.20 1.05 None 2.0 4 30 395°C	to incident light) (mm) (mm) (mm) (mm) (10 ⁻¹⁸ cm ² sec) (μs) (μs) 1.16 1.75 None 0.6 5 70 1 1.40 2.20 395°C 168 hrs 0.5 None, abrasi- vely polished 0.20 1.05 None 2.0 395°C 395°C 395°C 395°C 395°C



C

.()

Fig. 7.1 Relative photon photoconductivity, $\Delta\sigma/(\sigma_O E_q)$, versus wavelength for sample CZ-78-11-11 at three different temperatures with E μ c and E μ c.



to the bar and and a

Fig. 7.2 Relative photon photoconductivity, $\Delta\sigma/(\sigma_0 E_g)$, and average time constant τ at 3.5 µm plotted against the reciprocal of absolute temperature for sample CZ-78-11-11 with E#c. The extrinsic region extends up to about 180 K.

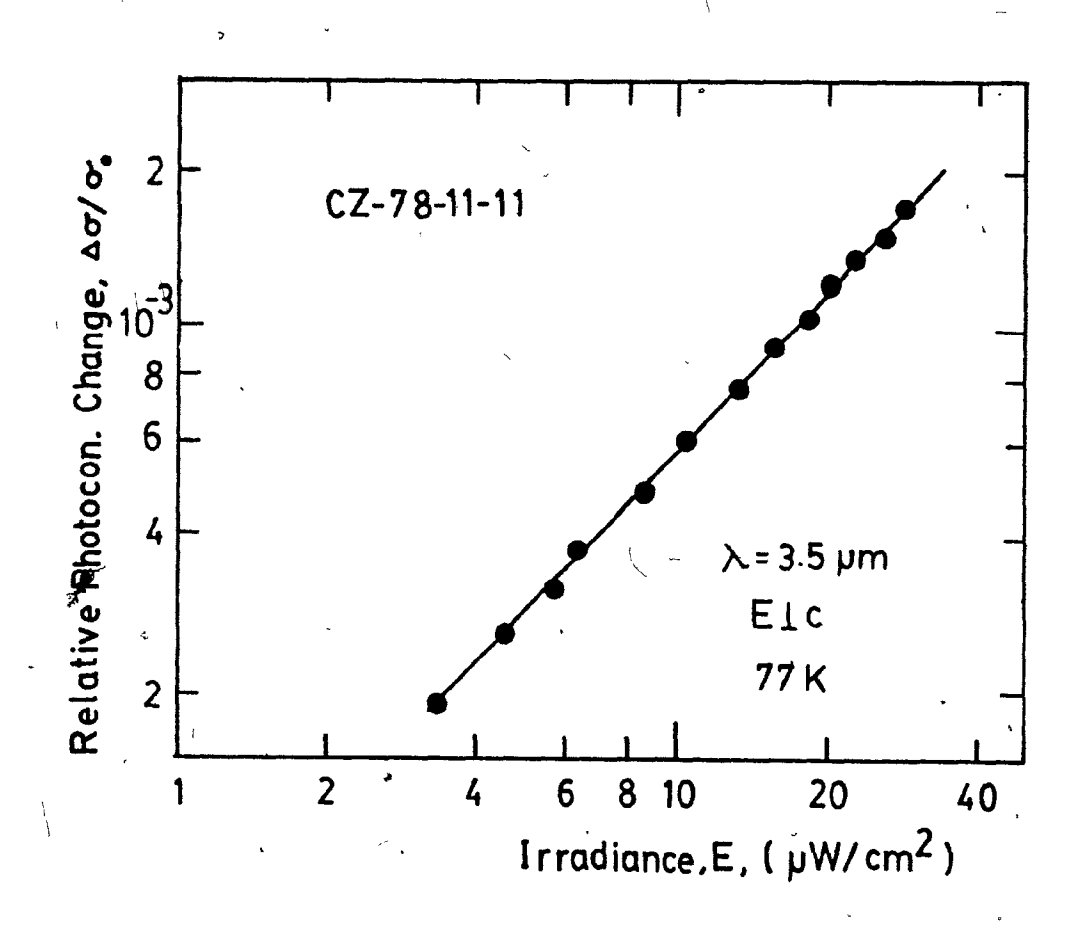


Fig. 7.3 Relative photoconductivity change, $\Delta\sigma/\sigma_0$, plotted against irradiance at 3.8 µm. It is seen that the photoconductivity increases linearly with the irradiance.

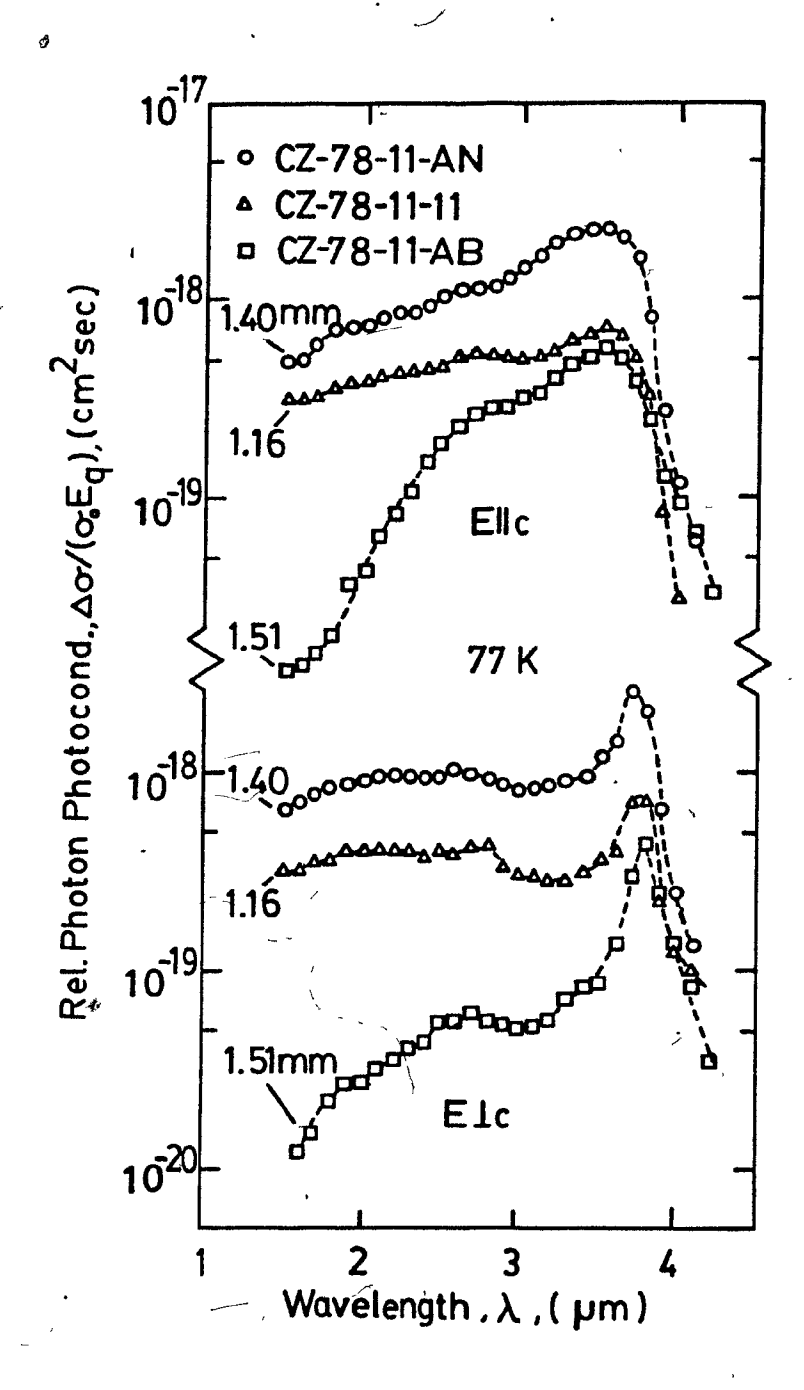
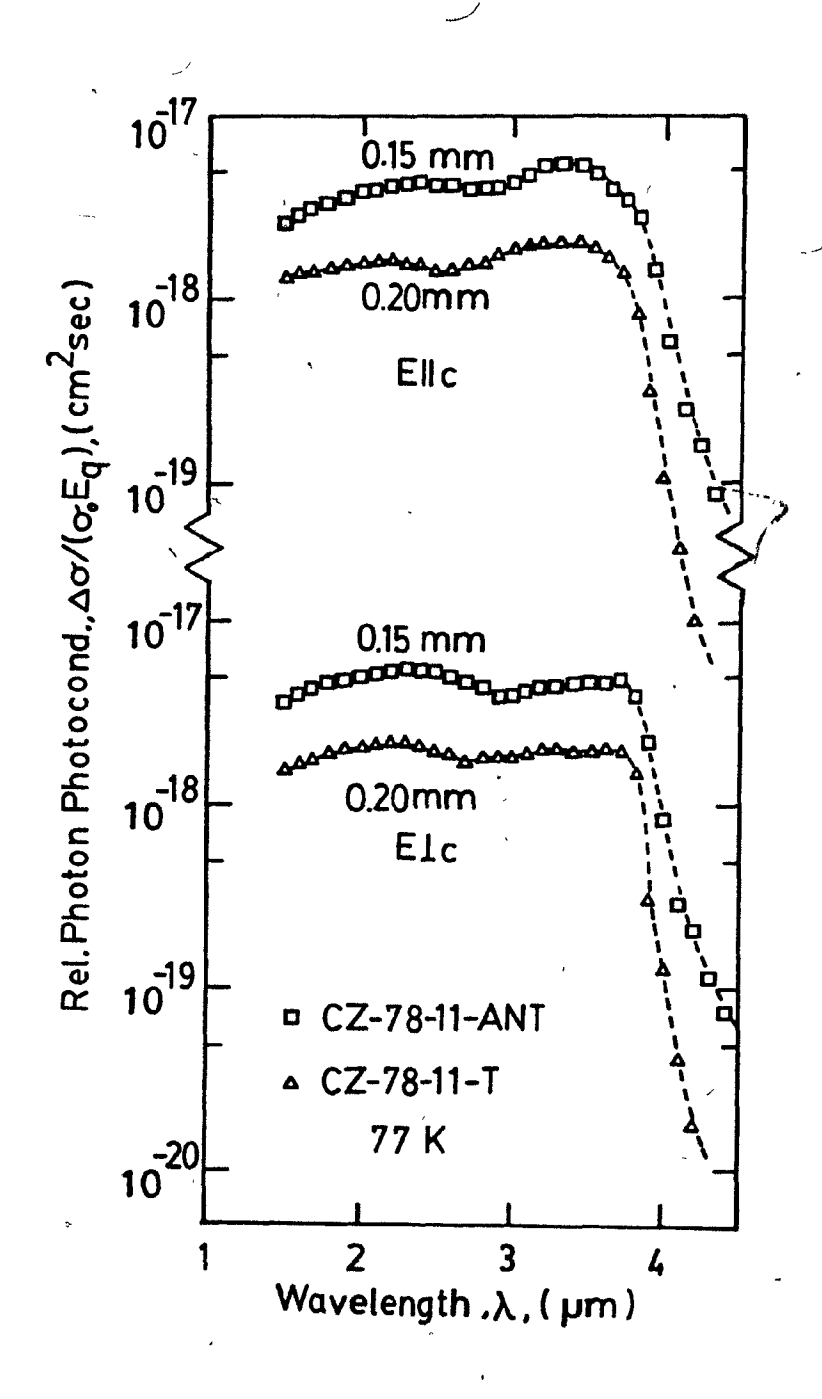


Fig. 7.4 Relative photon photoconductivity at 7.7 K plotted against wavelength for three samples prepared by different treatments with E#c and E1c. Samples C2-78-11-AN annealed; -11 unannealed; -AB abrasively polished.



--

Fig. 7.5 Relative photon photoconductivity at 77 K versus wavelength for two thinner samples with (CZ-78-11-ANT) and without (-11-T) annealing.

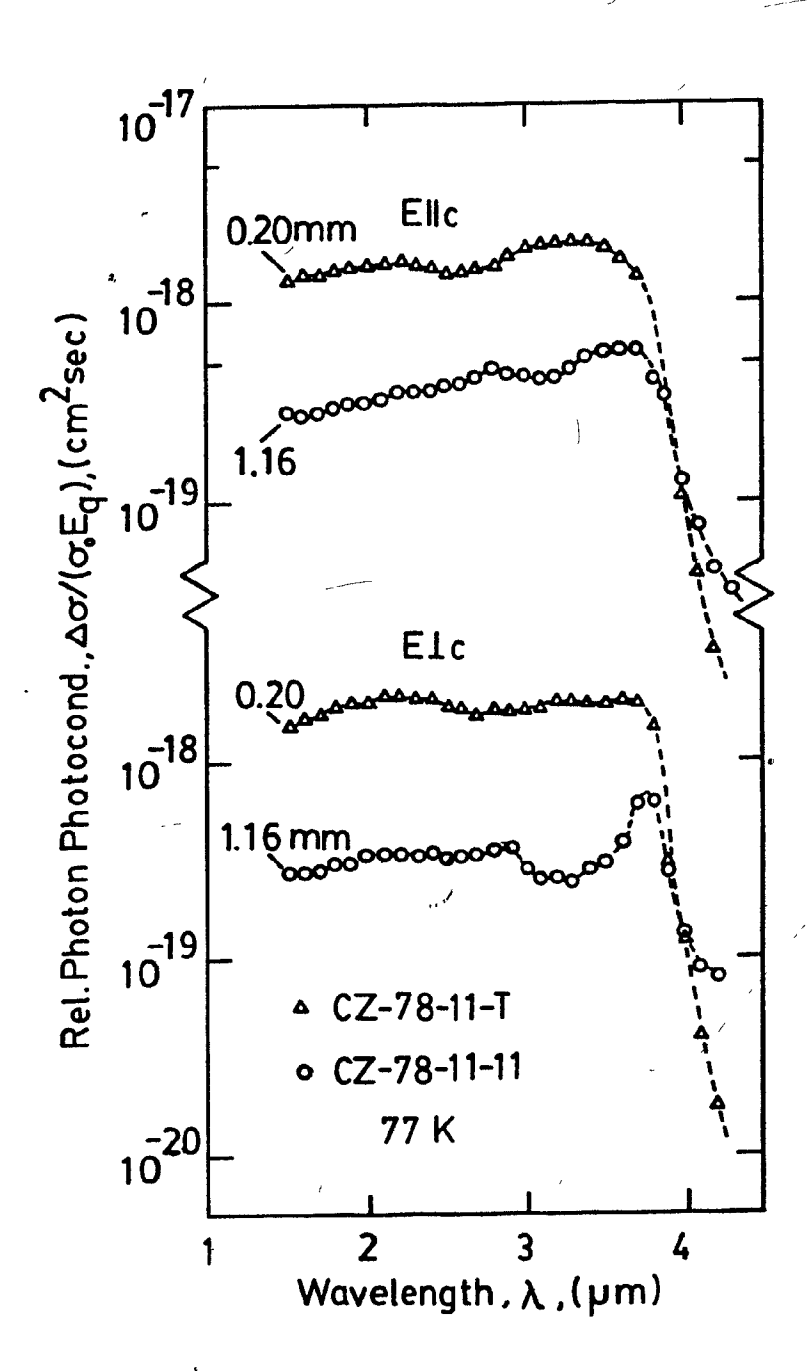


Fig. 7.6 Relative photon photoconductivity at 77 K versus wavelength for two samples of different thickness.

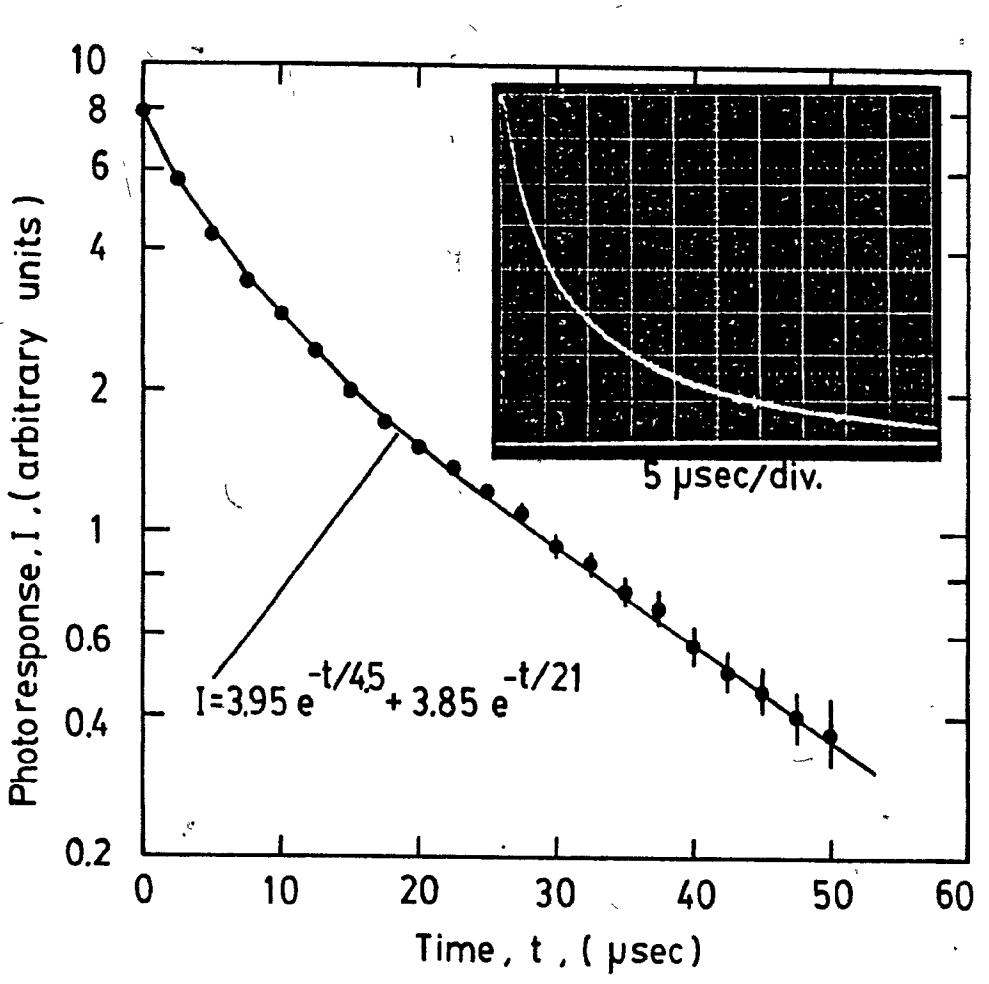


Fig. 7.7 Relative magnitude of the photoconductive transient decay following spark source excitation for sample CZ-78-11-11 at 77 K plotted against time. The solid curve is the result of fitting with the two-time constant equation shown.

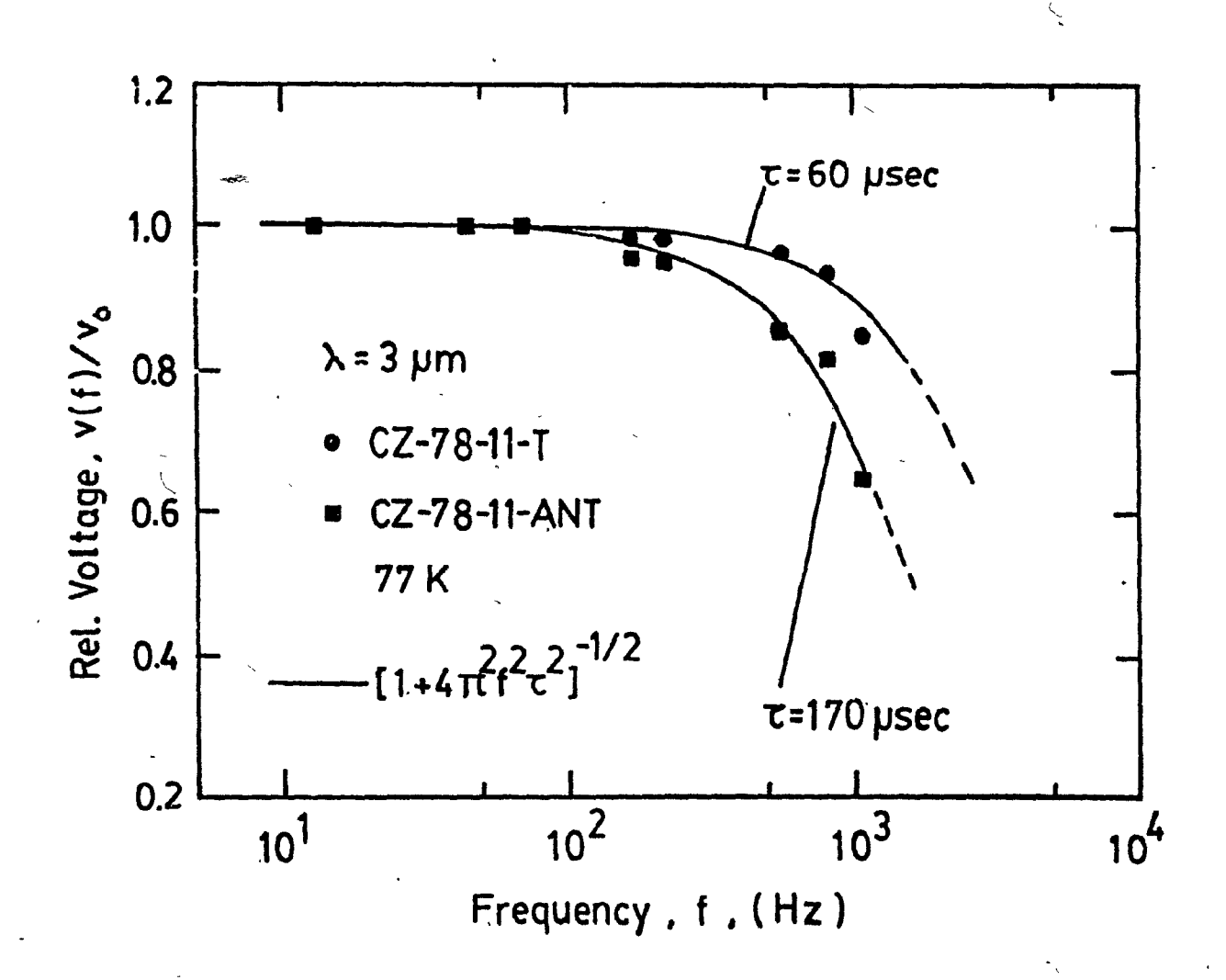
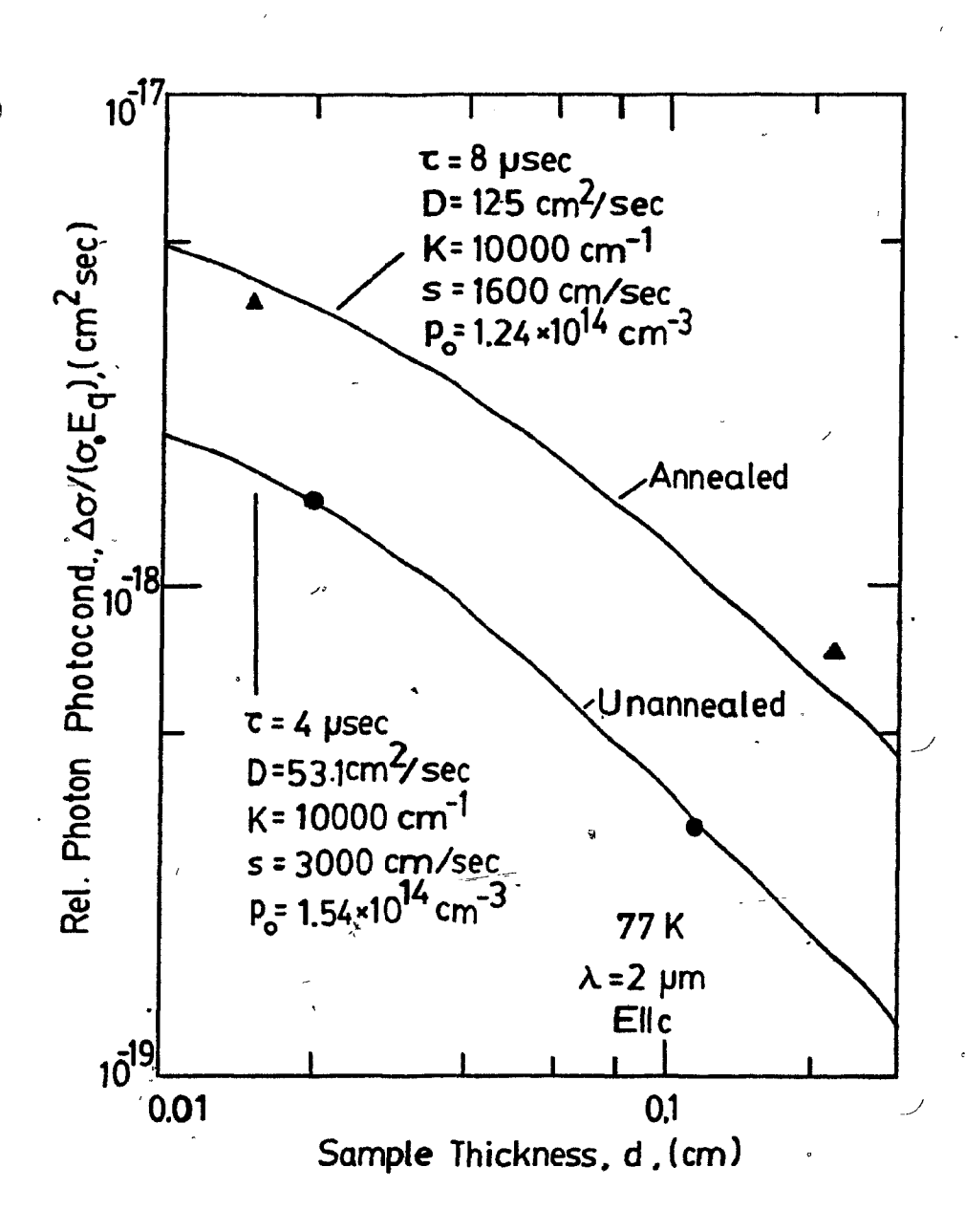


Fig. 7.8 Relative photoconductive voltage, $v(f)/v_0$, plotted against frequency. The solid lines represent the variation of $(1+\omega^2\tau^2)^{-1/2}$ with τ fitted to the experimental points.



の かんしゅう かんかい かんかい

Fig. 7.9 Calculated variation of photon photoconductivity with sample thickness using equation (9.1) of chapter 9. The parameters were chosen to correspond to the plotted experimental points of the two annealed and two unannealed samples.

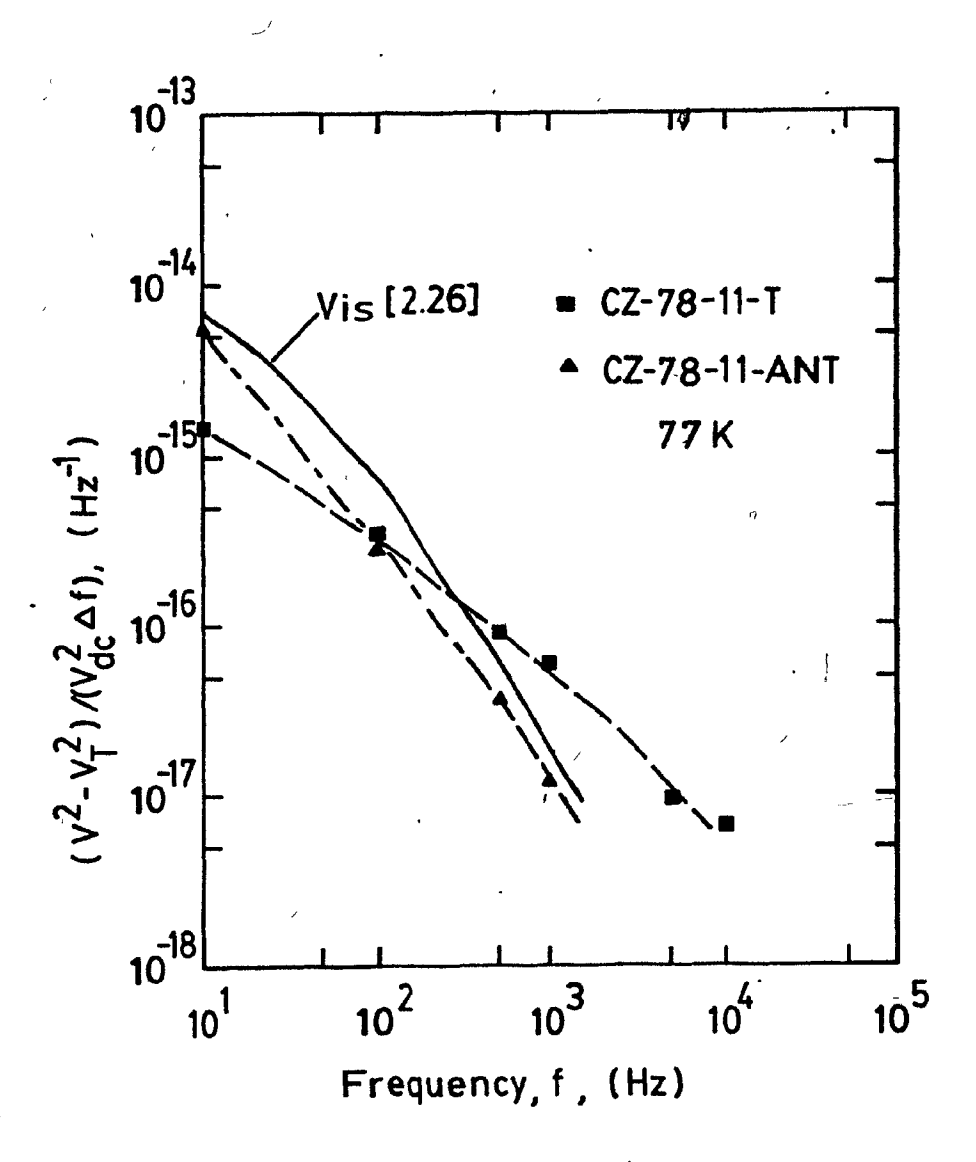


Fig. 7.10 Normalized noise parameter, $(v^2-v_T^2)/(v_{dc}^2\Delta f)$, plotted against frequency for samples CZ-78-11-T and -ANT, together with a curve of Vis [2.26].

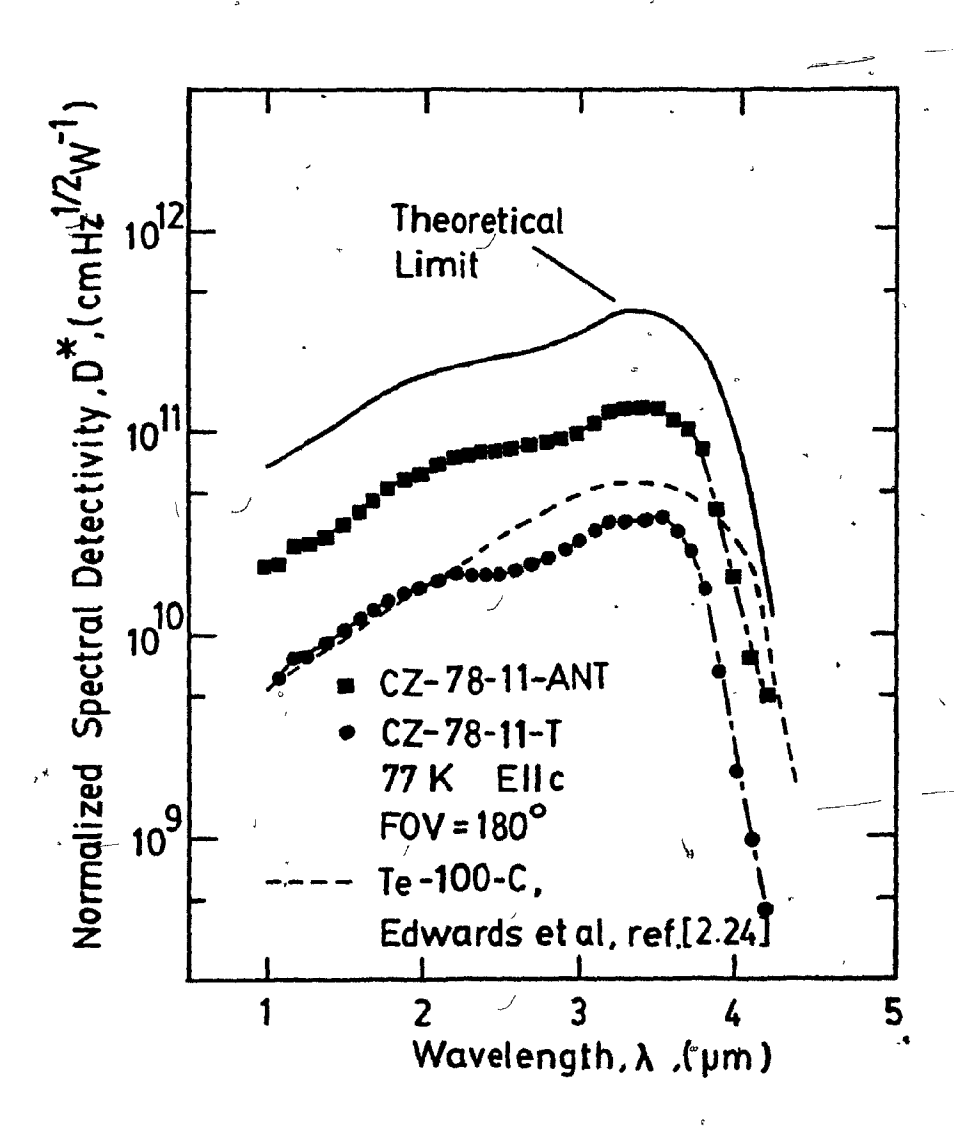


Fig. 7.11 Normalized spectral detectivity D* plotted against wavelength for samples CZ-78-11-T and -ANT at 77 K with E/c. The broken curve is from ref. [2.24] on melt-grown Te, while the solid line is a theoretical curve for background limited conditions in the present case.

()

CHAPTER 8 PHOTOCONDUCTIVITY RESULTS IN

SexTe_{1-x} ALLOYS

8.1 Introduction

In this chapter the results of photoconductivity measurements of samples from the Se_xTe_{1-x} alloys are presented. These consisted of photoconductivity obtained with chopped light as a function of wavelength and with pulsed light as a function of time, together with measurements of dark electrical resistivity and Hall coefficient. The measurements should be considered as preliminary because of the fact that the preparation of the samples was in a much less advanced stage than was the case with pure tellurium. Never-the-less, the displacement of the photoconductive peaks with composition was very clear, as will be seen. The photoconductivity results are the first reported for the Se_xTe_{1-x} alloys at liquid nitrogen temperature.

8.2 Steady State Photoconductive Spectral Response

For the Te-rich Czochralski-grown alloys the variation of the relative photoconductivity, $\Delta\sigma/(\sigma_{Q}E_{q})$, with wavelength between about 1 and 4.2 μm is shown in Fig. 8.1 for E1c and in Fig. 8.2 for E1c at 77 K. It is noted that as the selenium content increases from 0 to 10 at.% there is a displacement of

the peaks to shorter wavelengths, coupled with an increase in , the magnitude of the photoconductivity of the maximum and of the values at shorter wavelengths. The shift of the curves also causes a decrease of photoconductivity on the longer wavelength side of the maximum.

Figs. 8.3 and 8.4 'show the variation photoconductivity at 77 K with wavelength for the samples over the complete composition range from 0 to 100 at. &Se. It is clear that there is a steady wavelength displacement of the maxima from about 3.8 μm to about 0.8 μm. At the same time, there is also an increase of photoconductivity magnitude by " some 5 orders of magnitude (see also Table 8.1). A difference in the photoconductivity with change of the orientation of the plane of polarization with respect to the c-axis between Elc and E/c was onot discernible in samples containing 20 at.% or more of selenium. The variation of $\Delta\sigma/(\sigma_{O}^{E})$ with wavelength is plotted separately for selenium in Fig. 8.5 together with experimental results of Stuke [2.32] at a similar temperature (93 K). The maximum occurs at about 0.72 μm in the present results, compared with 0.71 µm from the curve of Stuke and 0.67 µm from measurements of Prosser, [2.30] (not shown) at 95 K.

8.3 Transient Photoconductivity

decrease of photoconductivity following pulsed illumination was recorded using an oscilloscope or, in the case of the Se-rich alloys, using an X-Y recorder connected to the electrometer. A typical decay curve is shown in the inset to Fig. 8.6, where the main part of the figure shows the variation plotted on semilogarithmic scales. / As with pure tellurium, it is found that the curve can be fitted with the sum of two exponentials, one with a "fast" time constant, τ_f , and the other with a slower one, $\boldsymbol{\tau}_{\mathbf{s}^{\bullet}}$. For the particular composition in Fig. 8.6 τ_f was 50 and τ_s was 600 µsec. This procedure was done for all the samples, yielding the time constant values for both τ_s and τ_f . For compositions with more than 90 at. & Se the decay was particularly complex. Figs. 8.7 and 8.8 the values of τ_f and τ_g are respectively plotted against the selenium content in the alloys. It is seen that the time constant variation covers some six orders of magnitude in going from tellurium to selenium, with τ_{f} ranging from microseconds to seconds.

In Fig. 8.9 the maximum values of $\Delta\sigma/(\sigma_0 E_q)$ are plotted against the τ -values of the corresponding alloys on log-log scales. The photoconductivity appears to vary approximately as

 $\tau_{\rm f}^{0.4}$ up to $\tau_{\rm f}$ =0.1 sec, corresponding to about 50-60 at. Sec. Thereafter, the slope is steeper corresponding to a dependence roughly of the form $\tau_{\rm f}^2$.

€

8.4 Electrical Resistivity and Hall Mobility

The variation of the dark electrical resistivity measured at 77 K with composition is shown in Fig. 8.10, where it is seen that there is a change of about 5 decades in going from Te to Se. About the same magnitude of change was observed for the room temperature resistivity by Bahl and Chen [2.18] (broken line in Fig. 8.10).

Experimental points for Hall mobility $R_{H}\sigma_{O}$ at 77 K plotted against composition up to 40 at.% Se are shown in Fig. 8.11. It was not possible to measure the Hall effect at greater selenium concentrations with the apparatus employed because of very low mobility values. The measured values are seen to be consistent with the Hall mobility results (broken curve in Fig. 8.11) of Bahl and Chen [2.18].

8.5 Conclusions and Speculations

It is evident from the wavelength shift of the photoconductivity maxima that the alloys show a continuous change of energy band gap with composition. This will be

treated more specifically in chapter 9. The existence of the two decay times was discussed for pure tellurium in chapter 7, where it was speculated that the shorter value τ_f might be the recombination lifetime. The increase of such a quantity with selenium content would explain the increase of the photoconductive responsivity in the alloys. However, it is difficult to accept lifetimes of the order of seconds which are observed for τ_f at the Se-rich compositions.

From a device point of view, the alloys are seen to offer the possibility of sensitive detector materials operating at wavelengths between about 0.8 and 3.5 μm . However, the response times for such photoconductive devices would be very long, especially for the alloys at the shorter wavelengths.

In view of the importance of annealing in the case of pure tellurium, it is clear that heat treatment would be important in the case of the $\mathrm{Se_{x}Te_{1-x}}$ alloys as well. In fact lattice imperfections are likely to be much more prevalent as the selenium content increases. For these reasons the results in the present chapter must be regarded as only initial characterization measurements to observe the main trends.

Table 8.1 Se Te Samples Used in the Photoconductivity Measurements

	Sample Composition	Thickness	Width (mm)	Preparation	Max. $\Delta \sigma / (\sigma_{\mathbf{Q}}^{\mathbf{E}})$	
,		(mm)			$(10^{-18} \text{ cm}^2 \text{ sec})$	
	Se _{0.04} Te _{0.96} *	1.73	1.75	chemical	2.5	
	Se _{0.1} Te _{0.9} *	1.50	1.50	chemical	6.0	•
	Se _{0.18} Te _{0.82}	1.50	2.10	abrasive	` 4.0	
	^{Se} 0.23 ^{Te} 0.77	1.70	2.45	abrasive	4.0	
	^{Se} 0.28 ^{Te} 0.72	1.90	2.25	abrasive .	10.0	
	^{Se} 0.45 ^{Te} 0.55	1.26	2.03	abrasive	_ 40.0	
	Se _{0.54} Te _{0.46}	1.78	2.00	abrasive	35.0	\
	Se _{0.58} Te _{0.42}	1.25	1.66	abrasive	70.0	
	^{Se} 0.75 ^{Se} 0.25	1.07	1.52	abrasive	1,020.0	_
	Se _{0.9} Te _{0.1}	2.63	2.01	abrasive	40,000.0	
	Se	1.26	, 2.12	abrasive	100,000.0	

^{*} Czochralski-grown samples.

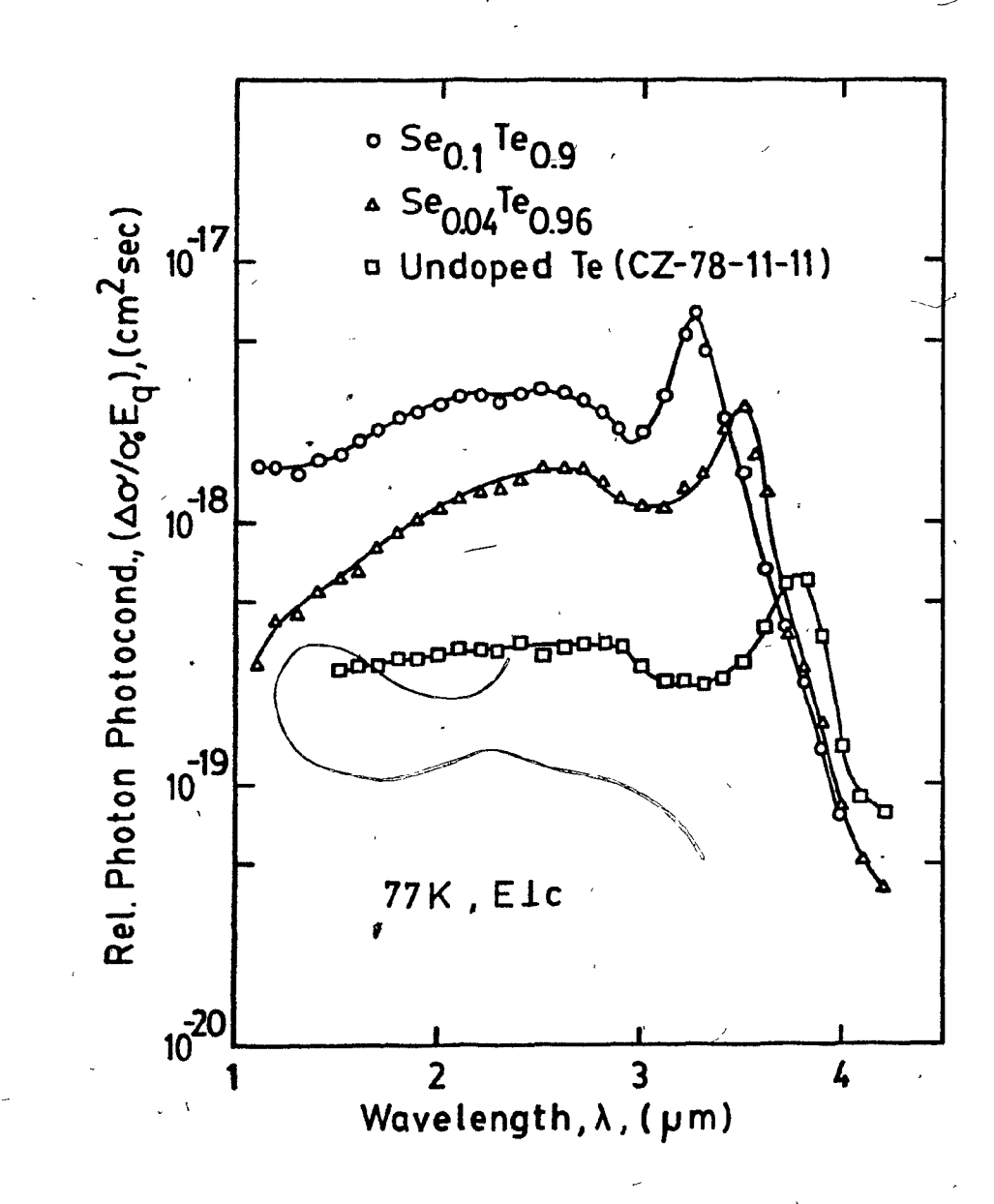


Fig. 8.1 Relative photon photoconductivity at 77 K versus wavelength for samples (crystals grown by the Czochralski method) with 0, 4 and 10 at.% of selenium for Elc.

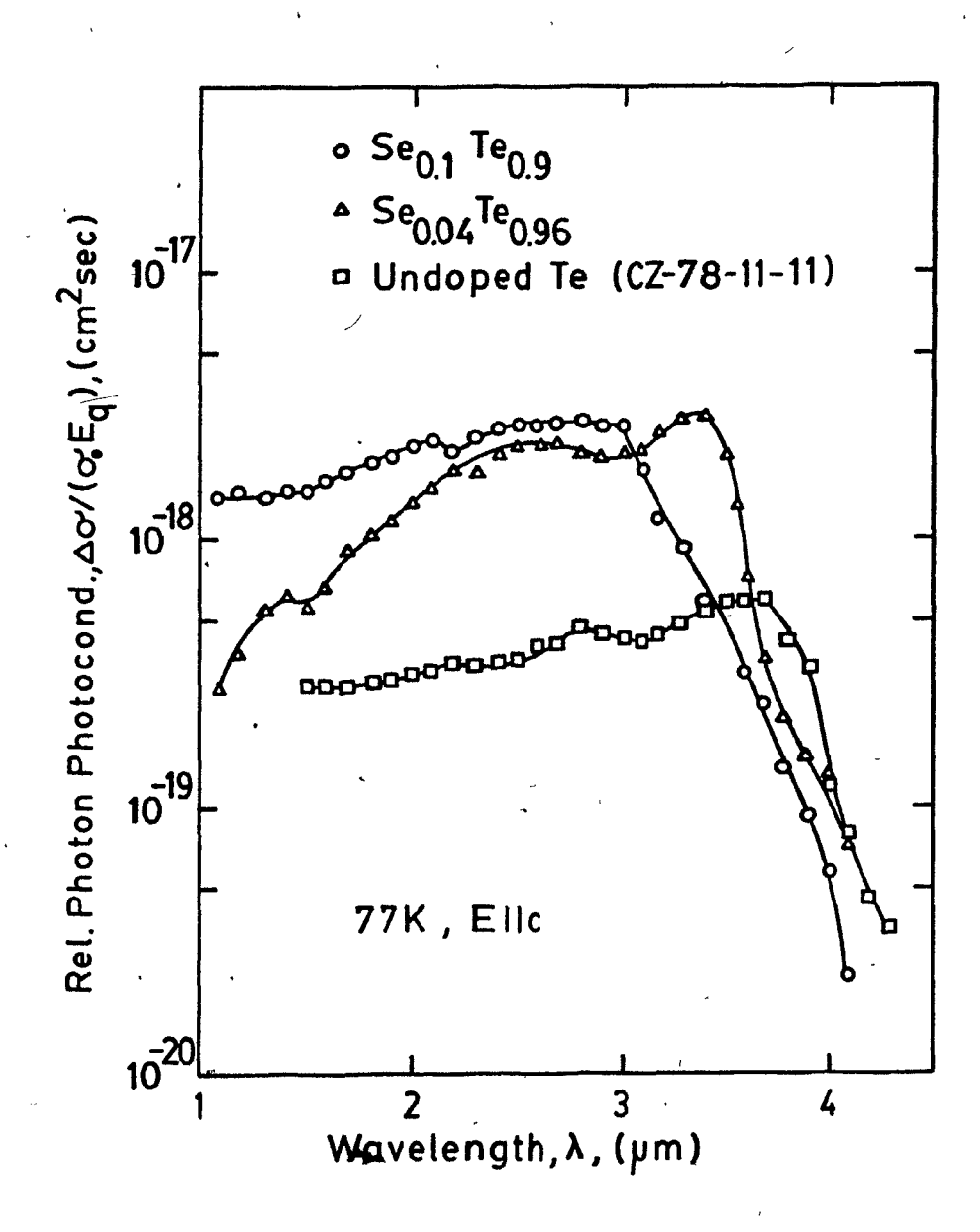


Fig. 8.2 Relative photoconductivity at 77 K versus wavelength for samples (crystals grown by the Czochralski method) with 0, 4 and 10 at.% of selenium for Esc.

j.

Fig. 8.3 Relative photon photoconductivity versus wavelength for samples selected from the slowly cooled-melts and the Czochralski-grown selenium crystal.

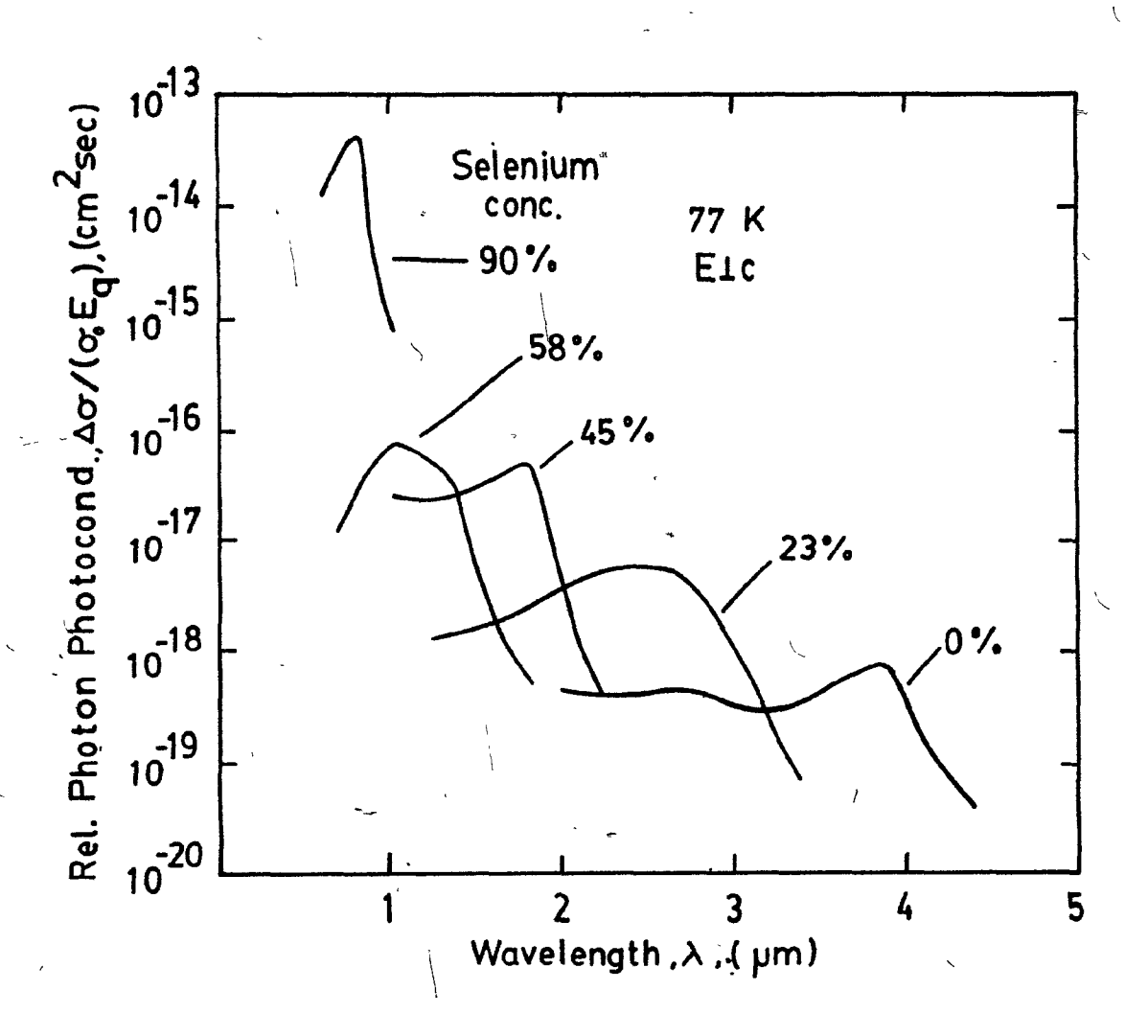


Fig. 8.4 Relative photon photoconductivity versus wavelength for samples selected from the slowly cooled-melts.

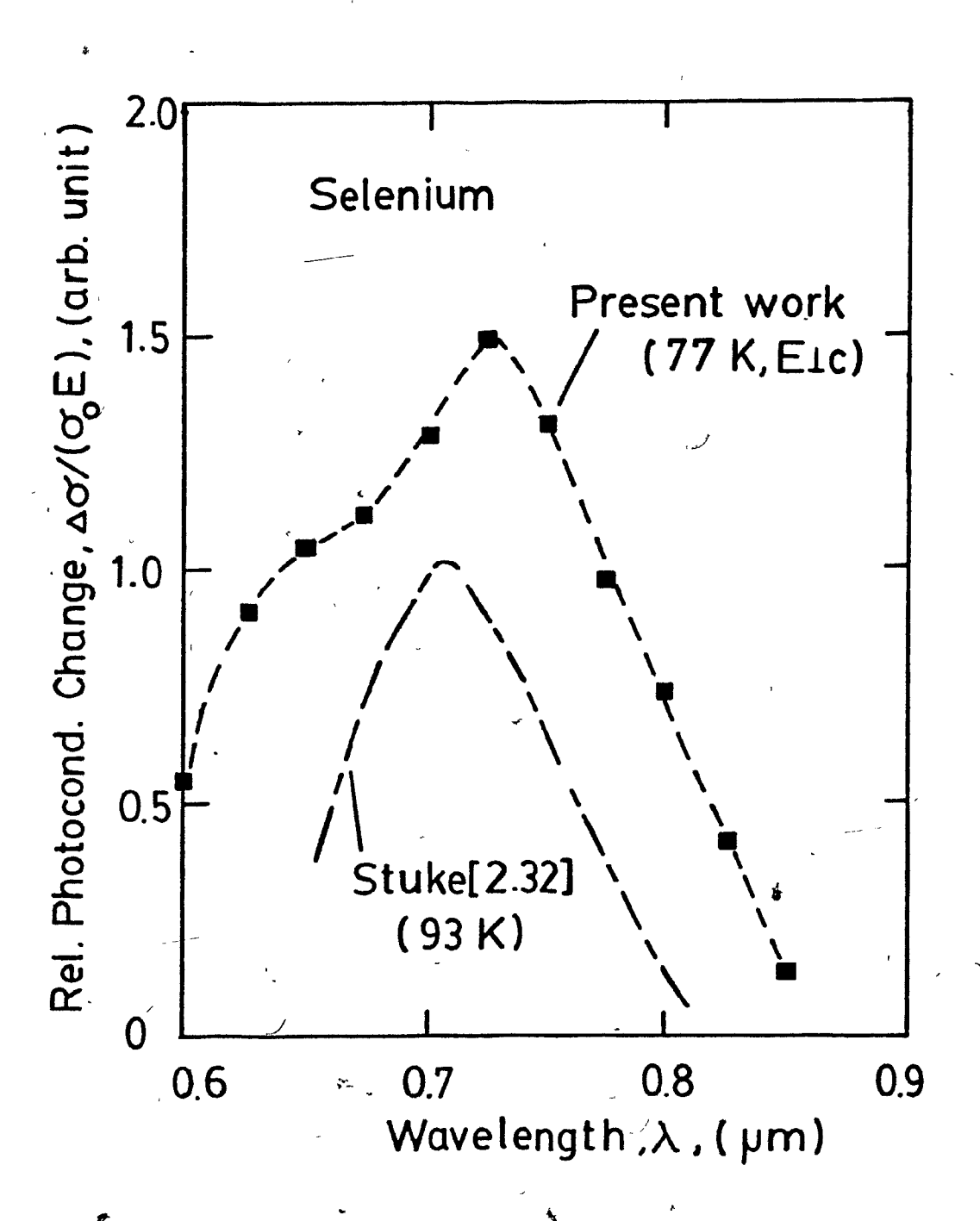


Fig. 8.5 Spectral dependence of photoconductivity for selenium samples.

()

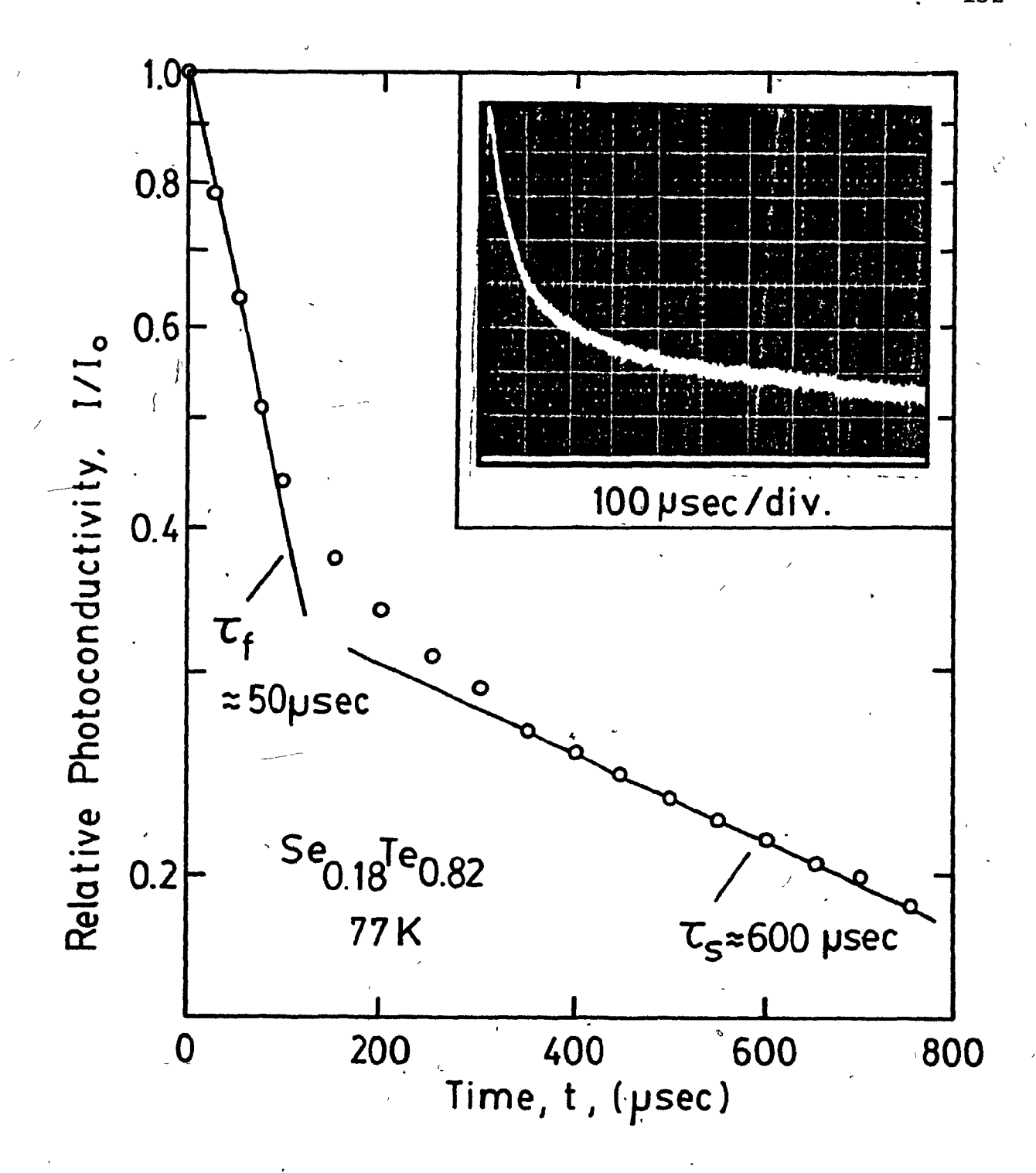


Fig. 8.6 Relative magnitude of the photoconductive transient decay for sample Se_{0.18}Te_{0.82} at 7 against time on semi-logarithmic scales. at 77 K plotted

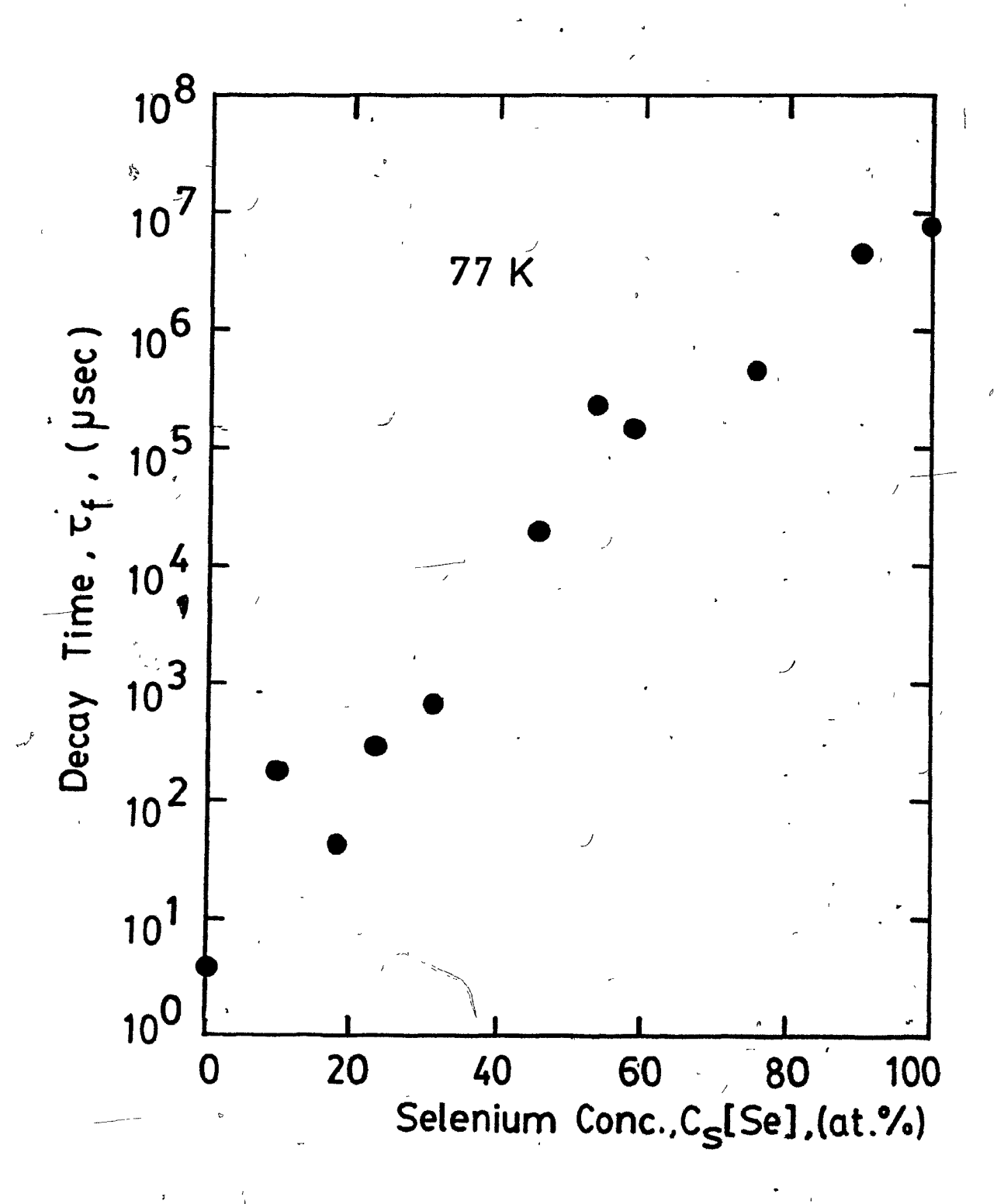


Fig. 8.7 The fast decay time constant, τ_f , as a function of the selenium concentration in the solid.

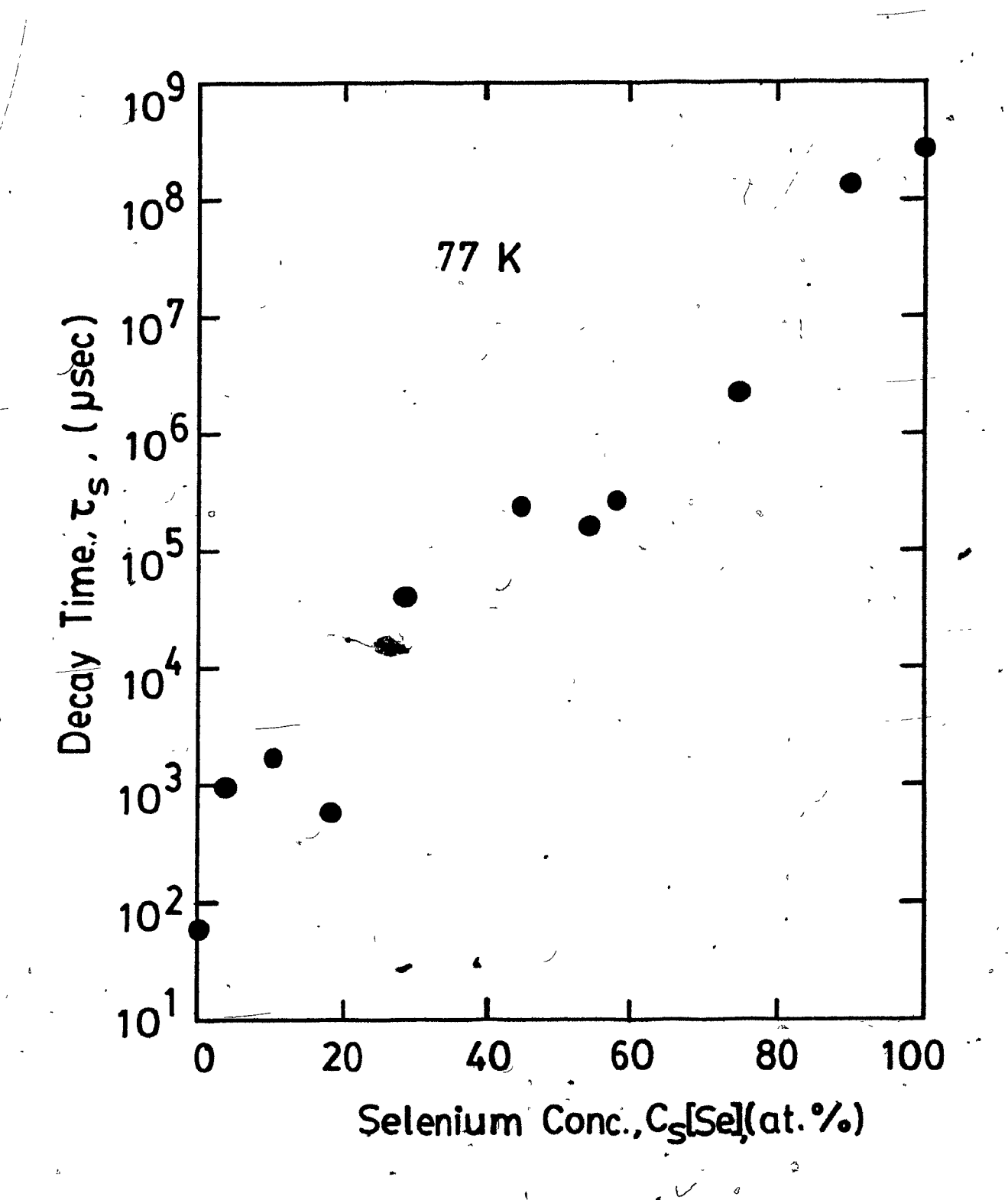


Fig. 8.8 The slow decay time constant, $\tau_{\rm S}$, as a function of the selenium concentration in the solid.

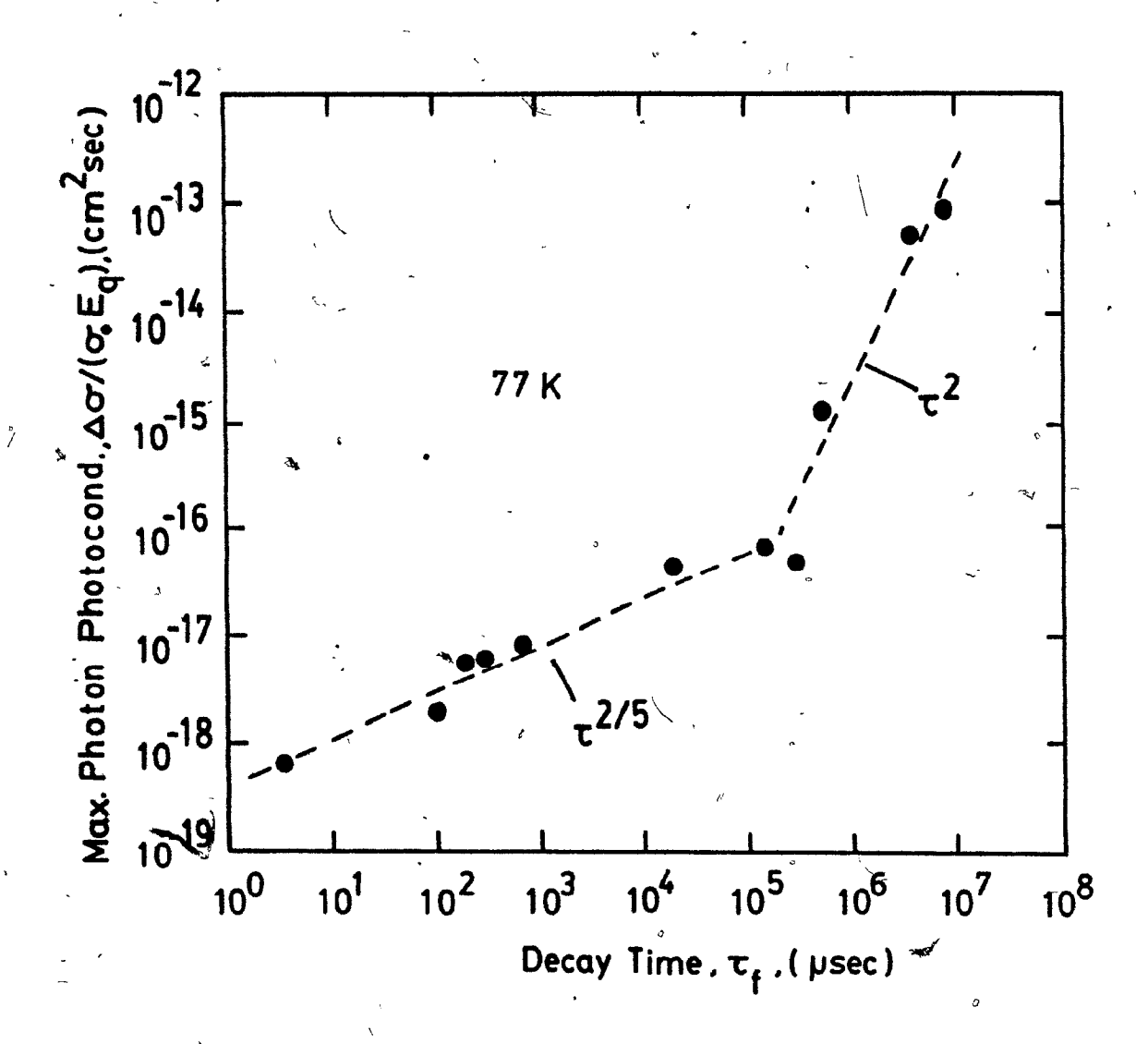
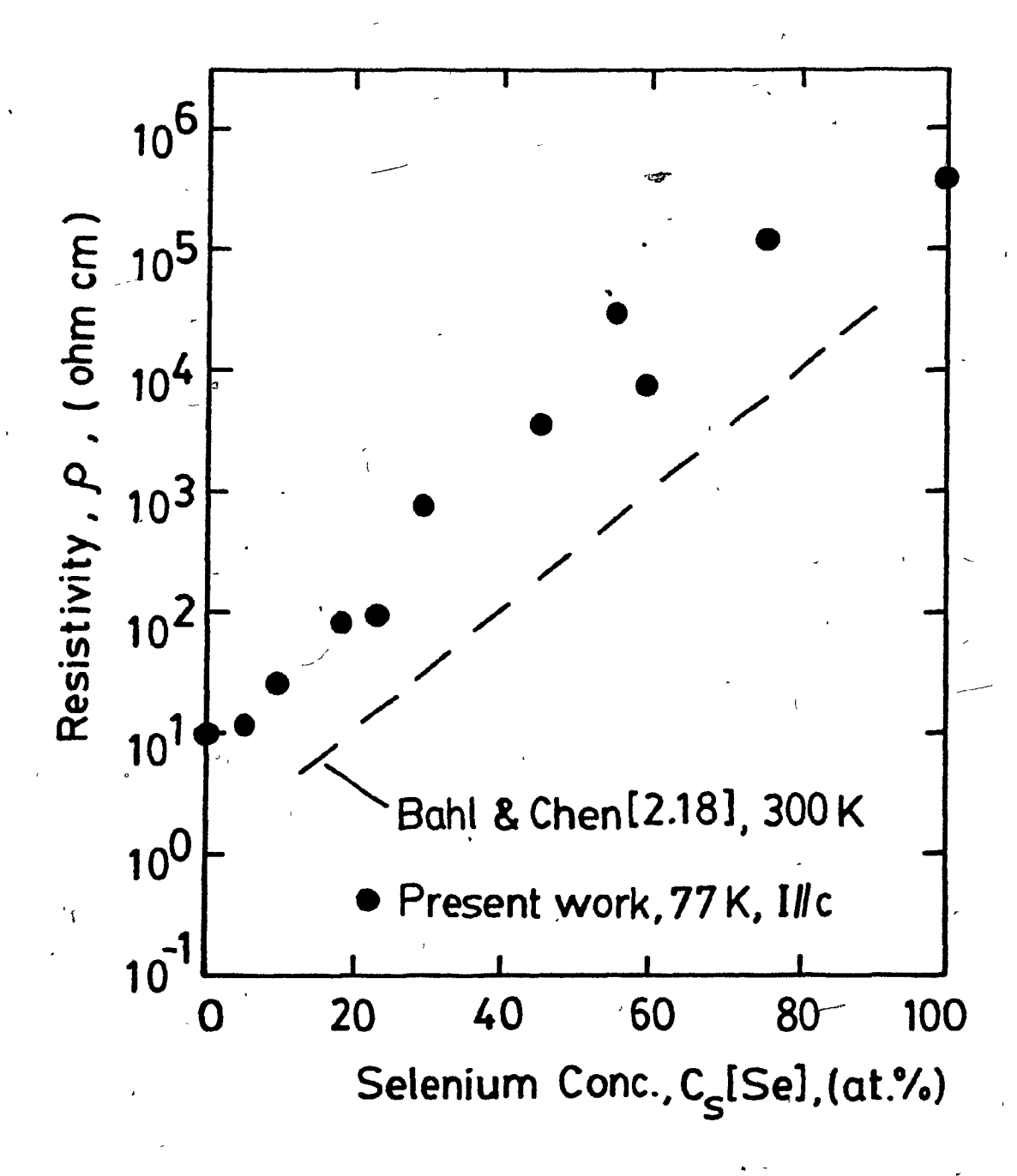


Fig. 8.9 Maximum relative photoconductivity plotted against the fast decay time constant.



0/

Fig. 8.10 Resistivity at 77 K as a function of the selenium concentration in the solid.

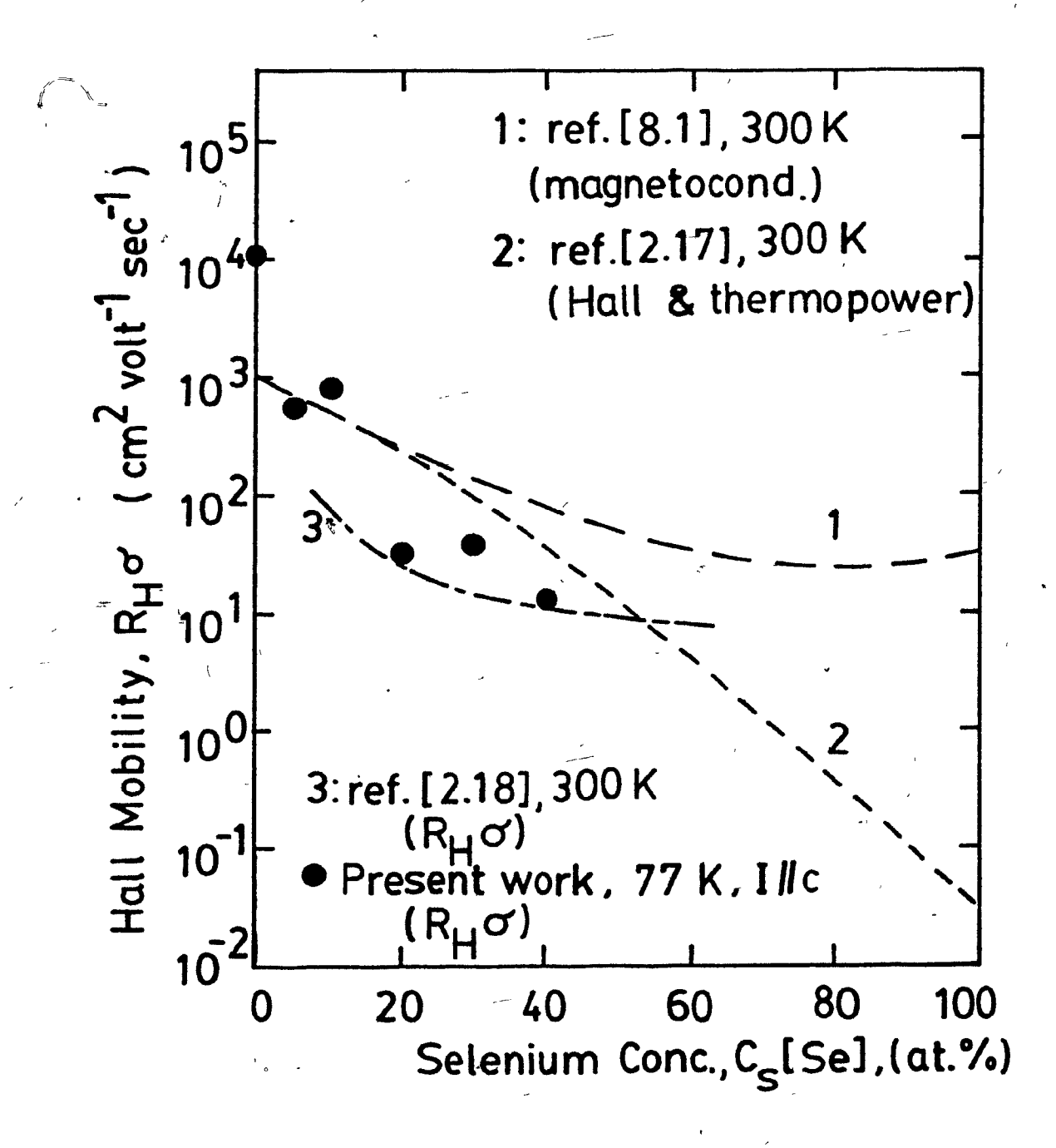


Fig. 8.11 Hall mobility plotted against the selenium concentration in the solid. Shown also are the results at 300 K reported in the literature.

CHAPTER 9 CALCULATION OF ABSORPTION COEFFICIENTS AND ENERGY GAPS

9.1 Introduction

It is especially interesting from a scientific point of view to examine the absorption edge of semiconductors, since this provides information on the band structure. specifically it can give the magnitude of the energy gap and determine whether the electron interband transitions are direct or indirect. In the present work, the absorption coefficient (K) was not directly measured in the materials but possible to calculate this quantity from photoconductivity if other parameters are known. As pointed out by Grosse and Winzer [2.27], such calculated values have advantage the directly over measured absorption coefficients in that they are the result of photogenerated carriers, whereas in the latter case absorption can also arise from non-electronic transitions such as lattice vibrations. Further, absorption coefficients derived from photoconductivity can provide K-values over wavelength ranges where they are very large and difficult to measure directly because very thin samples would be required. Never-the-less, as will be seen, calculated K-values require parameters which may not be easily available, such as surface recombination velocity and in addition the theory of photoconductivity may

not be complete enough to take all relevant factors into account.

In this chapter absorption coefficients are calculated from photoconductivity firstly for pure tellurium and then for the $Se_{x}Te_{1-x}$ alloys using a relatively simple theory. In the latter case, this enabled the variation of energy gap with composition to be determined at 77 K.

9.2 Theory

9.2.1 Photoconductivity

If light is incident on an infinite slab of p-type semiconductor of thickness d and having an equilibrium hole concentration \mathbf{p}_{O} , then the relative change of conductivity $\Delta\sigma/\sigma_{O}$ per unit photon flux density $\mathbf{E}_{\mathbf{q}}$ is given by (for derivation see ref. [9.1]):

$$\frac{\Delta \sigma}{\sigma_{OE_{q}}} = \frac{1+b}{p_{O}d} \frac{\tau}{1-K^{2}L^{2}} \left[1-e^{(-Kd)} + KL \frac{(KL-\alpha)e^{(-Kd)} - (KL+\alpha)}{1 + \alpha \coth(d/2L)}\right] , (9.1)$$

where b is the electron-to-hole mobility ratio, K is the absorption coefficient and L is the diffusion length. Both excess electrons and holes are assumed to contribute to $\Delta\sigma$

with a common lifetime τ . The quantity α represents sL/D= $s(\tau/D)^{1/2}$, where s is the recombination velocity of the two surfaces and D is the diffusivity of the minority electrons.

As the absorption coefficient K is increased, $\Delta\sigma/(\sigma_O^E_q)$ from equation (9.1) increases to a maximum between Kd=l and 10 and thereafter decreases towards a plateau at infinite K given by:

$$\left(\frac{\Delta\sigma}{\sigma_{o}E_{q}}\right)_{Kd=\infty} = \frac{1+b}{p_{o}d} \frac{\tau}{1 + \alpha \coth(d/2L)} \qquad (9.2)$$

It is noted that the ratio of the photoconductive change to that of the plateau from equations (9.1) and (9.2) is given by:

$$\frac{\left(\frac{\Delta\sigma}{\sigma_{O}E_{q}}\right)}{\frac{\Delta\sigma}{\left(\frac{\Delta\sigma}{\sigma_{O}E_{q}}\right)Kd=\infty}} = 1-e^{\left(-Kd\right)} + \alpha \frac{\coth\left(d/2L\right)\left(1-e^{\left(-Kd\right)}\right) - KL\left(1+e^{\left(-Kd\right)}\right)}{1-K^{2}L^{2}}, (\beta.3)$$

which is independent of p_0 and b.

For a thick sample, in which d >>1/K, L, the photoconductivity from equation (9.1) reduces to:

$$\frac{\Delta\sigma}{\sigma_{OE_{\mathbf{q}}}} = \frac{(1+b) \left(1 + \frac{\alpha}{1+KL}\right)\tau}{p_{O_{\mathbf{q}}}d(1+\alpha)} \qquad (9.4)$$

representing proportionality to 1/d.

For a thin sample, in which $d \ll 1/K$, L, the photoconductivity from equation (9.1) reduces to:

$$\frac{\Delta \sigma}{\sigma_{\mathbf{o}^{\mathbf{E}}\mathbf{q}}} = \frac{(1+\mathbf{b}) K^{3} D^{1/2} d \tau^{1/2}}{2p_{\mathbf{o}} (1-K^{2}L^{2}) s}, \qquad (9.5)$$

representing proportionality to d.

Physically the reasons for these thickness dependences are as follows. For thick samples, increasing the sample thickness dilutes the photoconductive change. Thin samples, on the other hand, are dominated by surface recombination, so that increasing the thickness allows the photoconductive change to be greater.

9.2.2 Absorption edge

For direct electron transitions between the valence band and the conduction band of a semiconductor, it has been shown that [9.2] the dependence of absorption coefficient on the energy (h_{ν}) of the radiation absorbed has the following forms:

$$K_{a} \propto \frac{\left(h\nu - E_{g}\right)^{1/2}}{h\nu} \tag{9.6}$$

and

$$K_f \propto \frac{(hv - E_g)^{3/2}}{hv}$$
 (9.7)

where K_a and K_f are respectively the absorption coefficients for allowed and forbidden vertical transitions.

If the transition is indirect involving a phonon of energy $k\theta$, the absorption coefficient is given by [9.2]:

$$K = \frac{A}{h\nu} \left[\frac{(h\nu - E_g - k\theta)^2}{1 - \exp(-\frac{\theta}{T})} - \frac{(h\nu - E_g + k\theta)^2}{1 - \exp(\frac{\theta}{T})} \right]$$
(9.8)

where A is a quantity independent of frequency. Thus if an equation of this type applies, a plot of $(Kh\nu)^{1/2}$ against $h\nu$ can yield two linear regions where either the first term in the brackets dominates over the second or vice versa. When many different phonons are involved in a transition, there could be many linear sections and associated break-points in the curve.

9.3 Calculated Absorption Coefficients

9.3.1 Undoped tellurium

Using a computer program, values of absorption coefficient were calculated from equation (9.1) with the measured values of $\Delta\sigma/(\sigma_{Q}E_{q})$ for sample CZ-78-11-11 with the following parameters:

b=2.0[9.3], $p_{o}=1.54 \times 10^{14} \text{ cm}^{-3},$ $d=0.116 \text{ cm}, \qquad s=8000 \text{ cm/sec},$ $D=(kT/q) \mu=53.1 \text{ cm}^{2}/\text{sec}, \qquad \tau=\tau_{f}=4 \text{ µsec},$ $\alpha=s(\tau/D)^{1/2}=2.2,$ $\mu=\mu_{n}=(R_{H}\sigma_{o})_{77} \text{ b=8000 cm}^{2}/\text{V sec},$ R=Reflectivity=0.51 for (E/c) or 0.37 for (E1c) [7.2].

The s-value was estimated by calculation from the ratio of the photoconductivity at the peak to the value at 1.5 μm using a d/L ratio of 7.96; it can be shown that the ratio of the maximum to the plateau value from equation (9.3) depends only on α, when d/L is given. The values of K obtained by calculation are plotted against wavelength in Fig. 9.1 for ELC and E/C, together with the calculated values for the annealed sample CZ-78-11-AN and the abrasively polished sample CZ-78-11-AB using the parameters given in the caption. For comparison the directly measured absorption coefficient values obtained by Tutihasi et al [7.2] at 196 K are also included. The steeper slope of the absorption edge for ELC compared with E/C is clearly apparent. In addition, there is an apparent absorption peak near 3 μm for ELC in the calculated values.

This peak, which corresponds to an energy of about 0.4 eV, could be due to some artifact arising from the experimental method or to absorption from imperfections or to a fundamental electronic transition in tellurium. In the last case, the peak show up in the directly measured absorption coefficient but apparently measurements over this wavelength range for Elc were not covered at 77 K or below by Tutihasi et al [7.2] or by Blakemore and Nomura [9.4]. The peak height the annealed sample is much less than that for unannealed sample, suggesting that the origin imperfections but this is not confirmed for the abrasively prepared sample where the peak is even less pronounced.

The calculated absorption coefficients near the absorption edge are plotted semilogarithmically against photon energy hv in Fig. 9.2 assuming two different values of s. It is noted that in this range the results are not very sensitive to the s-values used in the low photon energy region. In the higher energy region, however, the calculated K results are sensitive to the s-values. Therefore, the absolute magnitude of the calculated K in the high energy region should be viewed with caution. In Figs. 9.3 and 9.4, (Khv) 1/2 is plotted against hv for EIC and E//c respectively. The points do not show clearly defined linear regions; extrapolations to the abscissa give intercepts between 0.31 and 0.33 eV.

The fact that K_{\perp} is larger than K_{\parallel} at the same wavelength near the absorption edge is in keeping with the idea that the ELC transitions are direct allowed while those for $E_{\parallel}C$ are direct forbidden. The ratio K_{\perp}/K_{\parallel} is thus plotted against $h \vee in$ Fig. 9.5. While it is clear that the variation is not exactly linear, it is nearer to a $h \vee E_{g}$ dependence than to its reciprocal. Such a dependence is inconsistent with equations (9.6) and (9.7) which indicate that $K_{f}/K_{a}=h \vee -E_{g}$, as pointed out by Sutter [2.15]. This would imply that K_{\perp} is forbidden and K_{\parallel} is allowed. This apparent paradox has not been explained.

9.3.2 Se Te 1-x alloys

In the case of the Se $_{\rm X}$ Te $_{\rm l-x}$ samples, there is much less certainty about the values of the parameters needed for the calculation of absorption coefficients than for pure tellurium. However, since the absorption coefficient is more directly related to the energy gap and band structure than photoconductivity, calculations of K were made with assumed parameters. The values of these were:

b=2

D=(kT/q) μ , p=1/(R_qq)₇₇, R=Reflectivity taken as linear variation between Te(R=0.51) and Se(R=0.45),

 $\mu=\mu_n=(R_H\sigma_0)_{77}^b$ from present Hall Measurements up to x=0.4, and from work of Beyer et al [2.17] from x=0.4 to 1, $\tau=\tau_f$ measured at each composition.

The calculated K-values for the Te-rich alloys with E $oldsymbol{ exttt{LC}}$ are shown in Fig. 9.6 plotted against wavelength. Here it is while the absorption edge shifts to noted that wavelengths with increasing selenium content, the 3 µm peak has hardly absorption values over the whole moved.The are plotted semilogarithmically against composition range 9.7 and 9.8, where the shift of photon energy in Figs. absorption edge with composition is clearly evident. While these results are nominally for E/c, the points for Elc are not significantly different, except for the Te-rich alloys. As with the case of pure tellurium, it is of interest to see the same data in a plot of $(Khv)^{1/2}$ against hy on linear scales, which are shown in Figs. 9.9 and 9.10. Despite the errors in so doing, a measure of the energy gap of each alloy was determined by extrapolation to the abscissa and reading off the intercept. Such values have been plotted against composition in Fig. 9.11. Points are also given in the same Sutter [2.15] at room figure from the measurements of temperature, representing the energy positions of kinks in the curves of directly measured absorption coefficient. seen that the present results lie above those of

between about 60 and 90 at. Se. It would also appear that a change in energy gap variation occurs near 40 at. selenium as reported by Beyer, Mell and Stuke [2.17]. Fig. 9.12 shows a plot against composition of the energies at which the photoconductivity is half that of the maximum value on the long wavelength side. The points are from the present results at 77 K and the broken curve is from the photoconductivity measurements of Kessler and Sutter [2.33] at room temperature. Again, the present values are higher in the composition region between about 60 and 90 at. selenium.

9.4 Discussion

While determination of absorption coefficients by calculation from photoconductivity is easier than from direct measurements of transmittance in samples, it appears to be less accurate. Part of this is due to lack of knowledge of the parameters involved and part to the incompleteness of the theory. Never-the-less, it is a fairly rapid method and can be used even when K is very high.

In the case of pure tellurium, the deduced absorption coefficients are generally consistent with previously reported values. However, a possible absorption band is involved near 3 µm for Elc, whose origin is not clear. It is unlikely to be an artifact because it is only present for Elc. While no

previously reported directly measured absorption coefficient data appears to exist at this wavelength for ELC, there are data at 77 K for ELC from the work of Tutihasi et al [7.2]. In their plot of $(Kh\nu)^{1/2}$ against $h\nu$ (see Fig. 9.4) there is a kink between two linear regions at an energy of 0.41 eV, corresponding to a wavelength of 3 μ m. Further work is obviously needed on this matter.

For the Se Te alloys there is a greater uncertainty of the parameters used over the whole the values composition range to calculate K. Furthermore, as previously mentioned, there are many improvements to be made in the sample preparation techniques. Despite this, the calculated absorption coefficients clearly show the trend of the band gap variation with composition. The fact that there appears to be a slightly steeper change of band gap with increasing selenium content, starting at about 40 at. & selenium, is in agreement with the suggestion of Beyer, Mell and Stuke [2.17] that the transition from the direct gap of tellurium to the indirect gap of selenium occurs at this composition. Apart from supporting this interesting possibility, the present band gap data will be useful from a practical point of view in the preparation of a semiconductor with a specifically energy band gap for a particular application or experiment.

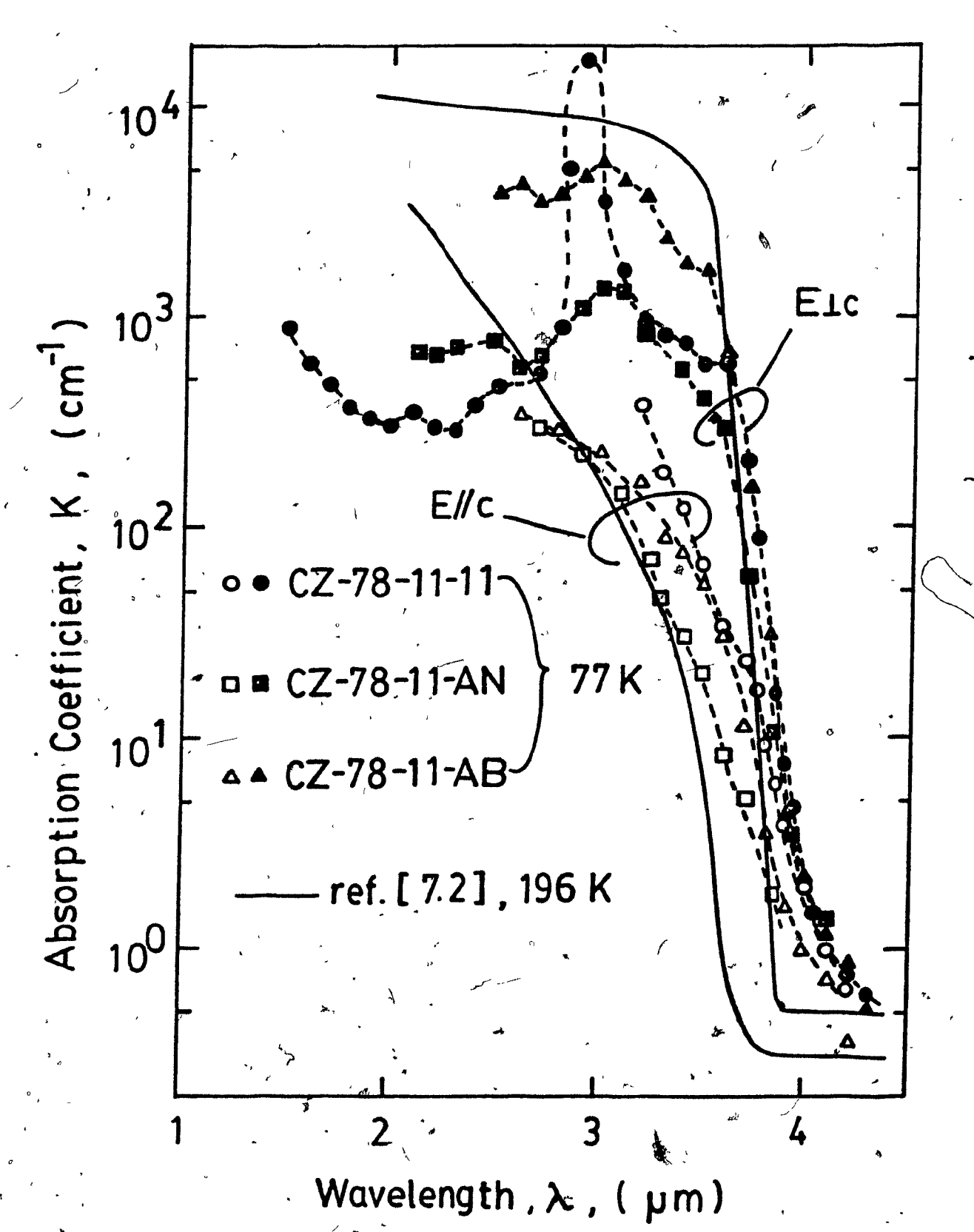


Fig. 9.1 Absorption coefficient at 77 K plotted against wavelength for three tellurium samples with different treatments. The parameters used for the calculation are as follows; ll-ll: \(\mu=4000\) cm²/V sec, \(\tau=4\) \(\mu=6000\) cm/sec, \(\mu=1000\) cm²/V sec, \(\tau=5\) \(\mu=6000\) cm/sec and \(\mu=1000\) cm²/V sec, \(\tau=4\) \(\mu=1000\) cm²/V sec, \(\tau=4\) \(\mu=1000\) cm/sec.

•

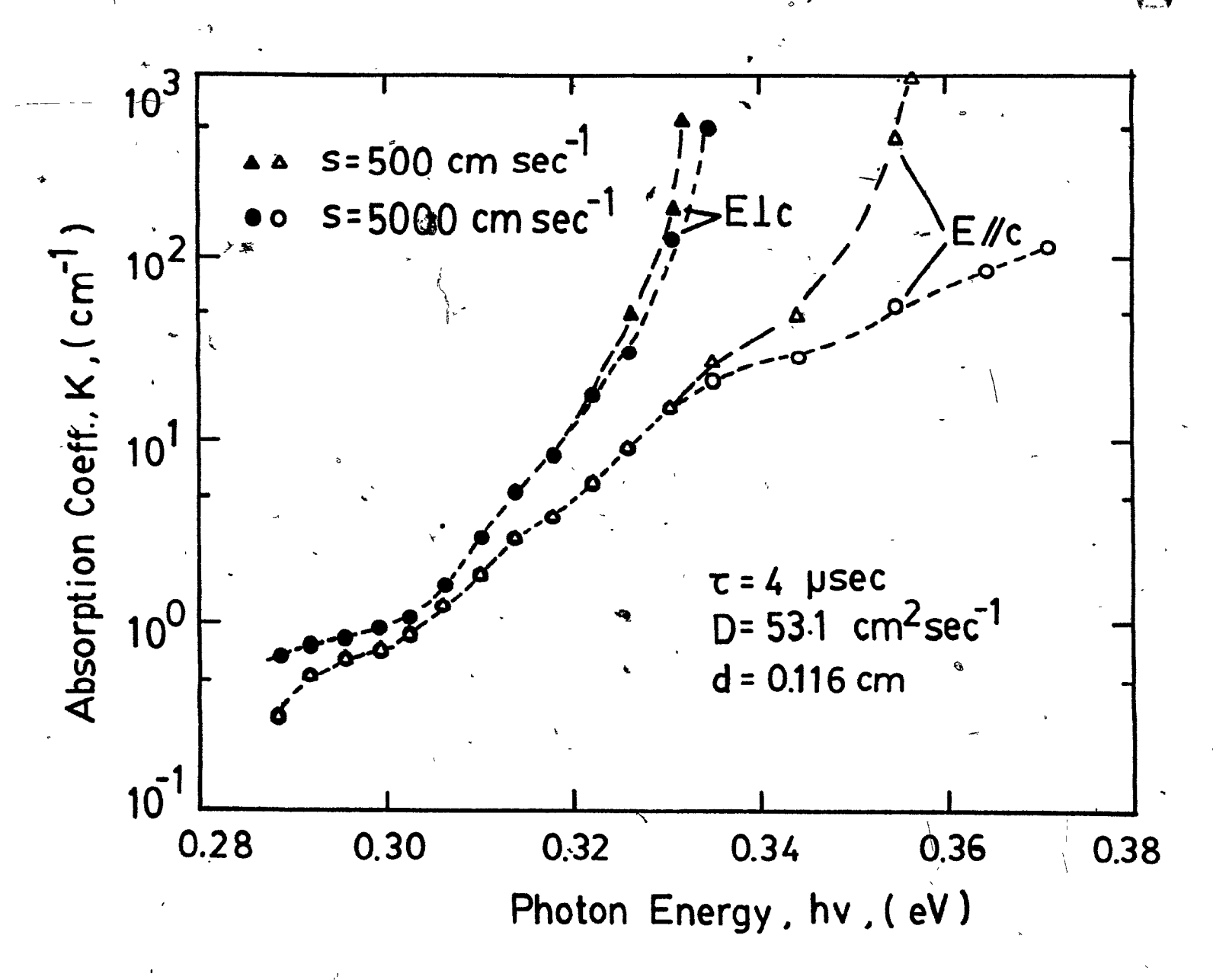


Fig. 9.2 Calculated absorption coefficient at 77 K vs photon energy, hv, for sample CZ-78-11-11 using two s-values for both E#c and EIc.

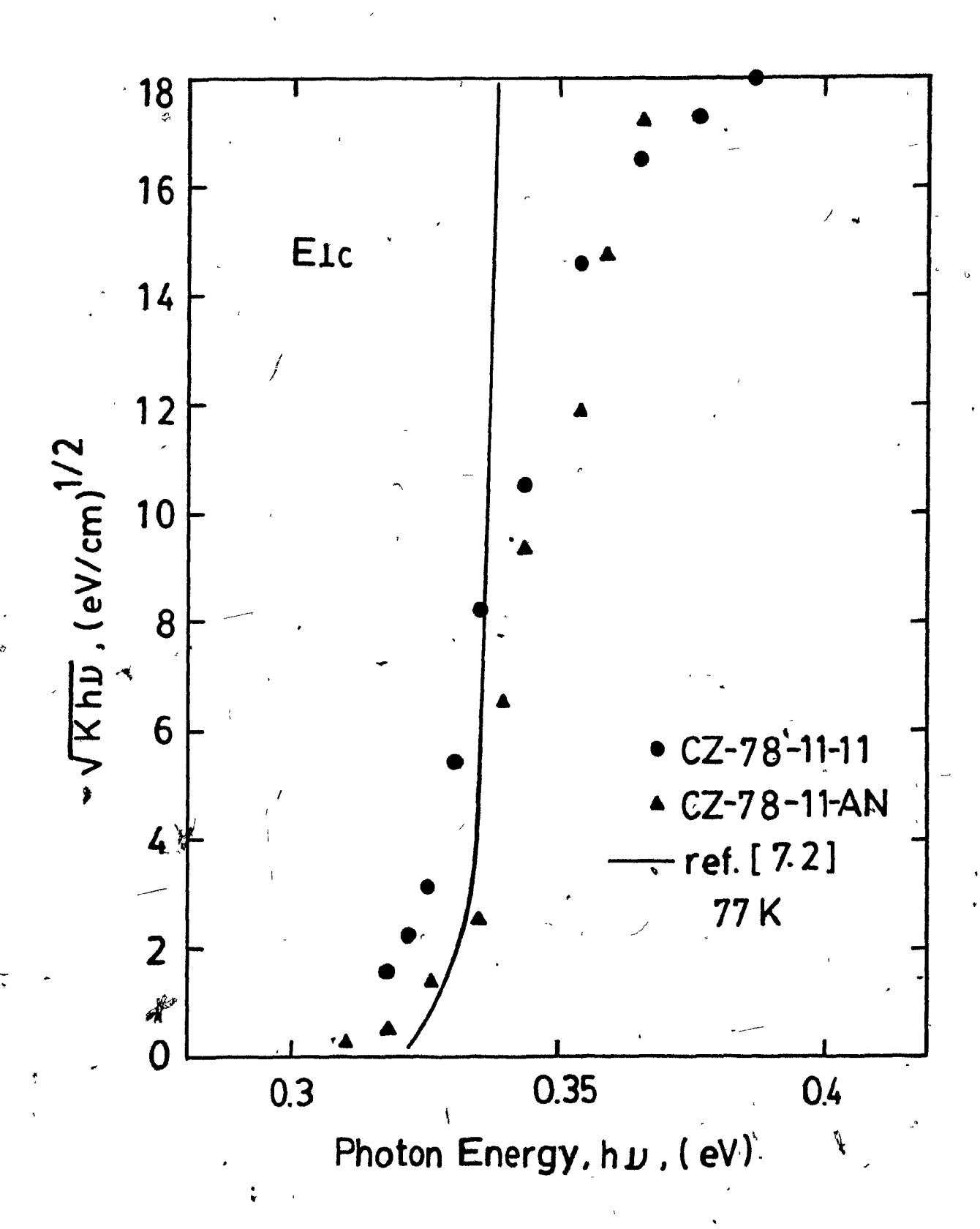


Fig. 9.3 Plot of $(Khv)^{1/2}$ vs hv for tellurium samples with Elc.

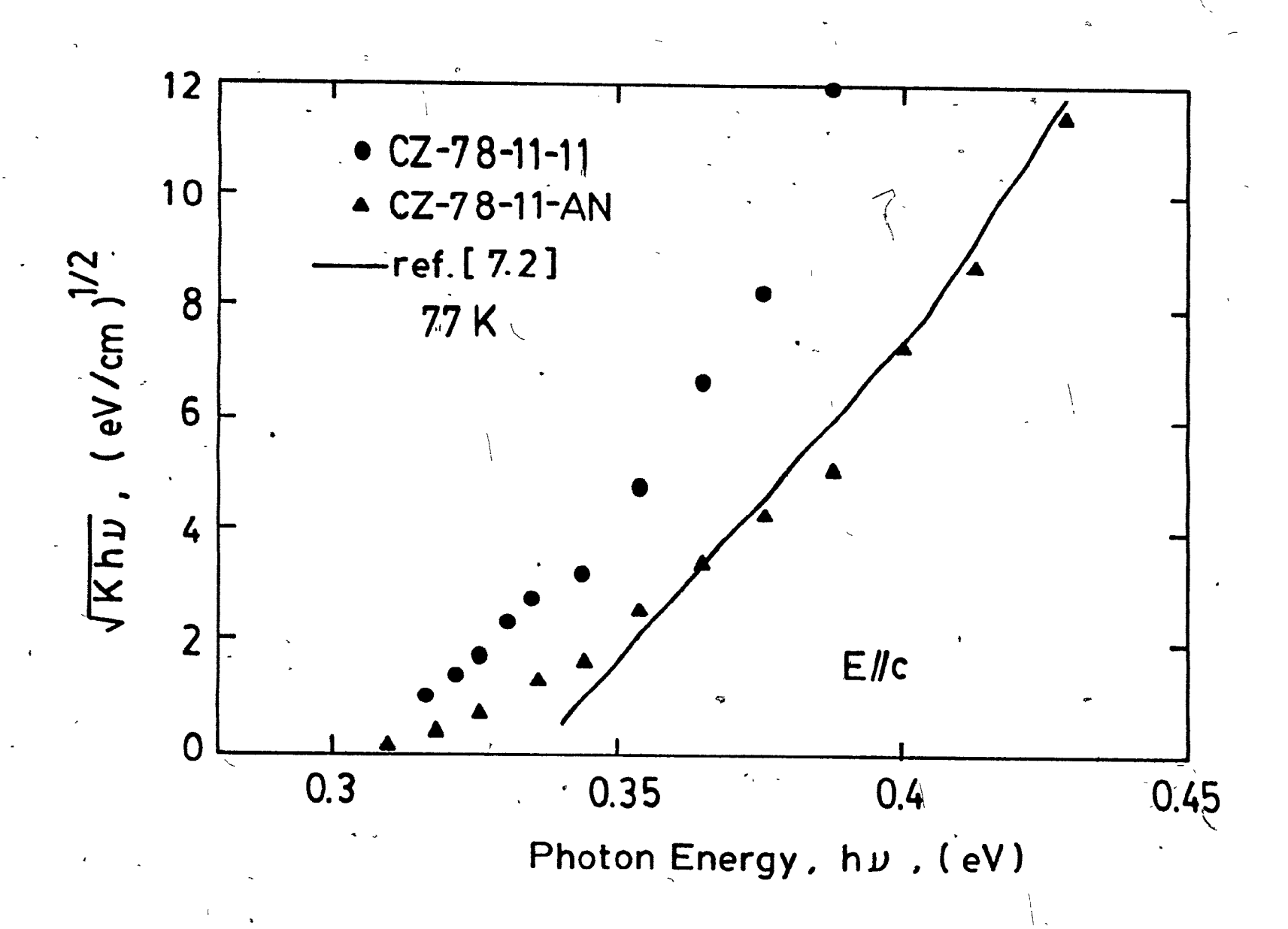


Fig. 9.4 Plot of $(Kh^{\vee})^{1/2}$ vs h^{\vee} for tellurium samples with Elc.

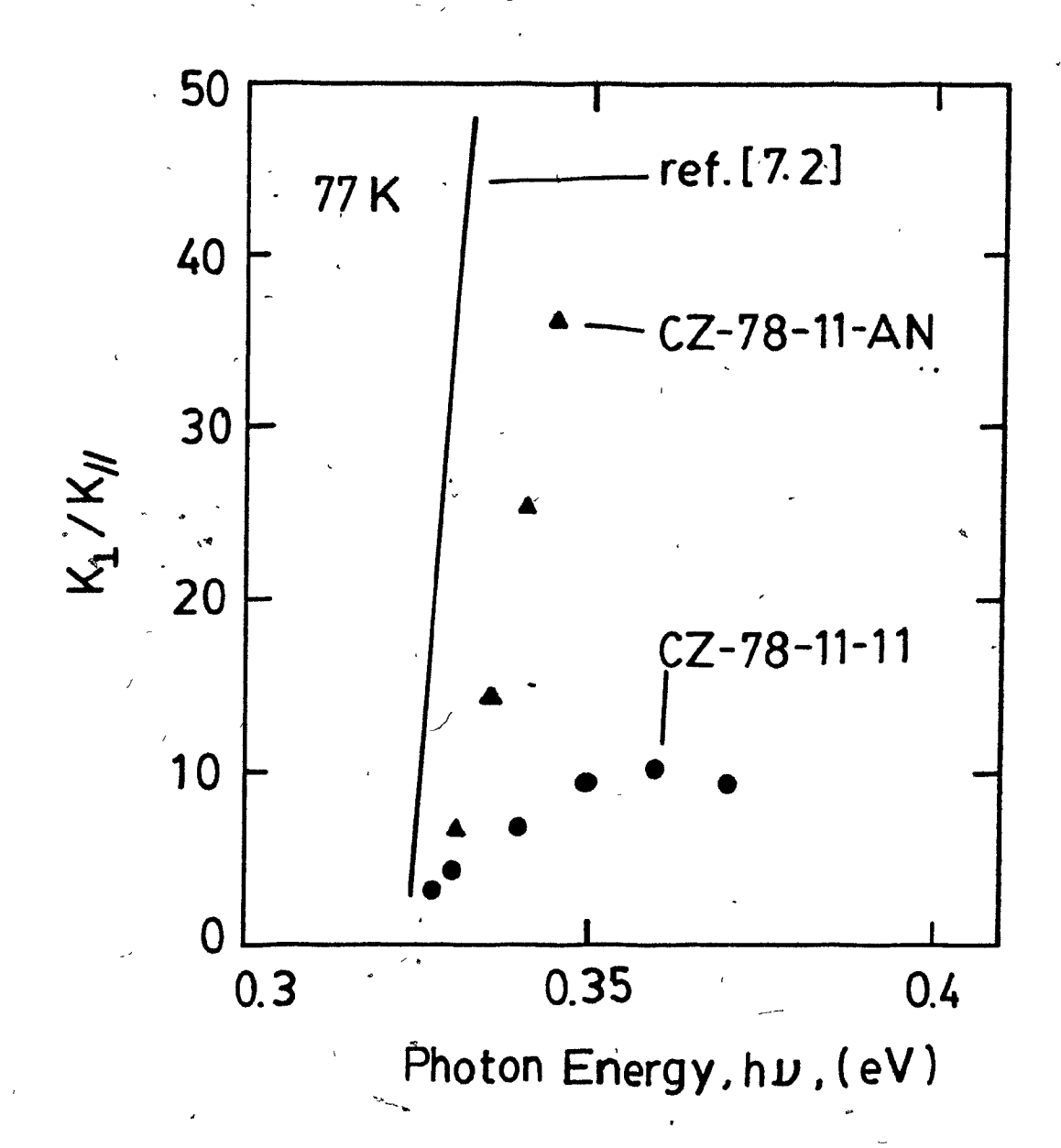


Fig. 9.5 Ratio of K_{\perp} to K_{\parallel} vs hv for tellurium samples at 77K.

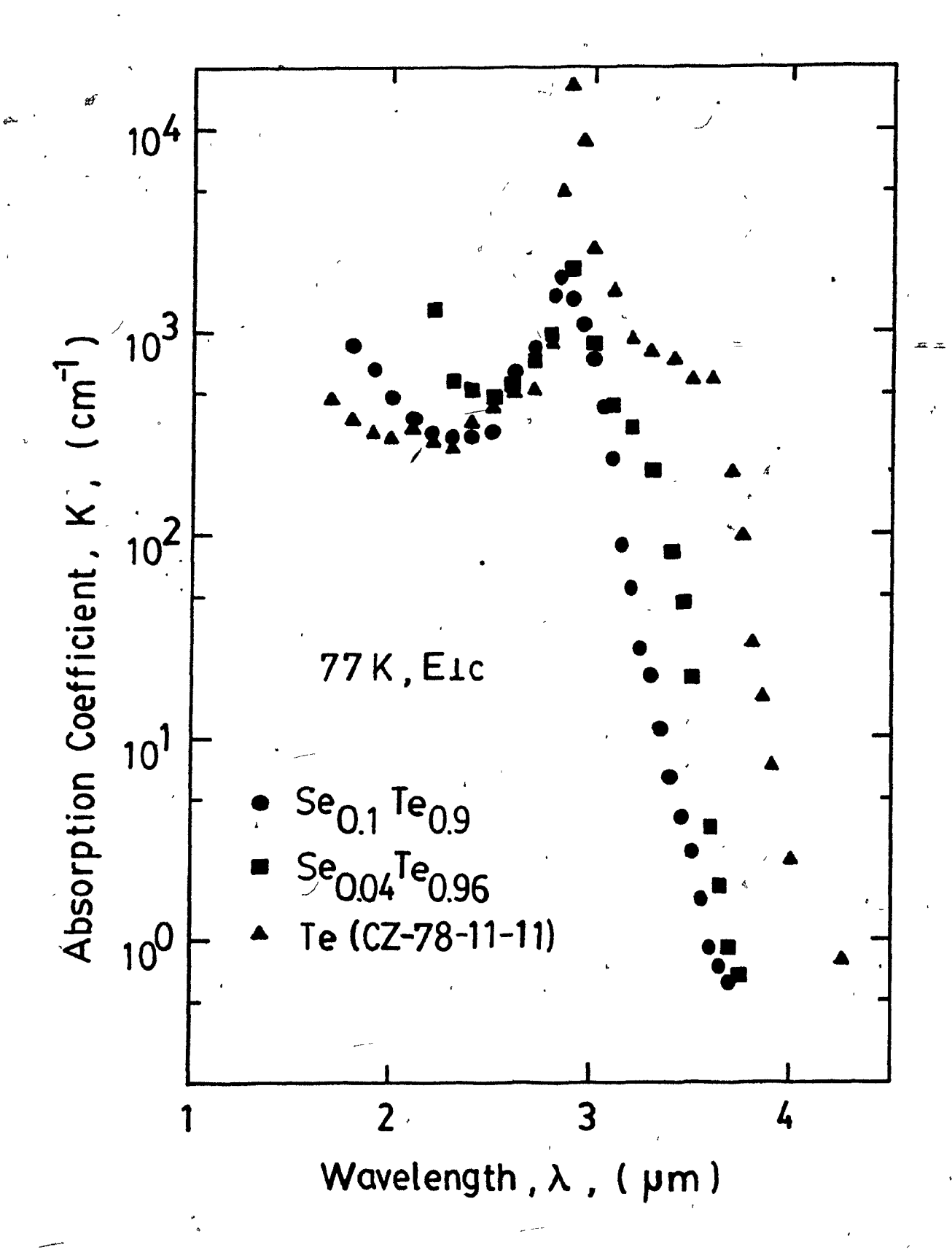


Fig. 9.6 Absorption coefficient at 77 K vs wavelength for the Czochralski-grown Te-rich Se_xTe_{1-x} alloys.

(

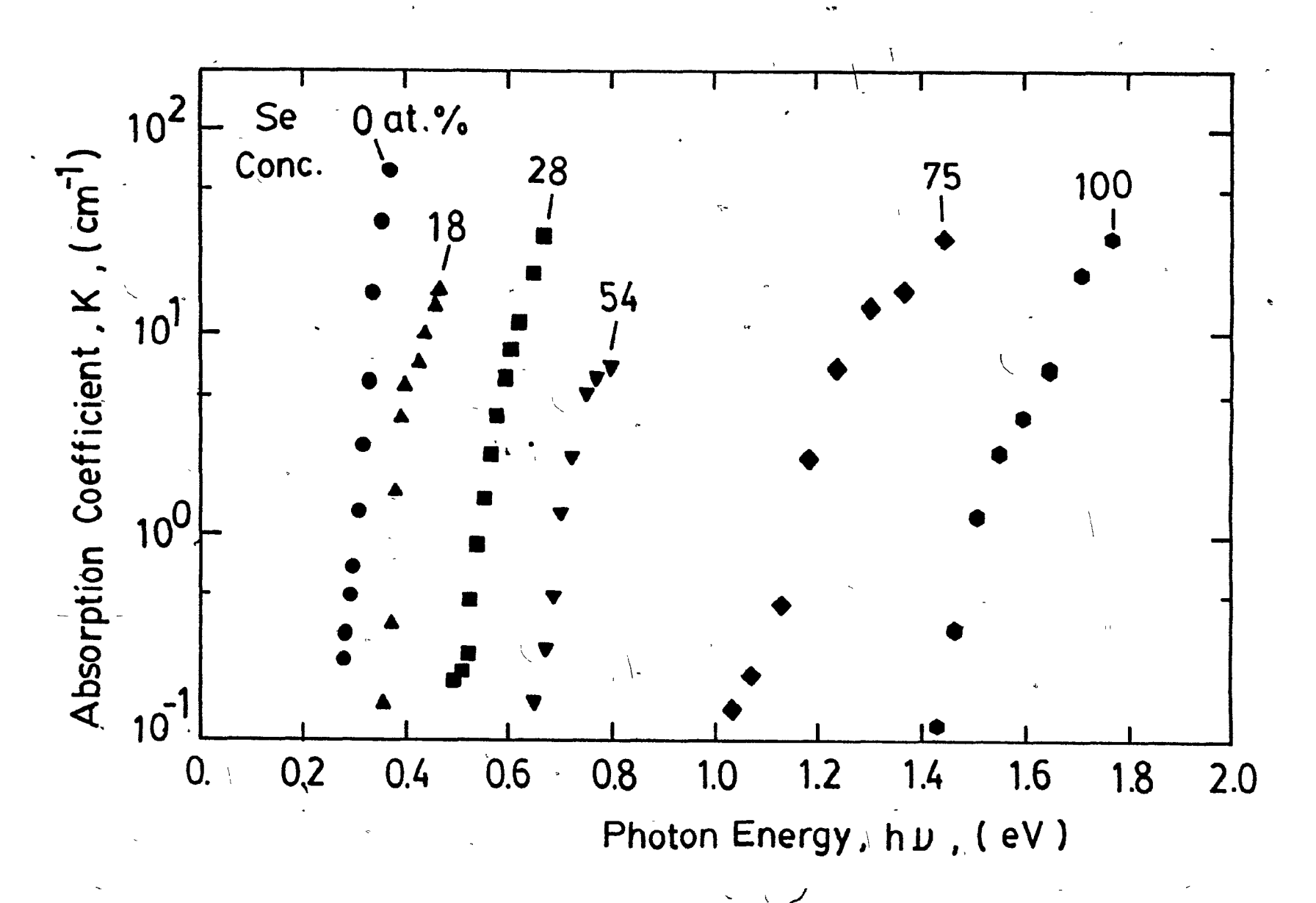


Fig. 9.7 Absorption coefficient at 77 K plotted against hv for the Se Te alloys with E/c.

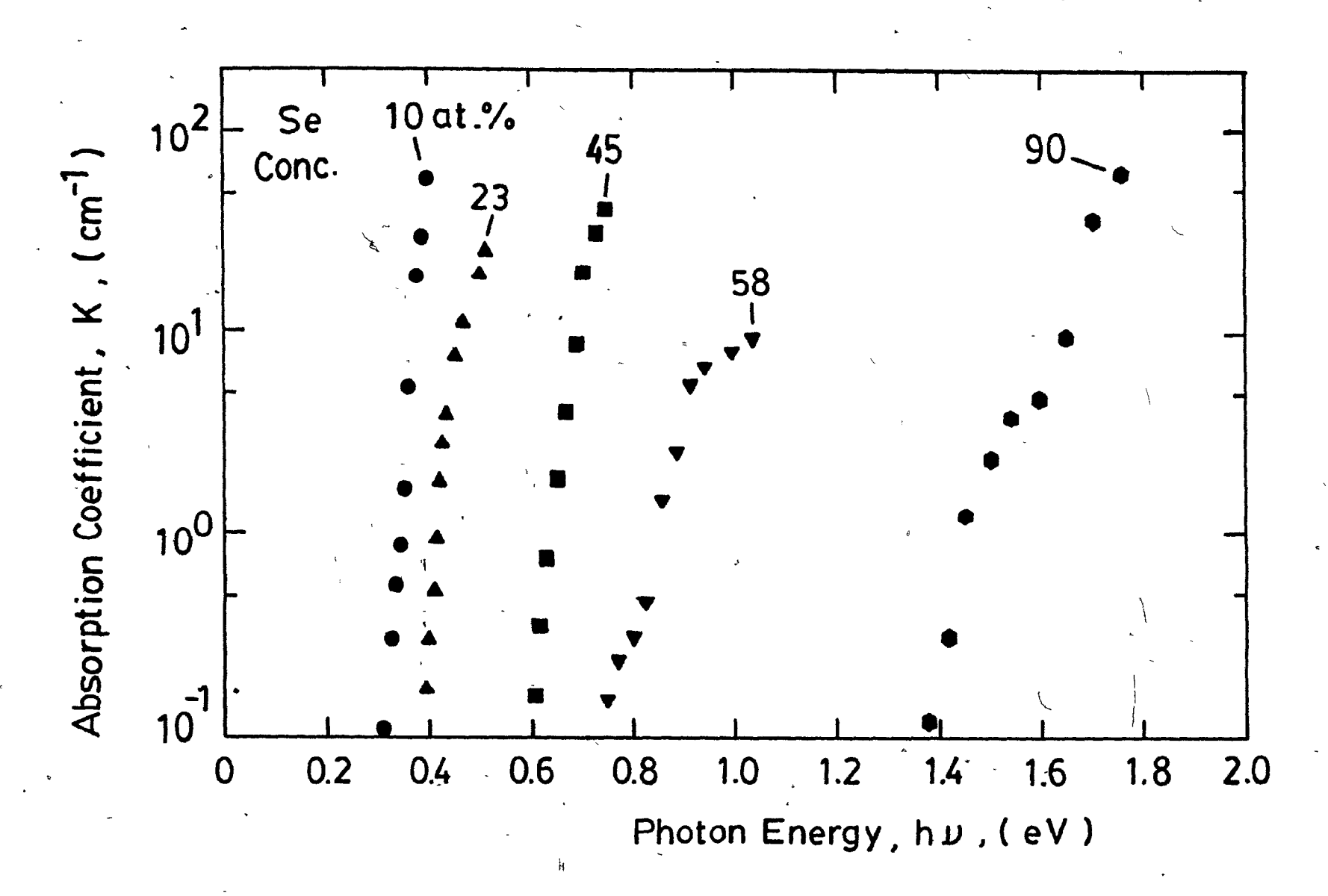


Fig. 9.8 Absorption coefficient at 77 K plotted against hv for the $Se_{x}^{Te}e_{1-x}$ alloys with E// c.

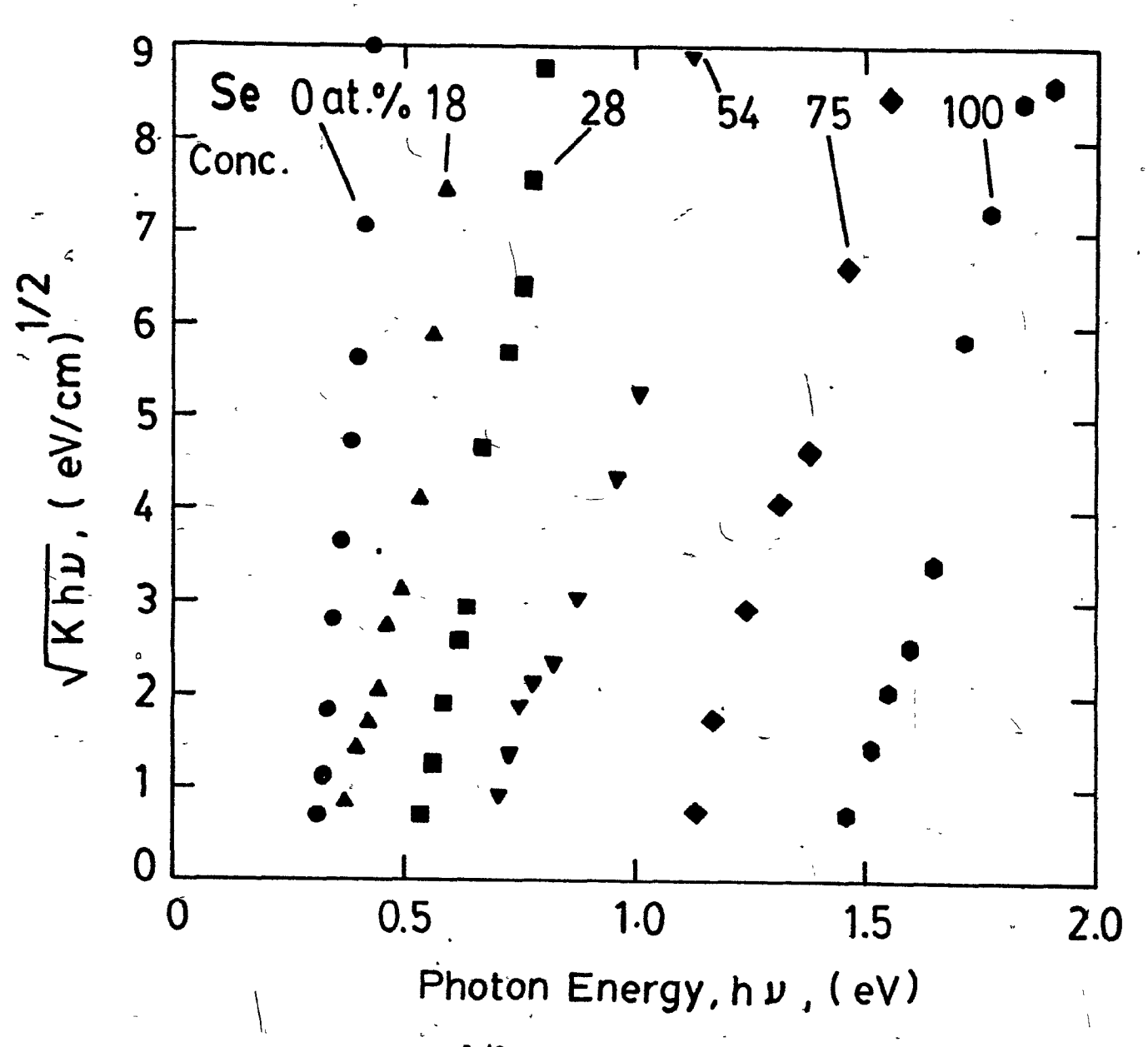


Fig. 9.9 Plot of $(Khv)^{1/2}$ at 77 K vs hv for the $Se_{x}Te_{1-x}$ alloys.

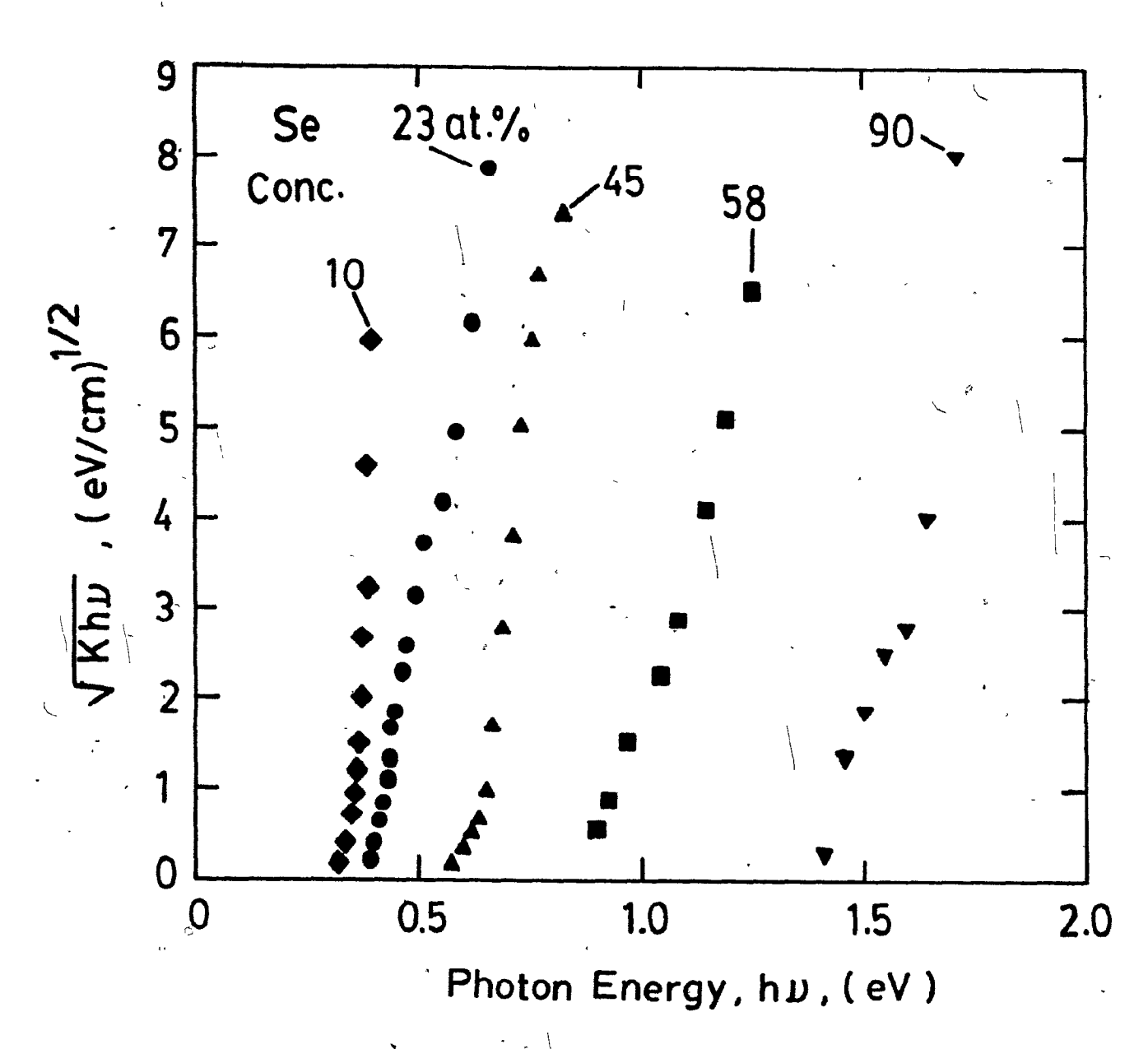


Fig. 9.10 Plot of $(Khv)^{1/2}$ at 77 K vs hv for the Se_XTe_{1-X} alloys.

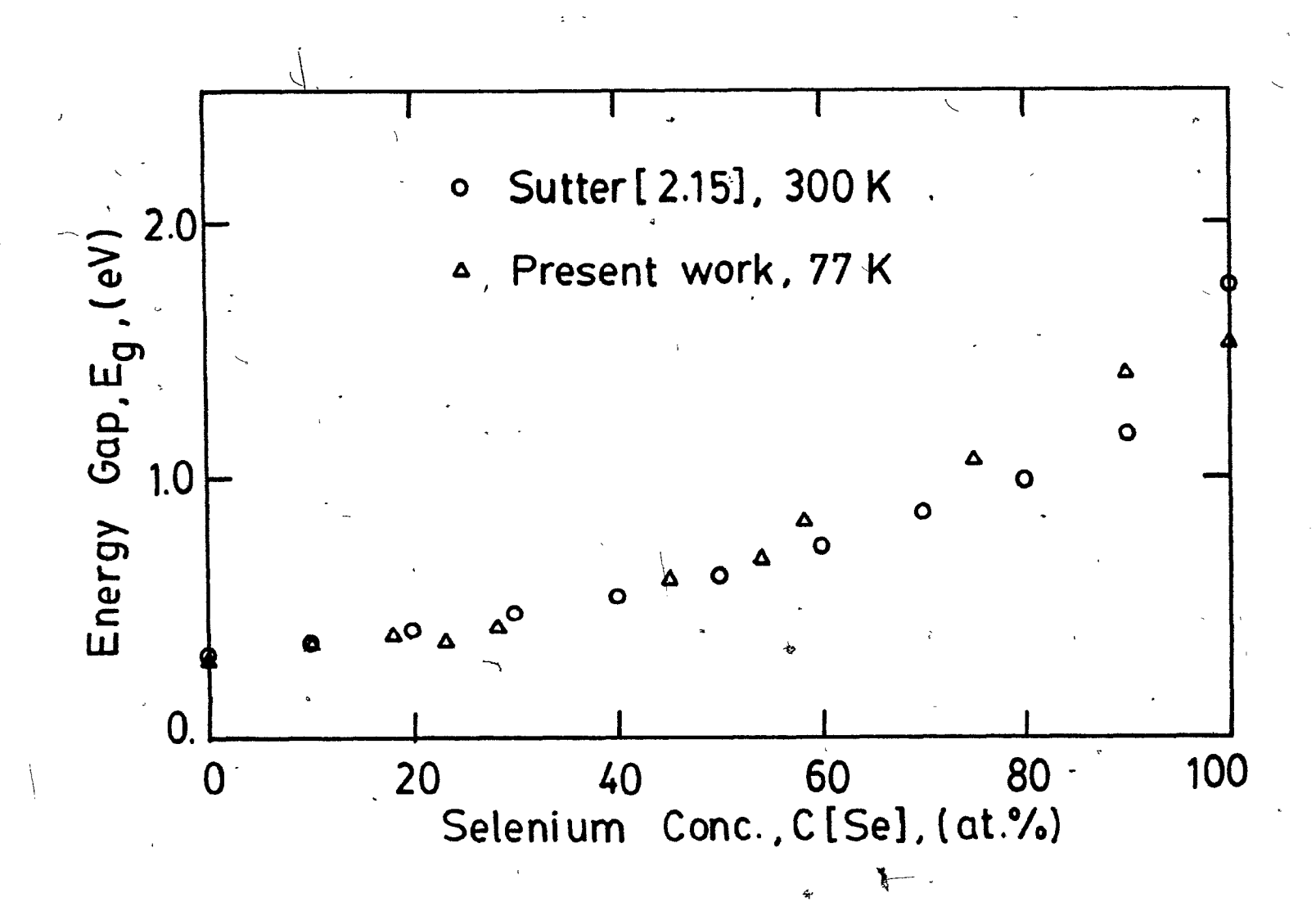


Fig. 9.11 Energy gap obtained from absorption coefficient curves shown in Figs. 9.9 and 9.10 for the $Se_{x}Te_{1-x}$ alloys plotted against the selenium content.

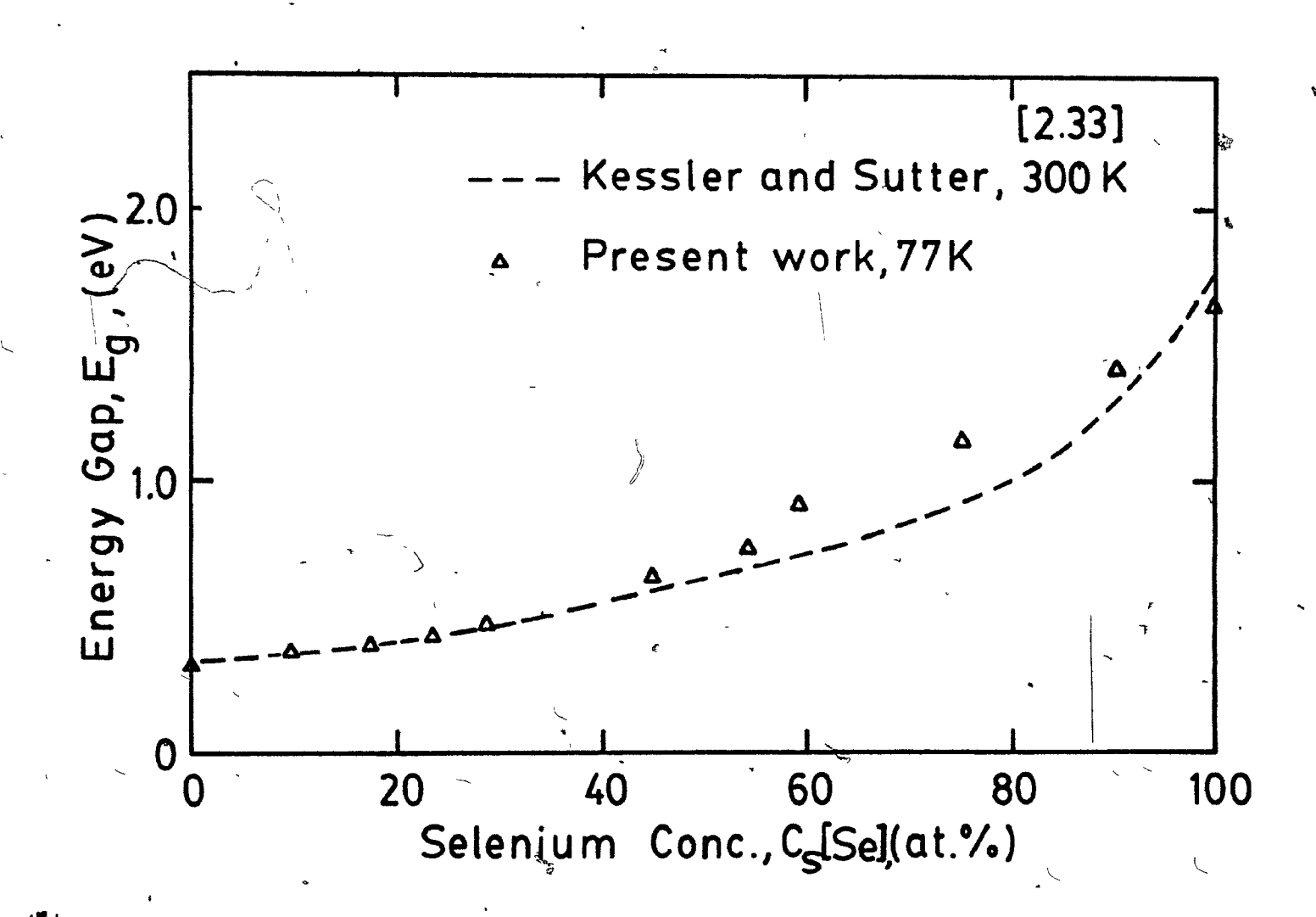


Fig. 9.12 Energy gap obtained from photoconductivity curves (energy of half the maximum on the long wavelength side) plotted against the selenium content.

CHAPTER 10 DISCUSSION AND CONCLUSIONS

10.1 Introduction

In this final chapter the main conclusions and ideas of the thesis are collected together and discussed. This is done firstly for the growth work and then for the photoconductivity studies. Some ideas for future work are also given.

10.2 Growth of Pure Tellurium

As a result of the present work, the technique of growing tellurium monocrystals by the Czochralski method has now reached an advanced stage of development. Having a high background temperature (such as 400°C), as well as a slow approach of the seed to the melt prior to dipping, not only ensures a high yield of monocrystals but also a minimum of defects arising from temperature gradients in the ingots. Such gradients during growth were confirmed to have their largest value, of around a 100°C/cm, near the growing interface, with an approximately exponential temperature variation along the ingot axis. The results in chapter 4 show however, that even under the optimum growth conditions, imperfections are still created in the crystals. None-the-less, these can be greatly reduced by subsequent annealing. Detailed studies to reveal

the nature of these defects were not a part of this thesis but the changes in extrinsic transport properties suggest that they are carrier traps rather than carrier scattering centres.

The work in chapter 3 shows that it is possible to determine the direction in which a crystal was grown by the orientation of the etch pits with respect to the external surfaces. This applies not only to 4-sided pits on the prism faces but to three (or six) sided pits on the basal planes as well. The effect can be explained if growth and etching (which is a form of "anti-growth") take place preferentially on three special pyramidal crystallographic planes, with slower growth on the other three pyramidal planes. The slower growing planes arise from a larger surface density of atoms and in growth it is these that form the facets which create the three larger prism planes of the ingot. It is suspected that a similar process applies to quartz.

10.3 Growth of SexTel-x Alloys

Using the Czochralski method with growth rates down to 0.3 mm/hr, monocrystals of Se_xTe_{1-x} were obtained for 0<x<0.1 and 0.95<x<1.0, that is for compositions with 0 to 10 at.% Se in Te and 0 to 5 at.% Te in Se. Some of these alloys are the first Czochralski-grown monocrystals reported in the literature.

alloys of intermediate composition. possible to obtain ingets by the Czochralski method because of the presence of selenium, in excess of that of the rest of the melt, near the growing interface. This excess selenium, with a density lower than that of the rest of the melt, diffuses away so slowly that its accumulation eventually causes the meniscus to break, thus preventing the formation of an ingot. However, intermediate compositions it was possible to obtain samples, which were crystallographically aligned to the c-axis but not single crystals, by allowing liquid alloy to cool ' slowly over about a week. In such a method, where the growth rate was of the order of 0.1 mm/hr, the solidified material lies underneath the liquid, so that the meniscus problem does not arise. This suggests, that for the intermediate alloys, the Bridgman method or a method involving liquid phase epitaxy on a tellurium substrate would be more suitable processes than the Czochralski method.

10.4 Photoconductivity in Tellurium

The difference in the shape of the photoconductive maximum near 3.5 µm between the orientation ELC and E //c was confirmed to be much the same as that previously reported for pure tellurium at 77 K. However, in the present work, it was found that the magnitude of the photoconductivity, like many other physical properties, was sensitive to sample treatment.

This was most evident near the shortest wavelength used of about 1 µm, where there was a difference of some two orders of magnitude between the responsivity of an annealed sample and one subjected to a light abrasive polish. This increase in photoconductivity with annealing appears to be the result of the combined effects of decreased surface recombination velocity and bulk lifetime and of increased carrier mobility. These changes were shown in annealed samples by increased decay times and an increase of Hall mobility. The existence of interference oscillations of photoconductivity character described by Grosse and Winzer [2.27] and attributed to a damaged layer of tellurium, was not found in the present work despite an intensive effort to observe them.

It was found that the transient photoconductivity could described approximately with two time constants. The physical origin of these is not known but it is suspected that longer value arises from trapping or from surface recombination, while the shorter time constant, magnitude is in microseconds, could be due recombination. Surface recombination velocities in excess of cm/sec_appear to apply to tellurium, even for samples prepared by chemical cutting and polishing and subsequently annealed.

Some of the results in chapter 7 are of interest from a

device point of view, since one of the annealed samples showed the highest D* yet reported on melt-grown tellurium. An even higher value up to the background limit should be possible with further reduction of sample thickness. However, it is likely that a specific program would be needed to develop the technology required to evaluate tellurium for use as an infrared detector material at 3.5 µm, where it would have to compete with existing devices using PbS and InSb.

The calculation of absorption coefficient photoconductivity for tellurium is not as accurate as it could be, because it is not clear how trapping should be taken into account in the theory and because of uncertainties regarding surface recombination processes. The calculated K-values confirm generally the absorption édge obtained transmission measurements except that there is a larger long wavelength tail in the former case, which was first reported by Grosse and Winzer [2.27]. In addition, in the present studies, an absorption peak was observed near 3 µm at 77 K for Elc, which has not been previously reported. However, it will be necessary to observe this peak on many more samples before its existence as a fundamental feature can be definitely confirmed.

10.5 Photoconductivity in Se Te 1-x Alloys

The photoconductivity measurements described in chapter 8 are the first to be measured on the Se Te, alloys below room temperature. They show a continuous shift of the photoconductive maximum from a wavelength of 3.7 µm in the , infrared to about 0.8 µm close to the visible region as the selenium content increases from 0 to 100 at.%. With this composition change, the magnitude of the photoconductivity increases by some 5 orders of magnitude and the decay time constants and the dark resistivity increase by something like the same amount. These changes are qualitatively consistent with the change of energy gap which, from the absorption coefficient analysis, takes place continuously, except for a slope change starting at about 40 at. & Se. This may well be the composition of the transition from a direct to an indirect gap as suggested by Beyer, Mell and Stuke [2.17]. Thus, despite the uncertainties regarding the sample preparation and the limitations of the method of calculating K, the results are able to trace the band gap changes. It should be mentioned, however, that the extrapolations to the abscissa, in the plots of calculated $(Khv)^{1/2}$ versus hy, have given underestimates of the energy gaps of tellurium and selenium those obtained from directly compared with

transmission and reflectance. This may also mean that the energy gaps given for the alloys are also somewhat too small.

10.6 Future Work

Like many investigations, the work in this thesis answers some questions but raises many more. To resolve these further work is needed.

In the area of the fundamentals of photoconductivity in pure tellurium, more studies should be done on transient effects, particularly with background light to fill traps. Surface recombination also should be measured by an alternate method. In addition, an attempt should be made to develop a theoretical model which takes into account lateral sample dimensions and trapping. However, perhaps the most immediate task would be the measurement of photoconductivity on many more annealed and unannealed samples, together with obtaining transmission measurements on the same material to refine the absorption edge and to see if the 3 µm band has definite existence. Accurate reflectance data are also needed in the wavelength range 1 to 4.5 µm at 77 K.

It has already been mentioned that * to evaluate tellurium adequately as an infrared detector material, a a specific device program would need to be undertaken. This

would entail the preparation and mounting of very thin samples having thicknesses in the range 10 to 100 µm. Such samples might be obtained by etching bulk wafers or by vapor growth on a substrate. Extensive measurements of D*, electrical noise and frequency response would be needed.

A wide open field of investigation is available for the SexTe1-x alloys. However, the first task is the preparation of monocrystalline samples under conditions where a minimum of imperfections are introduced. This could be done firstly by growing bulk crystals by a slow Bridgman method or by epitaxial growth from the vapor. Techniques would then need to be developed for the chemical cutting and polishing of the samples with appropriate solvents. After this stage, the samples would be ready for detailed optical and electrical measurements. A simpler, more modest and more immediate program, however, would be to take the material prepared in the present study and carry through annealing treatments, to be followed by a repetition of the photoconductivity and Hall effect measurements to observe the changes.

Finally, it should be mentioned that the availability of bulk selenium crystals, such as have been prepared in this program, opens the way to a number of interesting electrical and optical studies. This is because the material has rarely been available in monocrystalline form in a large enough size

for physical measurements in the laboratory.

REFERENCES

- [1.1] W.M. Becker and V.A. Johnson, in "Tellurium", ed. W.C. Cooper, (Van Nostrand Reinhold Co., N.Y., 1971) 54.
- [1.2] I. Shih, "High Yield Growth of Tellurium Single Crystals by the Czochralski method", McGill University thesis, (1977).
- [1.3] J. Stuke, in "Selenium", ed. R.A. Zingaro and W.C. Cooper, (Van Nostrand Reinhold Co., N.Y., 1974) 174.
- [2.1] J. Weidel, Z. Naturforsch., 9a(1954)697.
- [2.2] T.J. Davies, J. Appl. Phys., 28(1957)1217.
- [2.3] R. Link, Z. Phys. Chem., 221(1962)274.
- [2.4] R.C. Keezer, "Tellurium Crystal Growth", Report No. 2900-435-R, University of Michigan, (1963).
- [2.5] I.I. Farbshtein, A.M. Pogarskii and S.S. Shalyt, Sov. Phys.-Solid State, 7(1966)1925.
- [2.6] T. Ishiguro and T. Tanaka, Jpn. J. Appl. Phys., 6(1967)864.
- [2.7] P. Grosse, "Die Festkorpereigenschaften Von Tellur", (Springer, Berlin, 1969).
- [2.8] E.D. Kolb and R.A. Laudise, "The Physics of Tellurium and Selenium", ed. by W.C. Cooper, (Pergamon Press, 1969), p. 213.
- [2.9] M. Cerclet, Rev. Phys. Appl., 4(1969)63.
- [2.10] R. Dufresne and C.H. Champness, J. Cryst. Growth, 18(1973)34.
- [2.11] M. Cerclet, Document Pec No. 138, Centre National d'Etudes Des Telecommunications, (1973).
- [2.12] I. Shih and C.H. Champness, J. Cryst. Growth, 44(1978)492.
- [2.13] J.J. Loferski, Phys. Rev., 93(1954) 707.
- [2.14] R.C. Keezer, C.H. Griffiths and J.P. Vernon, J. Cryst. Growth, 3,4(1968)755.

- [2.15] E. Sutter, Phys. Status Solidi, 33(1969)749.
- [2.16] T. Shiosaki and A. Kawabata, Jpn. J. Appl. Phys., 10(1971)1329.
- [2.17] W. Beyer, H. Mell and J. Stuke, Phys. Status Solidi (b), 45(1971)153.
- [2.18] S.K. Bahl and J.H. Chen, Mater. Res. Bull., 10(1975)1121.
- [2.19] V.P. Bhatt and S.B. Trivedi, J. Cryst. Growth, 44(1978) 262.
- [2.20] R.C. Keezer, C. Wood and J.W. Moody, "Crystal Growth", ed. H.S. Peiser, (Pergamen Press, Oxford, 1967)119.
- [2.21] E. Grison, J. Chem. Phys., 19(1951)1109.
- [2.22] P.S. Bartlett, Phys. Rev., 26(1925)247.
- [2.23] T.S. Moss, Proc. Phys. Soc. London, A62(1949)264.
- [2.24] D.F. Edwards, C.D. Butter and L.D. McGlauchlin, Solid-State Electron., 3(1961)24.
- [2.25] V.A. Vis, J. Appl. Phys., 35(1964)360.
- [2.26] V.A. Vis, J. Appl. Phys., 35(1964)365.
- [2.27] P. Grosse and K. Winzer, Phys. Status Solidi, 13(1966) 269.
- [2.28] M. El-Azab, C.R. McLaughlin and C.H. Champness, J. Cryst. Growth, 28(1975)1.
- [2.29] W. Smith, Nature, 7(1873)303.
- [2.30] V. Prosser, Proc. Int. Conf. Semiconductor Phys., Prague, (Academic Press, 1960)993.
- [2.31] S.O. Hemila and T.O. Tuomi, Annales Acad. Sci. Fennicae, Series A(1966)199.
- [2.32] J. Stuke, Phys. Status Solidi, 6(1964)441.
- [2.33] F.R. Kessler and E. Sutter, Phys. Status Solidi, 23(1967) K25.
- [3.1] S. Ahmed and S. Weintroub, J. Cryst. Growth, 8(1971)299.

- [3.2] M. El Azab, C.R. McLaughlin and C.H. Champness, J. Cryst. Growth, 28(1975)1.
- [3.3] J.S. Blakemore, J.W. Schultz and K.C. Nomura, J. Appl. Phys., 31(1960)2226.
- [3.4] J.S. Blakemore and K.C. Nomura, J. Appl. Phys., 32(1961)745.
- [3:5] K. Herrmann, Phys. Status Solidi, 1(1961)254.
- [3.6] K.C. Nomura, Phys. Rev. Lett., 5(1960)500.
- [3.7] A. Koma, E. Takimoto and S. Tanaka, Phys. Status Solidi, 40(1970)239.
- [3.8] I. Shih and C.H. Champness, J. Cryst. Growth, 46(1979)458.
- [3.9] J. Di Persio, J.C. Doukhan and G. Saada, Mater. Sci. Eng., 4(1969)123.
- [3.10] J.C. Doukhan and J.L. Farvacque, Phys. Status Solidi(a), 4(1971)Kl.
- [3.11] Zb. Kalinski and G. Lehmann, Kristall und Technik, 11(1976)281.
- [3.12] P. Cherin and P. Unger, Acta. Crystallogr., 23(1967)670.
- [4.1] P. Skadron and V.A. Johnson, J. Appl. Phys., 37(1966)1912.
- [4.2] C.H. Champness and A.L. Kipling, Can. J. Phys., 48(1970)3038.
- [4.3] J.C. Brice, J. Cryst. Growth, 2(1968)395.
- [4.4] H.S. Carslaw and J.C. Jaeger, "Conduction of Heat in Solids", 2nd ed., Clarendon, Oxford, (1959) 214.
- [4.5] D.Q. Kern, "Process of Heat Transfer", McGraw-Hill Book Co., Inc., (1950)77.
- [4.6] E.D. Devyatkova, B.Ya. Moizhes and I.A. Smirnov, Sov. Phys.-Solid State, 1(1959)555.
- [4.7] Y.S. Touloukian and D.P. DeWitt, "Thermophysical Properties of Matter, Vol. 8", IFI/Plenum, New York, (1972)1579.

- [4.8] W.R. Wilcox and L.D. Fullmer, J. Appl. Phys., 36(1965)2201.
- [5.1] W.A. Tiller, K.A. Jackson, J.W. Rutter and B. Chalmers, Acta Met., 1(1953)428.
- [5.2] H.P.D. Lanyon and E.F. Hockings, Phys. Stat. Sol., 17(1966)K185.
- [7.1] N.G. Shyamprasad, C.H. Champness and I. Shih, Infrared Phys., 21(1981)45.
- [7.2] S. Tutihasi, G.G. Roberts, R.C. Keezer and R.E. Drews, Phys. Rev., 177 (1969) 1143.
- [7.3] T. Limperis, in "The Infrared Handbook", ed. W.L. Wolfe and G.J. Zissis, (Office of Navy Research, Washington DC, 1978).
- [8.1] H. Mell and J. Stuke, Phys. Status Solidi(b), 45(1971)163.
- [9.1] N.G. Shyamprasad, "Study of Photoconductivity in Undoped Tellurium", McGill University thesis, (1979).
- [9.2] T.P. McLean, Prog. Semicond., 5(1960)53.
- [9.3] I.L. Drichko, I.V. Mochan and Yu. N. Obraztsov, Sov. Phys. Solid State, 4(1963)1842.
- [9.4] J.B. Blakemore and K.C. Nomura, Phys. Rev., 127(1962)1024.